FEDERAL UNIVERSITY OF SANTA CATARINA
GRADUATE PROGRAM IN CHEMICAL ENGINEERING

Willbrynner Pereira Marques

Mg/Fe-based adsorbents for phosphate removal from synthetic wastewater and sewage

FLORIANÓPOLIS
2024

Willbrynner Pereira Marques

Mg/Fe-based adsorbents for phosphate removal from synthetic wastewater and sewage

PhD thesis presented to the Graduate Program in Chemical Engineering at Federal University of Santa Catarina to obtain the degree of Doctor in Chemical Engineering.

Advisor: Prof. Dr. Adriano da Silva

Co-advisor: Prof. Dr. Edson Passamani Caetano

FLORIANÓPOLIS
2024

Ficha catalográfica gerada por meio de sistema automatizado gerenciado pela BU/UFSC.
Dados inseridos pelo próprio autor.

Pereira Marques, Willbrynner
Mg/Fe-based adsorbents for phosphate removal from synthetic wastewater and sewage / Willbrynner Pereira Marques ; orientador, Adriano da Silva, coorientador, Edson Passamani Caetano, 2024.
91 p.

Tese (doutorado) - Universidade Federal de Santa Catarina, Centro Tecnológico, Programa de Pós-Graduação em Engenharia Química, Florianópolis, 2024.

Inclui referências.

1. Engenharia Química. 2. Composite synthesis. 3. Phosphorous recovery. 4. Adsorption. 5. Sewage. I. da Silva, Adriano. II. Passamani Caetano, Edson. III. Universidade Federal de Santa Catarina. Programa de Pós Graduação em Engenharia Química. IV. Título.

Willbrynner Pereira Marques

Título: Mg/Fe-based adsorbents for phosphate removal from synthetic wastewater and sewage

O presente trabalho em nível de Doutorado foi avaliado e aprovado, em 22 de dezembro de 2023, pela banca examinadora composta pelos seguintes membros:
Prof.(a) José Rafael Cápua Proveti, Dr.
Universidade Federal do Espírito Santo

Prof.(a) Leandro Pellenz, Dr.
Instituto Federal de Brasília

Prof.(a) Selene Maria de Arruda Guelli Ulson de Souza, Dr.(a)
Universidade Federal de Santa Catarina

Certificamos que esta é a versão original e final do trabalho de conclusão que foi julgado adequado para obtenção do título de Doutor em Engenharia Química.

Documento assinado digitalmente
Debora de Oliveira
Data: 13/08/2024 12:37:56-0300
CPF: ***.453.929-**
Verifique as assinaturas em https://v.ufsc.br

Coordenação do Programa de Pós-Graduação

Documento assinado digitalmente
ADRIANO DA SILVA
Data: 13/08/2024 11:15:24-0300
CPF: ***.709.189-**
Verifique as assinaturas em https://v.ufsc.br

Prof. Adriano da Silva, Dr.
Orientador

Florianópolis, 2024.

ACKNOWLEDGEMENTS

Over the last years of my graduate school at Federal University of Santa Catarina, I have learned many things not only about science, but also about life. It is necessary resilience, consistence and creativity to pass through the challenges. I believe that the ending results are rewarding.

First of all, I want to give all my thanks to my parents that encouraged and cheered me.

I also thank my advisor, Prof. Adriano da Silva, and my co-advisor, Prof. Edson Passamani, for all the support and guide throughout the years. They were always opened to evaluate new research ideas, also proposing ways to overcome issues of ongoing studies. I also want to thank my friend, Janiomar Barros, for starting this project and working with me. I would like to thank Prof. Eduardo Perini Muniz and Afonso Henrique da Silva Júnior for all their technical support and kindness.

I thank the Federal University of Santa Catarina for the opportunity to live this experience. Also, I thank FAPES and CNPq for financial support.

ABSTRACT

The eutrophication phenomenon, which is mainly characterized by an excessive algae growth, is causing a significant concern to the global society due to its intensification caused by the release of effluents with a high concentration of phosphate. On the other hand, there is a notable demand of fertilizers based on P-rich species for food production. Thus, considering the gradual increase of fertilizer demands based on P species, wastewater treatment using adsorption method could be a suitable mechanism to correlate these two issues, i.e., the phosphates could be recovered from sewage to be used as a fertilizer. Mg-based adsorbents have proven to be a promising path for treating water rich in P-species, and more importantly, magnetic adsorbents can be used in magnetic remediation process. Thus, magnetic Mg-Fe based composites (stoichiometric Mg-ferrite and Mg-rich matrix) were successfully synthesized via sol-gel method under different experimental conditions. No direct correlation between calcination temperature, specific surface area and adsorption efficiency was observed. The best performance of Sol-Gel synthesized adsorbent occurred for C-MgFeO (Mg-rich material) sample calcinated at 973 K with an adsorption capability of 60 $mg.g^{-1}$ (50 $mg.L^{-1}$ of P and 0.6 $g.L^{-1}$ of adsorbent). Adsorbents calcinated at 973 K maintained their adsorption efficiency through three adsorption cycles. However, since C-MgFeO requires less dosage to remove phosphate, the treatment cost was 8 times lower compared to S-MgFeO. To simplify the $MgO/MgFe_2O_4$ synthesis, the co-precipitation method was also employed (which also reduced the preparation cost), and the composite was also functionalized with vanadium. The incorporation of V into the material improved the adsorption and desorption capacity. The cost to produce 1 kg of V-substituted $MgO/MgFe_2O_4$ via co-precipitation is at least 15 % cheaper than $MgO/MgFe_2O_4$, and the maximum adsorption capacity obtained at isotherm experiments for the former material was 120 $mg.g^{-1}$ (three times higher than the latter adsorbent). The non-doped and V-doped composites were employed at a multicycle adsorption reuse to treat a secondary sewage effluent. Even though V-modified adsorbent costed 15 % higher to synthesize, its better adsorption (23 % higher) and desorption (40 % higher) efficiency made the V-modified composite synthesized via co-precipitation the most promising adsorbent in this project.

Keywords: Sewage. Phosphate. Adsorption. MgO. $MgFe_2O_4$.

RESUMO EXPANDIDO

Introdução

Os aspectos relacionamentos ao lançamento de esgoto não tratado em recursos hídricos vêm sendo bastante discutidas. Do ponto de vista de impactos ambientais, altas concentrações de fósforo nos manaciais decorrente da poluição resulta na eutrofização que consiste em um crescimento descontrolado de algas. Na medida em que as algas são decompostas por bactérios, ocorre a depleção de oxigênio tornando o recurso hídrico impróprio para diversas espécies marinhas. Se por um lado o fósforo em cursos d'águas é indesejável, por outro lado essa espécie é muito importante na agricultura visto que essa é um nutriente que auxília no crescimento. Portanto, a recuperação de P do esgoto pode ser uma oportunidade de se obter um subproduto para a agricultura. A adsorção tem se mostrado um método promissor para remoção do fósforo do efluente devido sua alta eficiência. O adsorvente gasto passa por um processo de desorção a fim de liberar os ions fosfato e de regenerar os sítios ativos. Diversas técnicas de síntese de adsorventes vêm sendo empregadas, sendo que a coprecipitação e sol-gel são as que estão em evidência. Devido a grande relevância do tema, compreender os efeitos dos parâmetros de síntese na eficiência de remoção de P se faz necessário, bem como avaliar a viabilidade econômica no uso de processos adsortivos para remediação ambiental.

Objetivos

O objetivo geral desse trabalho foi sintetizar materiais adsorventes baseados em Mg-Fe para remoção de fósforo em efluentes síntiticos e oriundo de estação de tratamento de esgoto.

A partir disso, os objetivos específicos foram traçados e consistem em: i) avaliar a influência dos métodos e parâmetros de síntese nas características do materiais e sua eficiência de adsorção; ii) realizar experimentos de adsorção com efluente síntetico e real; iii) propor mecanismo de adsorção; iv) estimar o custo referente a síntese dos adsorventes e do tratamento do efluente.

Metodologia

$MgFe_2O_4$ e $MgO/MgFe_2O_4$ foram sintetizados pelo método sol-gel, sendo investigado 3 temperaturas de calcinação (673 K, 823 K, 973 K). Os materiais obtidos foram caracterizados por DRX, área superficial, MEV-EDS, pH de carga zero, histerese magnética e espectroscopia

Mössbauer. Estudos de adsorção com efluente sintético foram realizados para avaliar a influência da dosagem de adsorvente, concentração inicial de P, tempo de contato e pH na eficiência do processo. A fim de simplificar o procedimento de síntese e reduzir o custo, o método de coprecipitação foi implementado para produzir um compósito $MgO/MgFe_2O_4$ modificado e não modificado com vanádio. Os produtos foram extensivamente caracterizado na sua forma bruta e após seu uso no processo de adsorção. As técnicas empregadas foram: DRX, FTIR, espectrocopia Mössbauer, histerese de magnetização, MEV e MET, análise de área superficial, e pH de carga zero. Além dos experimentos de adsorção realizados no trabalho dos materiais sintetizados pelo método sol-gel, dessa vez foi realizado ainda estudo de influência de íons coexistentes no efluente sintético. O reúso em multiciclos de adsorção foi conduzido com efluente sanitário.

Resultados e Discussões

Verificou-se pela caracterização dos materiais adsorventes sintetizados pelo sol-gel que uma grande quantidade de fases espúreas foram formadas ao calcinar a 673 K e 823 K. Entretanto, os adsorventes produzidos a 673 K e 973 K tiveram performance satisfatória para remoção de P. Os resultados indicaram que o adsorvente rico em Mg e calcinado a 973 K obteve melhor pureza, estabilidade química e capacidade de adsorção (60 $mg.g^{-1}$ para 50 $mg.L^{-1}$ de P e 0.6 $g.L^{-1}$ de adsorvente).

A fim de reduzir o tempo dispendido na síntese dos compósitos e reduzir o custo de síntese A cinética indicou que o processo de adsorção ocorre em duas etapas: difusão externa e difusão intra-particula. O modelo de Freundlich foi o que melhor se ajustou aos dados experimentais, com capacidade máxima de adsorção de aproximadamente 120 $mg.g^{-1}$ para ambos os adsorventes. Os testes de reuso dos adsorventes em multiciclos foram realizados com efluente proveniente de uma estação de tratamento de esgoto. Inferiu-se que o mecanismo de remoção de P ocorre: (i) atração eletrostática; (ii) troca de ligante; (iii) lixiviação do Mg. Embora o material modificado com vanádio tenha custado 15 % a mais para sintetizar, sua melhor performance na adsorção (23 % superior) e desorção (40 % superior) tornou este o mais promissor nesse projeto.

Considerações Finais

As observações demonstraram que o método de co-precipitação possui diversas vantagens em face ao sol-gel: (i) a produção por co-precipitação tem menor custo e maior reprodutibilidade

entre as bateladas de síntese; (ii) a preparação da amostra por co-precipitação gera materiais nanocristalinos; (iii) o procedimento de co-precipitação demanda menor tempo para gerar o adsorvente; (iv) os adsorventes apresentaram melhor desempenho quando sintetizados por co-precipitação. Outros parâmetros podem ser investigados a fim de melhorar o custo de produção e a eficiência de remoção de fósforo, como o aumento do teor de Mg no compósito e o uso de outros metais dopants.

Palavras-chave: Esgoto. Fosfato. Adsorção. MgO. $MgFe_2O_4$.

LIST OF FIGURES

LIST OF TABLES

LIST OF ABBREVIATIONS

AF – Antiferromagnetic state
BET – Brunauer–Emmett–Teller
BJH – Barrett-Joyner-Halenda
EBPR – Enhanced biological phosphorus removal
EDS – Energy dispersive spectroscopy
FI – Ferrimagnetic
FTIR – Fourier-transform infrared spectroscopy
ID – Intraparticle diffusion
PFO – Pseudo-first order
pH_{PZC} – Point of zero charge
PSO – Pseudo-second order
PZC – Point of zero charge
SAED – Selected area electron diffraction
SEM – Scanning electron microscopy
SPM – Superparamagnetic
SSA – Specific surface area
TEM – Transmission electron microscopy
XRD – X-ray diffraction

LIST OF SYMBOLS

b : Langmuir’s adsorption constant

B_{hf} : Magnetic hyperfine field

q_e : Adsorption capacity at equilibrium

q_t : Adsorption capacity at time t

q_{max} : Maximum amount of adsorbate adsorbed per unit weight of adsorbent

C_0 : Initial adsorbate concentration

C_e : Adsorbate equilibrium concentration

D : Adsorbent dosage

H_C : Coercivity

K : Effective magnetic anisotropy

k_B : Boltzmann constant

k_1 : Pseudo-first order adsorption rate constant

k_2 : Pseudo-second order adsorption rate constant

k_{s1} : Diffusion rate parameter

k_f : Freundlich isotherm parameter

M_R : Remanence

M_S : Saturation magnetization

Q_{UA} : Quadrupolar shifting

$1/n$: Freundlich isotherm parameter

χ_m : Magnetic susceptibility

δ : Isomer shift

CONTENTS

1 INTRODUCTION

The new regulatory framework for the application of public policies on basic sanitation sanctioned by Brazilian government in 2020 stipulates that 99 % of the population must have potable water and 90 % must have sewage collection and treatment until 2033 (BRASIL, 2020). Therefore, it is estimated that R$ 893.3 billion might be invested for the expansion and maintenance of water supply and sewage structures (ABCON, 2022).

A report released in 2021 by the Brazilian National Sanitation Secretariat indicates that only 50.8 % of generated sewage were treated (MDR, 2021). The remaining untreated sewage released to the environment, which contains phosphorus, stimulates uncontrolled algae blooms (eutrophication). During organic matter decomposition, oxygen is consumed by aerobic bacteria, which impacts the maintenance of aquatic life.

Phosphate removal makes sewage treatment more expensive. However, the recovered phosphorus can be used as fertilizer, a valuable by-product that reduces dependence of fertilizers from other countries and may minimize the production cost of food (CHRISPIM; SCHOLZ; NOLASCO, 2019; MAYER et al., 2016).

In this regard, according to International Fertilizer Association, the demand for NPK (nitrogen, phosphorus and potassium) fertilizers in 2018 was of 190 million tons, and this market was valued at US$ 155.8 billion in 2019 (ILINOVA; DMITRIEVA; KRASLAWSKI, 2021). Phosphorous (P) is mainly obtained by mining phosphate rocks deposits, a non-renewable resource, and its production is threatened by the exhaustion of mineral reserves (CORDELL; DRANGERT; WHITE, 2009). However, a common concentration of phosphate in sewage varies from 4 mg.L^{-1} to 15 mg.L^{-1} (SPERLING, 2007), thus P could continuously be recovered from sewage treatment plants reducing the mining impacts on the environment.

Among conventional methods for phosphorus removal, chemical precipitation and biological processes have been employed. The former is efficient, but a high concentration of aluminum is toxic for the majority of plants and iron strongly binds to phosphate, turning less bioavailable (CHRISPIM; SCHOLZ; NOLASCO, 2019; OWODUNNI et al., 2023). The latter can be inhibited by a myriad of factors as organic matter, toxic species, and operation parameters, which makes the process very complex (WU, Baile et al., 2020; ZHENG et al., 2014). Based on these issues, new adsorbents must be studied to be tested in water remediation with a possibility of its final removal from the effluent after the treatment, reducing the concentration of the adsorbent in the final effluent.

In this context, magnetic adsorbents have successfully been tested, e.g., for Pb removal in real effluents (RAMOS-GUIVAR et al., 2023) imposing that the magnetic remediation method is a promising technique for other contaminants, e.g., P removal. Indeed, it has been recently demonstrated that spinel M-ferrites (MFe_2O_4, M = Zn, Mn, Ni, Co) are promising magnetic adsorbents for P removal from synthetic effluents (REDDY; YUN, 2016). In particular, the Mn-ferrite (synthetized through the coprecipitation method) removed over 95 % phosphates from 10 mg.L^{-1} $H_2PO_4^-$ solution after 1 h of contact time (XIA et al., 2016), while the Zn-ferrite has adsorbed 70 % of phosphates at pH 3, adsorbent dosage of 1 g.L^{-1} and a phosphate initial concentration of 5 mg.L^{-1} (GU et al., 2016).

There are reports in the literature that X-substituted M-ferrites can enhance P removal properties. In particular, GU and coworkers (2017) have shown that Zn-ferrite had a maximum P adsorption of 5.2 mg.g^{-1}, while Ce-substituted $ZnFe_2O_4$ obtained a q_{max} of 41.6 mg.g^{-1}. Also, GU and coworkers (2018) observed that amino-functionalized Cu-ferrite had a maximum adsorption capacity of 9.92 mg.g^{-1}, but when the adsorbent was loaded with La, its q_{max} increased to 32.59 mg.g^{-1}.

In addition, several works have reported the use of Mg-based composites to remove phosphates in contaminated synthetic effluents. For example, $MgFe_2O_4$/biochar composite adsorbed over 487 mg.g^{-1} at pH 3 and 20 °C. The maximum adsorption capacity of lanthanum-modified $MgFe_2O_4$-biochar alginate beads was approximately 27 mg.g^{-1} for an initial P concentration of 50 mg.L^{-1}, which is about 2 times better than pure $MgFe_2O_4$ (WANG, Li et al., 2020). Thus, a metamaterial composed of Mg-ferrite and MgO may have enhanced adsorption properties and can show improved P removal properties.

In fact, several efforts have been made to produce adsorbents with low synthesis cost and high adsorption capacity to be industrially feasible. Quyen and coworkers (2021) produced activated carbon fiber (CF) impregnated with lanthanum (La) at a cost of at least 310 USD.kg^{-1} of adsorbent. This composite was used 10 cycles to treat wastewater and maintained its efficiency over 80 % for removing phosphate. However, this adsorbent is not magnetic at room temperature and should not be used in magnetic remediation process, i.e., it may persist in the final effluent and the use of secondary process to recover the adsorbent might increase the cost of the wastewater treatment.

1.1 GENERAL OBJECTIVE

This study intends to develop new magnetic adsorbents based on Mg-Fe to remove phosphate from effluents.

1.2 SPECIFIC OBJECTIVES

- Investigate the influence of synthesis parameters (such as Mg/Fe molar ratio, calcination temperature and V-doping) on physical-chemical and textural characteristics of adsorbents and P adsorption efficiency;
- Study the effect of adsorbent dosage, initial P concentration, initial pH, and coexisting ions in the adsorption process;
- Understand the P adsorption mechanism;
- Evaluate the economic feasibility for adsorbents usage on P recovery.

1.3 STRUCTURE OF THIS DOCUMENT

This thesis is organized as follows:

In Chapter 1, it is introduced the problematic that will be approached through the next chapters.

Chapter 2 brings the current state of the research field that will be followed during the thesis. Concepts related to synthesis methods, adsorbent properties, and adsorption variables are explored.

In Chapter 3, the results of P adsorption using the Mg-Fe based composites synthesized via Sol-Gel method are presented. The content in this chapter was published by *Journal of Materials Science* in July 2023 (https://doi.org/10.1007/s10853-023-08734-7).

In Chapter 4, a Mg-Fe based composite doped with vanadium was synthesized through co-precipitation method, and P adsorption experiments were performed with a synthetic wastewater and sewage treatment plant effluent. An in-depth investigation of the adsorption mechanism was carried out. This chapter was published in the *Journal of Cleaner Production* in 2024 (https://doi.org/10.1016/j.jclepro.2024.143184).

2 STATES OF ART

This chapter will explore the current scenario of adsorption for phosphate removal and recovery, the main techniques for adsorbent synthesis, and aspects that affect adsorptive processes.

2.1 CURRENT STATE IN PHOSPHATE ADSORPTION

The challenges for the usage of conventional technologies (e.g., chemical precipitation and enhanced biological phosphorus removal (EBPR)) have been growing due to the requirements of regulatory agencies, since these methods have difficulty to achieve low phosphate concentration (< 0.1 mg.L^{-1}). Although it is possible to reach better removal efficiency (0.5 mg.L^{-1}) with the chemical precipitation, on the other hand, it is necessary to apply more metallic salts, which generate more sludge. For the most industrial scale EBPR systems, 0.5-1 mg.L^{-1} of phosphate can be obtained, but the process can be inhibited by organic matter loads, toxic species, and others inherent parameters of reactor operation. Thus, the significant progress of studies approaching adsorption to remove phosphate has demonstrated its competitiveness (KUMAR, Prashanth Suresh et al., 2019; WU, Baile et al., 2020). **Figure 1** shows a gradual and consistent increasing in the number of published papers in the last two decades that is intrinsically related to phosphate adsorption, showing that this area has been shown a strong interest of the entire scientific community.

Figure 1 – Publications that include the words "Adsorption" AND "phosphate OR phosphorus" in the title, abstract or keywords. Search engine: SCOPUS data retrieved on June 2024.

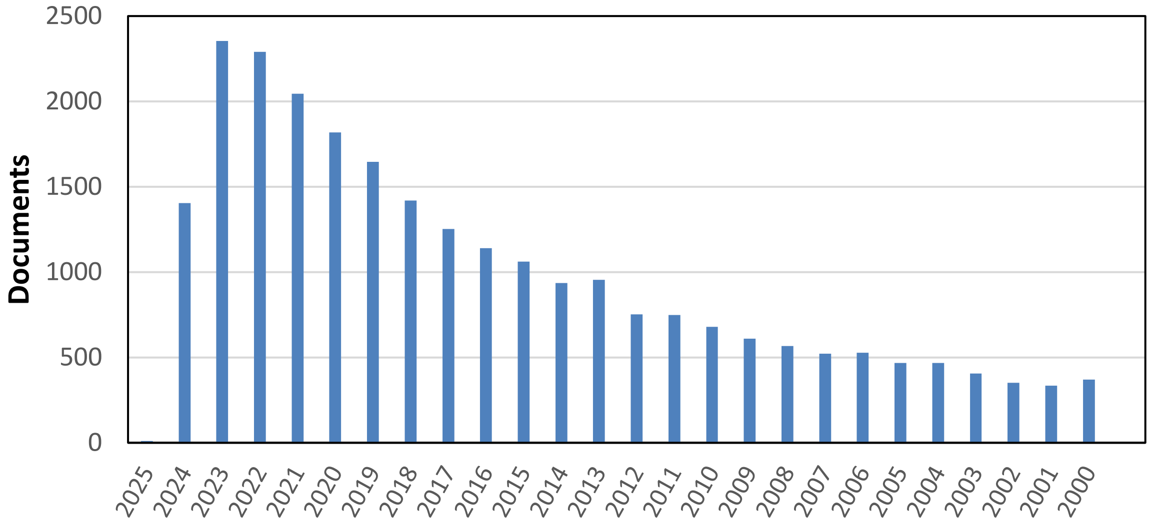

2.2 IMPORTANT ASPECTS ON ADSORPTIVE PROCESSES

The adsorption method has commonly been reported to achieve phosphate concentration below 0.1 mg.L^{-1} (WU, Baile et al., 2020). In addition, it favors a possible recovering of P by regeneration of the adsorbent removed from the effluent. However, it lacks information regarding its economic feasibility in large scale (most of works are done in laboratory scale and with rare information about the production and application costs). In other words, the main factor that encumber its employment are: (i) synthesis cost of adsorbent; (ii) adsorption capacity; (iii) adsorption kinetics, since the longer it takes to reach equilibrium, the greater has to be the volume of reactor or it has to work with lower volumetric flow; (iv) costs for adsorbent regeneration and neutralization of excessive NaOH in adsorbent; (v) number of cycles that adsorbent can be reused; and (vi) cost to recover phosphate as calcium phosphate or struvite (KUMAR, Prashanth Suresh et al., 2019). Therefore, in general, phosphate removal and recovery processes involve adsorption, desorption and recovery, as schematically plotted in **Figure 2**.

It should first be pointed out that the adsorption is a surface phenomenon process in which contaminants migrate and attach onto adsorbent surface either chemically by reactions or physically by potential barriers (WANG, Jianlong; GUO, 2020a). After adsorbent saturation, the desorption process is generally performed to recover adsorption capability of the material by a ligand switching place with phosphate (PATTAPPAN et al., 2023). Regarding P recovery after its adsorption, the precipitation process of P species with calcium can be easily employed. A molar ratio Ca/P > 1.6 is enough to precipitate phosphate as hydroxyapatite. Furthermore, an optimum pH between 7 and 9.5 leads to high P recovery and avoids the excessive generation of calcium carbonate (DENG, Linyu; DHAR, 2023).

Figure 2 – Stages involved in P removal and recovery by adsorption.

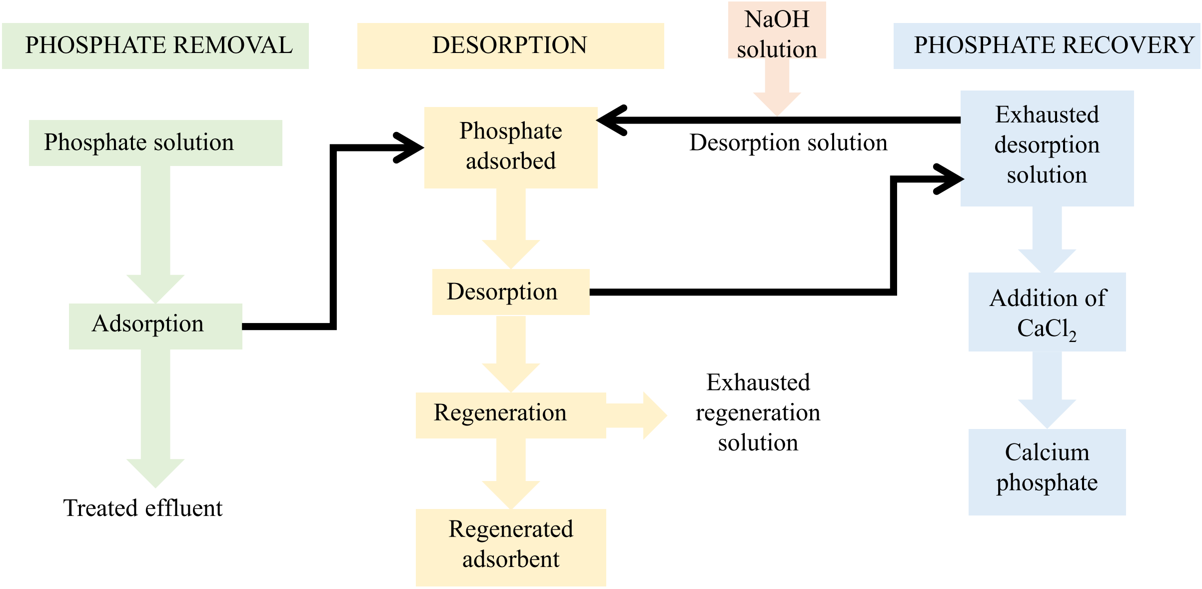

Source: Adapted from Baliarsingh and coworkers (2013).

Phosphate adsorption is intrinsically affected by several parameters, such as specific surface area, porosity, zeta potential and mineral composition In particular, some works have been shown that elemental composition (the presence of Mg, Ca, Fe, and Al) have a more important role than its surface area (ALMANASSRA et al., 2021; KUMAR, Prashanth Suresh et al., 2019; WANG, Jingxuan et al., 2023).

To understand the adsorption mechanism, it is important to perform experiments such as isotherm and kinetics, adsorbent performance with different pH environments, and selectivity, since these parameters impact the performance of adsorbent, and it may change the way as an adsorptive system must be operated. The mechanism can include electrostatic interactions, ligand exchange, precipitation, inner and outer-sphere complexation, and hydrogen bond (ALMANASSRA et al., 2021).

Electrostatic interaction is highly affected by pH of solution and the point of zero charge (pH_{PZC}) of the adsorbent. Therefore, electrostatic attraction occurs when $pH < pH_{PZC}$, because phosphate acquires a negative charge, while the adsorbent is positively charged. In contrast, if pH > pH_{PZC}, the electrostatic repulsion takes place, since the negatively charged surface of the adsorbent repels negative phosphorus species (ALMANASSRA et al., 2021). Some works have reported great adsorption efficiencies, even when pH is higher than the PZC of adsorbent, indicating that the adsorption involves more than one mechanism (ALMANASSRA et al., 2021).

Figure 3 – Phosphate speciation.

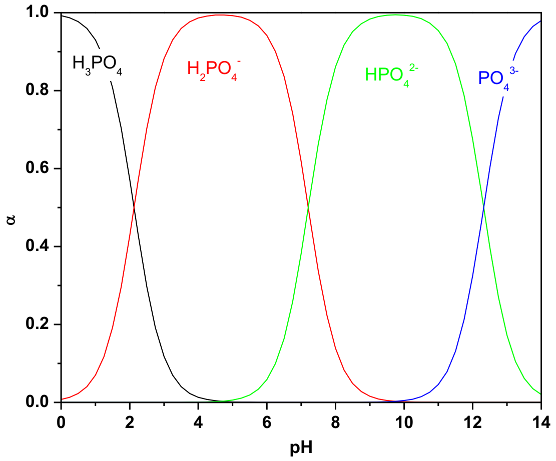

Source: Chent and coworkers (2021).

Ligand exchange consists of substituting a species adsorbed (such as hydroxyl groups) for another one (phosphate). This type of mechanism usually is reversible, suggesting that the phosphate can be recovered. Also, some phosphate salts have lower solubility and might precipitate on the adsorbent surface (ALMANASSRA et al., 2021).

It is common to have in effluent other ions (or organic and non-organic species) that compete for active sites of the adsorbent surface. An import aspect of selective adsorption is that the phosphate hydration energy is higher than other ions (such as sulfate, carbonate, chloride and nitrate), thus, it is necessary to surpass this energy to promote ion migration to another phase, and the process becomes inefficient for higher hydration energy (WU, Baile et al., 2020).

2.2.1 Adsorption kinetic

The adsorption kinetics are related to the rate at which solute adsorbs. It allows determining the time required to complete the reaction, and evaluate the scale and performance of adsorption equipment as well (QIU et al., 2009).

The pseudo-first order (PFO) model was first employed in 1898 by Langergren to describe the kinetic process of oxalic acid and malonic acid adsorption onto charcoal. The differential form of PFO model is (TRAN et al., 2017; WANG, Jianlong; GUO, 2020b)

$$\frac{dq_t}{dt} = k_1 \left(q_e - q_t\right) \tag{1}$$

Integrating the equation for $q_0 = 0$, it obtains

$$q_t = q_e\left(1 - e^{-k_1 t}\right) \tag{2}$$

Investigations about PFO model has shown that the process is related to (WANG, Jianlong; GUO, 2020b):

- High initial concentration of adsorbate;
- There is a limited number of active sites on the surface of adsorbent.

Ho proposed the pseudo-second order (PSO) model in 1995 to describe the adsorption of lead onto peat. The PSO model is written as follows (TRAN et al., 2017; WANG, Jianlong; GUO, 2020b)

$$\frac{dq_t}{dt} = k_2 \left(q_e - q_t\right)^2 \tag{3}$$

After integrating, it results in

$$q_t = \frac{k_2\, q_e^2\, t}{1 + k_2\, q_e\, t} \tag{4}$$

It is suggested from the PSO model that (WANG, Jianlong; GUO, 2020b):

- There is low initial concentration of adsorbate;
- Active sites are abundant.

Based on the literature, the PSO model has explained better the majority of kinetics experiments (**Table 1**). Somehow, it is difficult to compare the performance of materials presented in **Table 1** since parameters such as adsorbent dosage, P initial concentration and pH are not standardized.

Even though PFO and PSO are commonly used to describe kinetic data, it lacks a specific physical meaning since they are empirical models. Four main steps can control the adsorption process:

(i) bulk transport (mixing is usually enough to reduce its influence);

(ii) adsorptive attachment (very rapid step);

(iii) film diffusion (transport of adsorbed through the boundary layer to the external surface); and

(iv) intraparticle diffusion (adsorbate travels within the adsorbent pores).

Steps (iii) and (iv) are commonly stated as the limiting rate (WEBER, 1984). Thus, Weber and Morris have proposed the intraparticle diffusion (ID) model in 1962 given by (WU, Feng-Chin; TSENG; JUANG, 2009):

$$q_t = k_{s1}\, t^{0.5} \tag{5}$$

Table 1 – Adsorption kinetic models results employed for phosphate adsorption in literature

Adsorbent	Kinetic model	S_{BET} ($m^2.g^{-1}$)	Dosage ($g.L^{-1}$)	P initial concentration ($mg.L^{-1}$)	pH	q_e ($mg.g^{-1}$)	Reference
MgO coated Fe_3O_4@SiO_2 (FSM-1.5:1)	PSO	132.01	0.625	100	-	156.7	(LI, Shuangli et al., 2022)
MgO-biochar	PSO	-	2	400	9	200	(LIANG et al., 2023)
Mg-Al-CO_3 LDH/chitosan composite	PSO	28.47	0.3	50	5	119.71	(ISIDORO RIBEIRO et al., 2023)
MgBC600	PSO	98.5	0.5	100	7	104.76	(WANG, Chu-Ya et al., 2023)
MgO-modified biochar (MRS)	PSO	259	4	100	5.22	24.69	(TU et al., 2023)
MgO-ZrO_2 with hollow structure	PSO	31.8	0.5	100	7	88.2	(CHENG et al., 2022)
Mg modified multi-walled carbon nanotubes	PSO	139	0.4	100	-	154	(JIANG, Shoupei et al., 2021)
ACM-5:3 (Ca–Mg modified attapulgite)	PSO	21.45	0.3	20	-	~64	(KUANG et al., 2024)
MgO-expanded graphite composite	PSO	26.93	1	100	-	58.66	(SHIRAZINEZHAD et al., 2021)
Mg60Al40-LDH	PSO	-	0.4	50	-	53	(TONG et al., 2024)
$MgFe_2O_4$/biochar composite	PSO	172.81	0.2	100	-	165.49	(JUNG; LEE; LEE, 2017)
LDH-4	PSO	134.01	0.4	10	7	25	(XU, Yanming et al., 2024)

Regarding the ID model, it should be noticed that the experimental data of q_t versus $t^{0.5}$ must be plotted and if a straight line, obtained from the fit of the data, passes through the origin, the intraparticle diffusion governs the adsorption process. A negative intercept indicates a film diffusion controlling step, while a positive intercept suggests a fast initial adsorption uptake

(HU; PANG; WANG, 2022; ZHU, Qingyu; MOGGRIDGE; D'AGOSTINO, 2016). For multilinear processes which involve three steps: (i) it initiates by outer-surface adsorption or instantaneous reaction; (ii) next, there is a restriction due to the intraparticle diffusion; and (iii) finally, it reaches chemical equilibrium, and adsorbate slowly migrates from large pores to shorter pores (WU, Feng-Chin; TSENG; JUANG, 2009).

2.2.2 Adsorption isotherm

Adsorption isotherm consists of correlating adsorption capacity with concentration of contaminant at equilibrium stage (FOO; HAMEED, 2010; WANG, Jianlong; GUO, 2020a).

The Langmuir model was first proposed to describe the adsorption of gas onto solid. It assumes a monolayer adsorption (which means that the layer possesses one molecule thickness) that occurs for a finite amount of similar active sites with no side interaction nor steric hindrance between adsorbed molecules. It states that the adsorption is homogeneous, so each molecule has the same enthalpy and activation energy for adsorption. In this case, all sites keep the same affinities for the adsorbate. It is graphically characterized by a plateau that indicates equilibrium saturation, then all sites are fully occupied (FOO; HAMEED, 2010). Several materials in the literature have shown to follow Langmuir (Eq. (6)) and Langmuir modified models (**Table 2**).

$$q_e = \frac{q_{max}\, b\, C_e}{1 + b\, C_e} \tag{6}$$

The Freundlich isotherm describes non-ideal adsorption, i.e., adsorption processes that are not restricted to monolayer adsorption features. It is also an empirical model that can be applied to multilayer adsorption with non-uniform adsorption heat and affinities; therefore, it possesses a heterogeneous surface adsorption. The number of adsorbed molecules is the sum of total adsorption sites (each one with its own binding energy), and the sites with strong interactions are occupied first until the adsorption energy is reduced exponentially. The parameter 1/n varies from 0 to 1 and it indicates the adsorption intensity or surface heterogeneity (FOO; HAMEED, 2010).

$$q_e = k_f\, C_e^{\frac{1}{n}} \tag{7}$$

Table 2 – Adsorption isotherms models result employed for phosphate adsorption in literature.

Adsorbent	Isotherm model	S_{BET} (m^2.g^{-1})	Dosage (g.L^{-1})	Contact time (h)	P initial concentration (mg.L^{-1})	pH	q_e (mg.g^{-1})	Reference
MgO coated Fe_3O_4@SiO_2 (FSM-1.5:1)	Langmuir	132.01	0.625	5	10-250	-	222.2	(LI, Shuangli et al., 2022)
MgO-biochar	Langmuir	-	0.5	24	50-2000	5	1104	(LIANG et al., 2023)
MgBC600	Langmuir	98.50	0.5	12	0.5-160	7	109.35	(WANG, Chu-Ya et al., 2023)
Mg-Al-CO_3 LDH/chitosan composite	Freundlich	28.47	0.3	5	10-120	5	106.35	(ISIDORO RIBEIRO et al., 2023)
MgO-modified biochar	Langmuir	259	4	24	10-1000	5.22	167.3	(TU et al., 2023)
MgO-ZrO_2 with hollow structure	Langmuir	31.8	1	-	2-200	7	149.3	(CHENG et al., 2022)
Mg modified multi-walled carbon nanotubes	Langmuir	139	0.4	48	25-150	-	284	(JIANG, Shoupei et al., 2021)
MgO-expanded graphite composite	Langmuir	26.93	1	3	10-2000	-	491.6	(SHIRAZINEZHAD et al., 2021)
$MgFe_2O_4$/biochar composite	Sips	172.81	0.2	12	5-500	-	487.99	(JUNG; LEE; LEE, 2017)
ACM-5:3 (Ca–Mg modified attapulgite)	Langmuir	21.45	0.3	24	5-25	-	63.2	(KUANG et al., 2024)
Mg60Al40-LDH	Langmuir	-	0.4	1	1-50	-	108.8	(TONG et al., 2024)
LDH-4 (Mg-La binary layered double hydroxides)	Langmuir	134.01	0.4	1	10-100	7	85	(XU, Yanming et al., 2024)

2.3 ADSORBENT SYNTHESIS

It has widely been investigated the use of magnetic adsorbents to remove pollutants due to the possibility to recover the adsorbent by applying a magnetic field (ALMANASSRA et al., 2021).

There are two main approaches to synthesize metamaterials (**Figure 4**): *top-down*, which is known as a conventional technology that reduces the dimension of bulk materials to micro or nano scale; and *bottom-up*, which begins with atoms and molecules that form clusters, and then build micro and nanomaterials (PATRA; BAEK, 2014). In this regards, the Sol-gel and co-precipitation methods are widely used chemical methods that fit in the bottom-up approach (EL-KHAWAGA; ZIDAN; EL-MAGEED, 2023).

The parameters of synthesis (temperature, pH, and concentration of species) create a response, which is the desirable material that receives a series of particular characteristics (PATRA; BAEK, 2014).

Figure 4 – Routes to synthesize micro and nanomaterials.

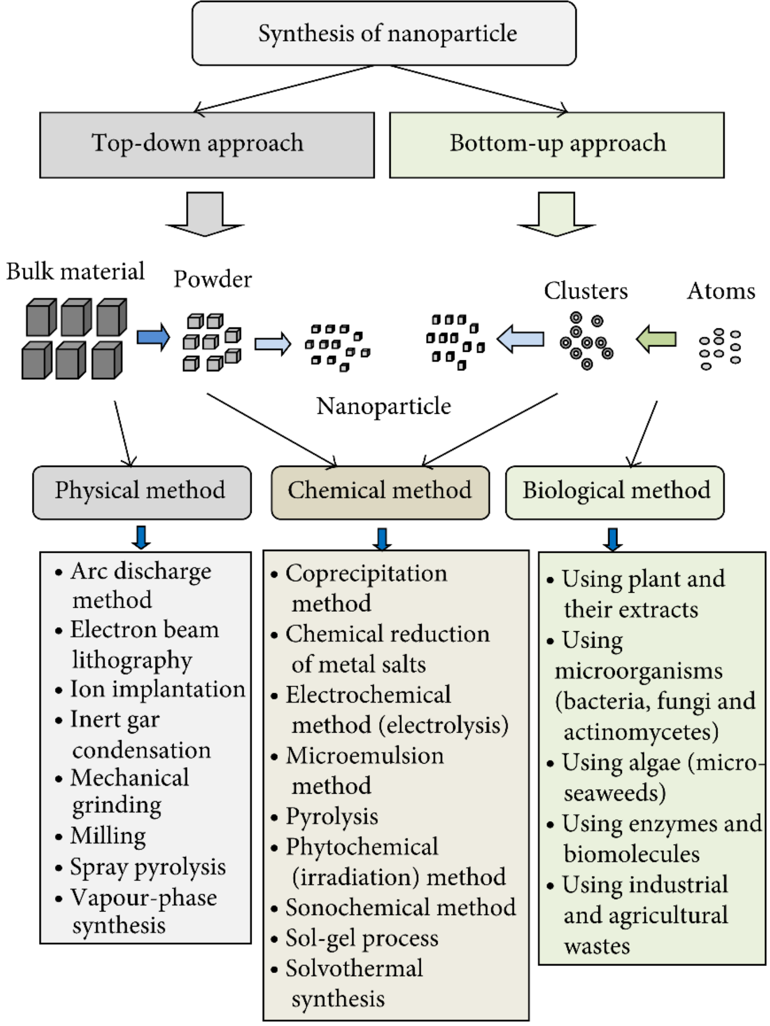

Source: Patra and Baek (2014)

2.4.1 Co-precipitation method

Co-precipitation is one of the first chemical methods to synthesize oxide-based adsorbents, it is versatile and widely employed (ABID et al., 2022).

During coprecipitation, multiple species must precipitate simultaneously from metallic salts, such as $M(OH)_2$ and $M(OH)_3$, by adding another solution with a precipitation agent, such as sodium hydroxide (NaOH). At the beginning of the precipitation, a high number of small particles are formed (nucleation). The particles tend to aggregate fast, which affects the size, morphology and properties of materials (**Figure 5**). The precipitation through chemical reaction is widely employed to result in species with low solubility (CUSHING; KOLESNICHENKO; O'CONNOR, 2004; SCHOLZ; KAHLERT, 2015) .

Precipitation can be favored by changing some parameters related to solubility (e.g., concentration of salts, pH, temperature, nature of basic solution). It is necessary to keep conditions close to the pH of a saturated solution to form high quantity of crystalline metal hydroxides (**Figure 6**) (BUKHTIYAROVA, 2019; SCHOLZ; KAHLERT, 2015).

Produced particles are collected by filtration or centrifugation. To remove impurities, the material should be washed with ethanol, distilled water or other solvents (ABID et al., 2022).

A post-treatment, such as calcination, is necessary to acquire a crystalline material with desirable morphology (ABID et al., 2022).

Figure 5 – Stages of co-precipitation method

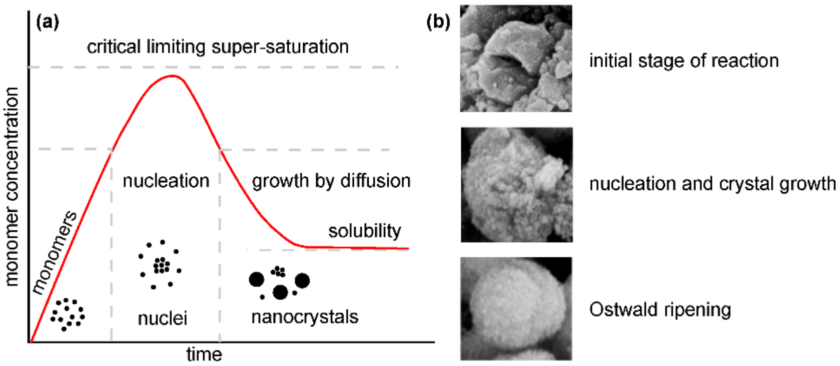

Source: Hornak (2021).

Figure 6 – Solubility of metal hydroxides in terms of pH.

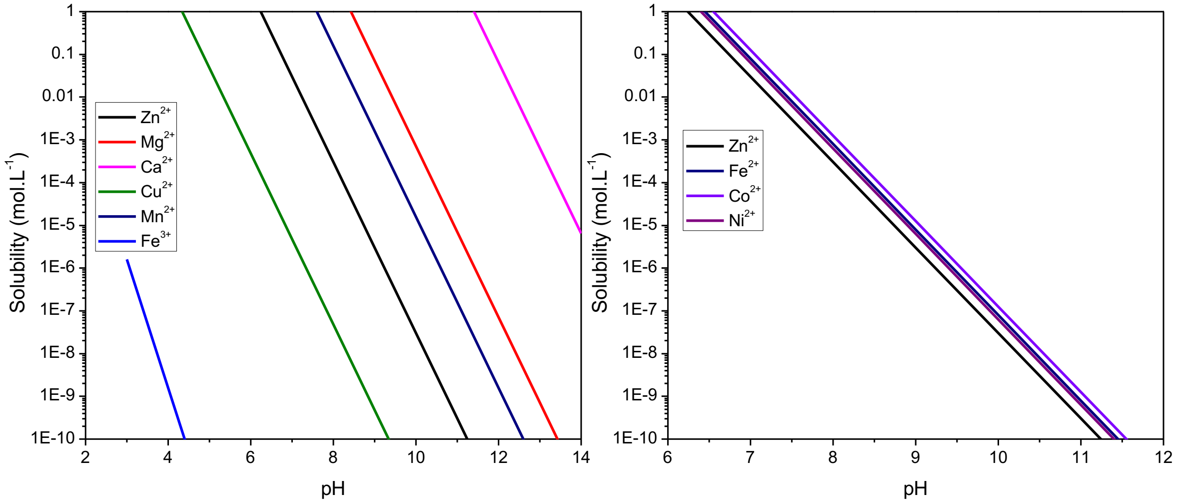

Source: Adapted from Scholz and Kahlert (2015).

2.4.1 Sol-Gel method

The Sol-gel is a well spread method due to its simplicity. Sol is a colloidal solution, and gel consists of a solid network structure dispersed in a liquid (ABID et al., 2022).

The Sol-gel method consists of the following steps (**Figure 7**) (PARASHAR; SHUKLA; SINGH, 2020):

1) Hydrolysis: Formation of stable solution (Sol) with colloidal particles after hydrolysis of precursor;
2) Condensation: Resulting in the oxides formation (Gel). The development of hydrolysis reaction and the condensation of polymeric networks lead to growth of clusters, which eventually collides with another ones and link to it. This process increases the viscosity of solvent and forms a porous structure.
3) Aging: while the aging process progresses, clusters continue to link together, this increases Gel thickness.
4) Drying: it is a critic step, since it changes the structural properties of Gel. By heating the Gel, the solvent evaporates. The xerogel formed possesses low surface area and pore volume, and high shrinkage of the gel.
5) Calcination: this step is set up to remove residues and water from the material. The calcination temperature and time is an important parameter to obtain a particular size and density of the sample.

Figure 7 – Steps involved in Sol-Gel method.

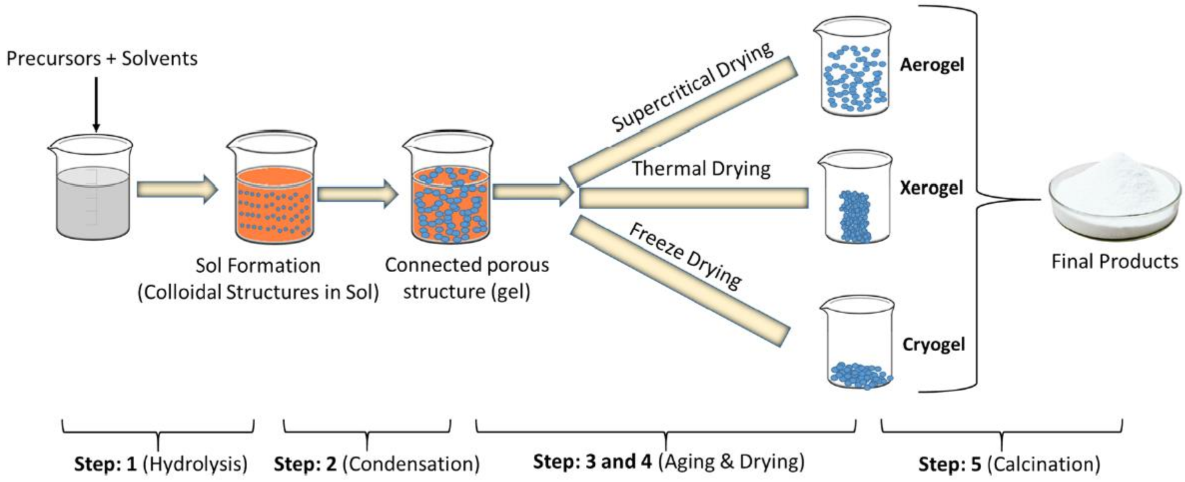

Source: Parashar et al. (2020).

2.5 ADSORBENT MATERIALS

It was previously mentioned that the phosphate adsorption is correlated to adsorbent surface properties, which the elemental composition of the adsorbent surface has a significant impact over other parameters.

Magnesium is an alkaline-earth metal well-known to have great affinity for phosphate due to its high electropositive. It was found by Li and coworkers (2022) (LI, Shuangli et al., 2022) that increasing the content of Mg in a MgO coated $Fe_3O_4@SiO_2$ improves its specific surface area and maximum adsorption capacity. Liang and coworkers (2023) (LIANG et al., 2023) also verified that adding more $Mg(NO_3)_2$ to the pyrolysis of peanut shell led to an enhancement of its porosity and adsorption capacity. Other works have evaluated the influence of Mg content in P removal (JIANG, Shoupei et al., 2021; SHIRAZINEZHAD et al., 2021).

Mg-based adsorbents can be found in a variety of forms: natural minerals (periclase, brucite, magnesite, dolomite); unsupported synthetic materials (nanosheets and microspheres); supported by organic materials (biochar) or oxides (diatomite, bentonite, ZrO_2) (SILVA; BALTRUSAITIS, 2020). Therefore, Mg-based compounds can be used as a matrix that support magnetic particles resulting in composites that can be used as a magnetic adsorbent for water remediation where phosphates are the main species that one desires to remove.

2.5.1 Spinel ferrite

Ferrites are chemical compounds with the general formula MFe_2O_4 (M is a bivalent metallic ion). There are, at least seven main ferrites (Mg^{2+}, Cu^{2+}, Mn^{2+}, Ni^{2+}, Fe^{2+}, Zn^{2+}, and Cd^{2+}) that crystallize in a structure called cubic spinel. The unit cell of spinel ferrites is formed by 32 oxygen atoms, 16 metal ions in octahedral sites (B), and 8 metallic ions in tetrahedral sites (A) (**Figure 8**) (BROCKMAN, 1951; MATHEW; JUANG, 2007). The existence of two types of sites (A and B) elapse of cations with different valence (ÖZGÜR; ALIVOV; MORKOÇ, 2009).

When A sites are occupied by M^{2+} cation and B sites by Fe^{3+} cation, it is a ferrite denominated as normal spinel (for example $CdFe_2O_4$ and $ZnFe_2O_4$). On the other hand, ferrites characterized with the A sites occupied by Fe^{3+} cation and B sites randomly constituted by M^{2+} and Fe^{3+}, it is called inverse spinel structure (such as $NiFe_2O_4$, $CoFe_2O_4$, $CuFe_2O_4$) (MATHEW; JUANG, 2007; REDDY; YUN, 2016). Of course, it can also obtain mixed spinel ferrites if sites are occupied in an intermediate way between normal and inverse structure, i.e., with fractions of M^{2+} ions in A and B sites (MATHEW; JUANG, 2007). In general, changing these occupations of A and B sites, magnetic properties, for instance, can be changed and applications can be proposed.

Regarding the magnetic properties of ferrites, its magnetization is related with the occupations of A and B sites and also the exchange interactions among them (ÖZGÜR; ALIVOV; MORKOÇ, 2009), features that lead the ferrites to an antiferromagnetic state (AF) as found in bulk $ZnFe_2O_4$, or ferrimagnetic-like state as commonly found in Ni, Co, Fe-ferrites, since the net magnetic moment will naturally occur due to the sum of individual moments of sub-lattices (MATHEW; JUANG, 2007). In mixed-spinel ferrites, such as $MgFe_2O_4$, a ferrimagnetic state is expected to happen.

At the moment, several ferrites have been employed to wastewater treatment (REDDY; YUN, 2016). However, Mg-ferrite and its composites have brought more attention for removing a variety of pollutants such as phosphate (JUNG; LEE; LEE, 2017), ciprofloxacin (HUYNH et al., 2023), chlorpyrifos (SHARMA; KAKKAR, 2018), and arsenic (UDDIN; JEONG, 2022b). The possibility of recover these adsorbents by applying an external magnetic field is one of the essential properties. Another great aspect of $MgFe_2O_4$ is that, until now, there is no sign of toxicity, since Mg is an important element for cell life (BECKER; KIRCHBERG; MARSCHALL, 2020; UDDIN; JEONG, 2022a).

Figure 8 – Crystalline structure of cubic ferrite

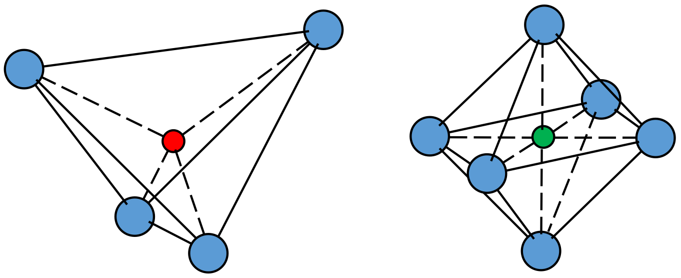

(a) Tetrahedral sites (A) (b) Octahedral sites (B)

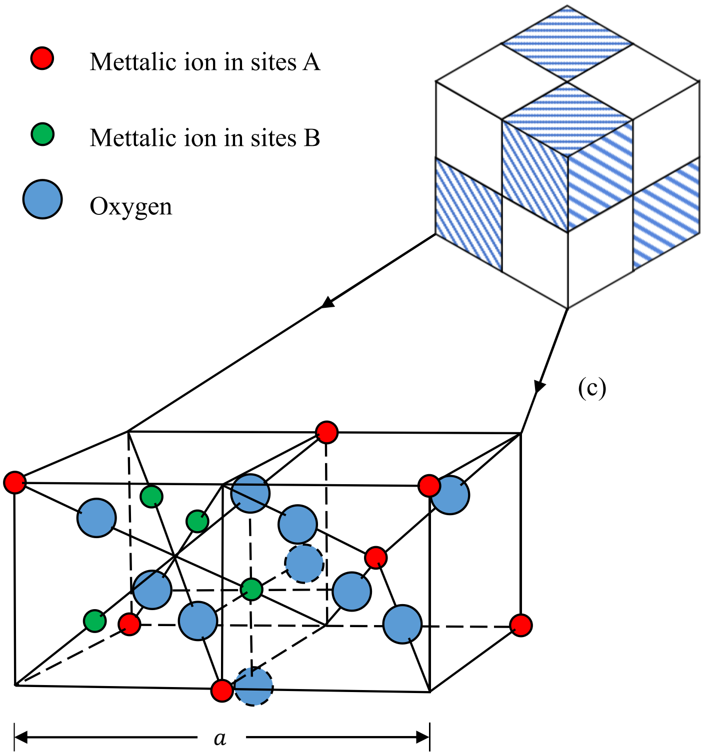

(d)

Source: Cullity and Graham (2019).

2.5.2 Magnesium oxide

In the literature, MgO is described as a material with low surface area and porosity. Thus, it often uses biochar and diatomite as supporting materials in order to obtain larger number of active sites. There are also ways to fabricate mesoporous MgO, since pore characteristics dictate phosphate transport through material, and, thus, the adsorption rate. It is important to mention that magnesium hydroxides partially dissolve in solution releasing Mg cations which combines with phosphates. This dilution increases pH and enable magnesium phosphate precipitation (LOGANATHAN et al., 2014). Therefore, performing BET and BJH analysis, one can bring some insights of the surface area loss and pores blockage in MgO phase after interaction, for example, with effluent rich in phosphates (SILVA; BALTRUSAITIS, 2020).

2.6 PRINCIPLES OF MAGNETISM

Applications of magnetic adsorbents have been based on the manipulation of its properties by exposing to an external magnetic field to separate the suspended adsorbent from water (MEHTA; MAZUMDAR; SINGH, 2015; MOHAMMED et al., 2017).

Regarding the magnetic behavior of adsorbents, some parameters are very important (**Figure 9**) (KIM; ZHAO, 2022):

i) magnetic susceptibility (χ_m): the magnetic response of material under an applied field of low intensity, i.e., how intense a material magnetizes (M) under an external magnetic field (H). This quantity is usually characterized by the slope of magnetizing curve ($\chi_m = \partial M / \partial H$);

ii) saturation magnetization (M_S): by increasing the H field strength, the adsorbent becomes further magnetized until all moments are fully aligned to the applied field direction, i.e., it reaches the saturation regime;

iii) remanence (M_R): it refers to the remaining magnetization after H field has been removed;

iv) coercivity (H_C): it corresponds to the resistance of materials to demagnetize, which means, it consists of the magnetic field necessary to make the magnetization zero. H_C fields larger than 400 Oe define hard magnets, while low (< 300 Oe) H_C field soft magnets. Superparamagnetic particles are those with net magnetization but due to its low magnetic energy (KV, where K is the effective magnetic anisotropy and V the particle volume) compared with the thermal energy (k_BT, where k_B is the Boltzmann constant and T temperature), the net magnetization fluctuates in time resulting in zero H_C field, for example.

As mentioned above, the spinel ferrites are usually classified by its magnetic properties as:

- Ferrimagnetic (FI): below critical temperature (T_N: Néel temperature) a spontaneous magnetization will appear due to the atomic exchange coupling of the two sublattices (A and B). The parallel coupling between spins of the M^{2+} (M a magnetic ion) and Fe^{3+} and the antiparallel coupling between spins of M^{3+} (M a magnetic ion) and Fe^{3+} and their different occupation fractions result in a net magnet moment (MORRISH, 2001);

Figure 9 – Magnetic hysteresis and influence of particle size on coercivity.

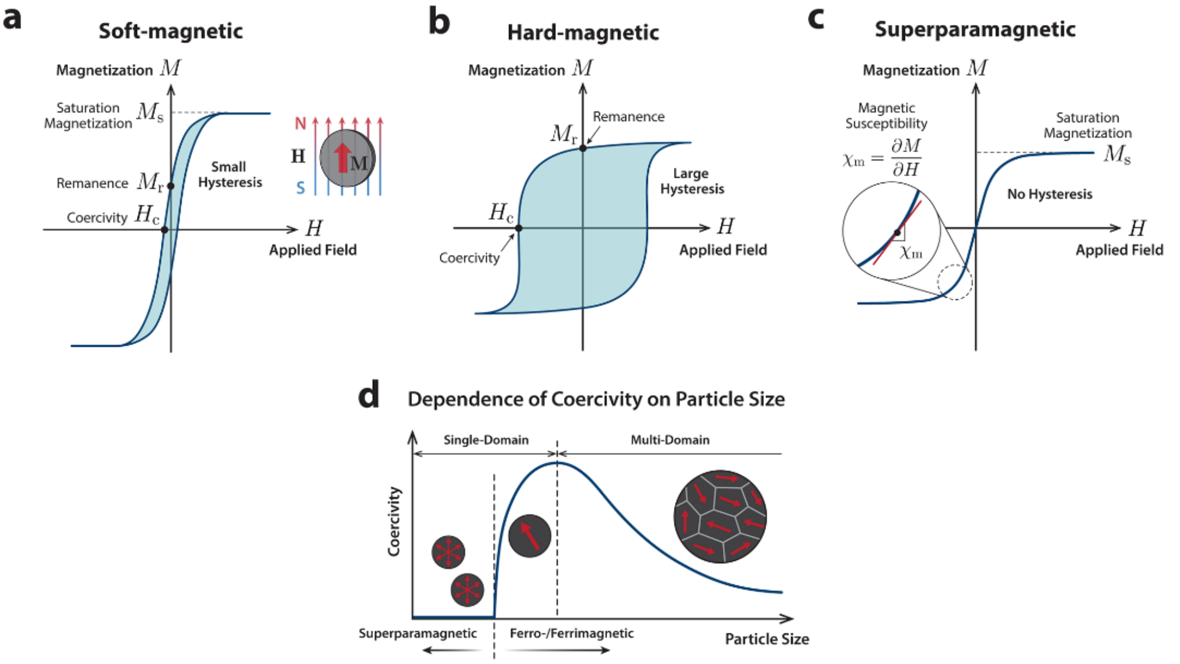

Source: Kim and Xuanhe (2022).

- Antiferromagnetic (AF): below a critical temperature (T_N: Néel temperature), where Fe^{3+} cations are equally distributed in B and A sites, and M^{2+} are nonmagnetic ions, the Fe ions couple antiparallelly, resulting in a magnetically ordered state, but with zero net magnetization (MORRISH, 2001);
- Superparamagnetic (SPM): this type of regime occurs with single domain particles that are in an ordered magnetic state (a net magnetization) like FI and ferromagnetic material. Consequently, it is related to size-dependent effect, i.e., as it is a phenomenon that depends on the competition between KV (anisotropy energy) and k_BT (thermal energy). For $KV > k_BT$, the particle will be in magnetically blocked state (non-zero magnetization and with H_C field), while for $KV < k_BT$ the particles show zero magnetization because the net spin is fluctuating in time. The possibility to have single or multidomain depends on the volume of the particle, because the domain wall thickness should be smaller than the particle volume in order to have magnetic multi-domains. In particular, nanoparticles with 10 nm to 20 nm do not possess multidomain, and single magnetic domain are found for sizes below 5 nm, of course, depending the material (ratio between the anisotropy constant and exchange interaction). In multidomain state the total magnetization is zero, but the material can be magnetized when it is exposed to external magnetic field (the saturation regime is reached usually in fields above 1 T in soft-magnets.

Thus, the magnetic dipole-dipole interactions of particles in remnant may yield a formation of clusters that reduce drastically the surface areas of adsorbent, concomitantly with a high possibility for pore blocking effect (MOHAMMED et al., 2017).

Ferromagnetic (FM) and Ferrimagnetic (FI) materials can be divided according to its hysteresis loop shapes. Hard magnetic materials (**Fig. 9b**) usually exhibit large hysteresis loops, with high coercivity values, while soft magnetic materials (**Fig. 9a**) have narrow hysteresis loops and small coercive force (SALIH; MAHMOOD, 2023).

3 PORE SIZE INCREASE IN SOL-GEL PREPARED NON-STOCHIOMETRIC MAGNESIUM FERRITE COMPOSITE DURING PHOSPHOROUS REMOVAL FROM WATER

The text of this chapter was published in *Journal of Materials Science* in July 2023 (https://doi.org/10.1007/s10853-023-08734-7).

This chapter describes the synthesis of $MgFe_2O_4$ and a Mg-Fe based composite via Sol-Gel method. The adsorbents were characterized by X-ray diffraction (XRD), ^{57}Fe Mössbauer spectrometry, and scanning electron microscopy with the option of Energy dispersive X-ray spectroscopy (SEM-EDS). The surface area (BET), pore size distribution (BJH), and pH of zero-charge are also determined. Adsorption experiments are performed to investigate the optimum dosage of adsorbent, the adsorption kinetic, the adsorption isotherm, the influence of pH on process efficiency, and multicycle reuse of adsorbent. The cost of adsorbent synthesis and adsorption process is also evaluated.

3.1 MATERIALS AND METHODS

3.1.1 Synthesis of Mg-Fe based composite via Sol-Gel method

The synthesis of adsorbent materials was adapted from Muniz and coworkers (2020) that used orange fruit residue to obtain pectin as substrate for the synthesis of Co-ferrite via Sol-Gel method. A schematic diagram of adsorbent preparation procedures is shown in **Figure 10**. Lemon peel was cut in small pieces in a blender and dried in an oven at 353 K for 24 h. Dried solids were milled in a blender and the fine particulates were separated by sieving through 200 meshes. The thin powder obtained from lemon peel was used as substrate to promote the Gel formation. For S-MgFeO precursor preparation, 50 mL of 20 $g.L^{-1}$ lemon peel particulate solution were mixed to 30 g $FeCl_2.6H_2O$ and 11,28 g $MgCl_2.6H_2O$. C-MgFeO precursor were prepared by mixing 11,28 g $FeCl_2.6H_2O$ and 30 g $MgCl_2.6H_2O$ in 50 mL of 20 $g.L^{-1}$ lemon peel particulate. These mixtures were dried in an oven at 353 K for 24 h. The precursors formed were calcinated at 673, 823 or 973 K for 2 h.

Figure 10 – Schematic image of the sample preparation route. The blue arrows indicate the sequence of similar parts of the sample preparation process. The red arrows show the route for the S-MgFeO sample, while the violet-arrow ones correspond to that for the C-MgFeO absorbent.

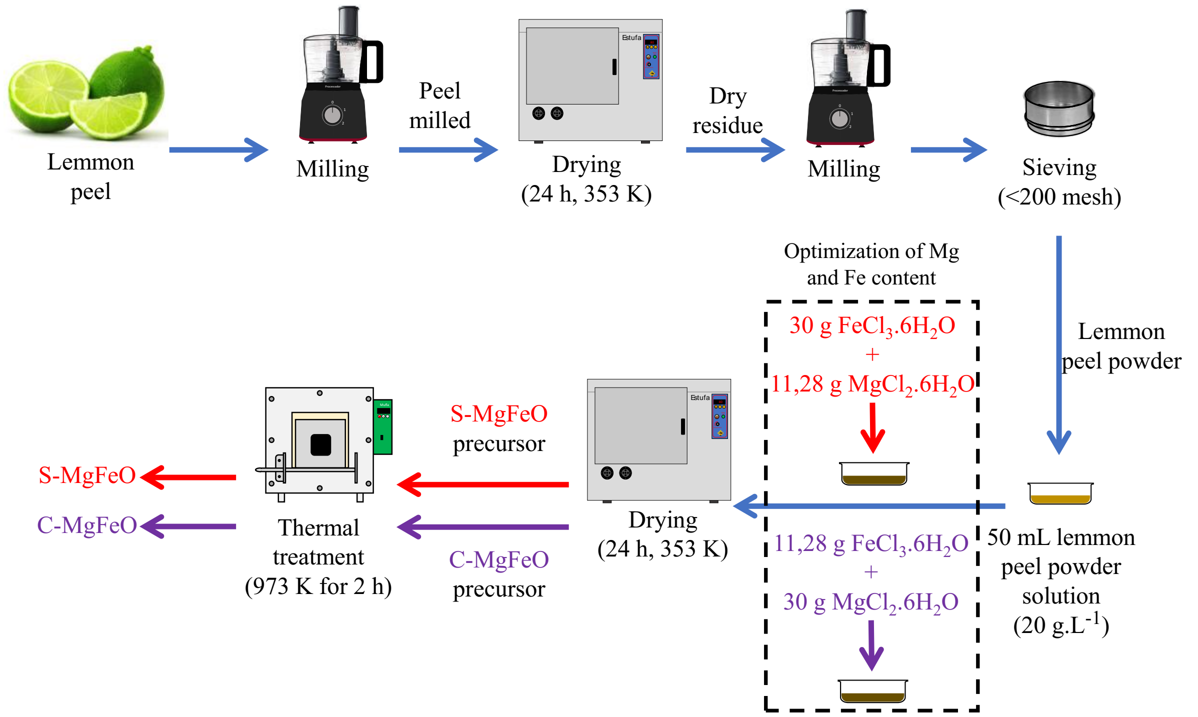

3.1.2 Characterization of adsorbent materials

X-ray diffraction (XRD) patterns were recorded at room temperature (RT) using a Rigaku Miniflex 600 diffractometer, operating with a Cu-Kα radiation source (1.5418 Å wavelength) for 2θ from 10° to 80° in a step of 0.02°. The XRD patterns were fitted by Rietveld refinement using the MAUD *software* (L.; S.; H., 1999). The following crystallographic files from COD (*Crystallography Open Database*) (GRAŽULIS et al., 2012) were used: MgO - COD ID 1011116, $MgFe_2O_4$ - COD ID 9001446, and α-Fe_2O_3 - COD ID 5910082.

15 K and 300 K ^{57}Fe Mössbauer spectra were recorded in transmission geometry with a non-polarized 50 mCi ^{57}Co:Rh source that was moved in a sinusoidal waveform of 12 Hz (512 channels not folded) and was kept at RT during the experiments. The 14.4 keV photons from the ^{57}Fe nucleus decaying were previously selected by a single channel analyzer and accumulated in a multichannel setup after passing by the sample (absorber). We used a thin layer of the powdered sample (approximately 0.5 mg ^{57}Fe/cm^2) mounted in an acrylic sample holder as an absorber. The spectrometer had its velocity calibrated with a thin foil of α-Fe at 300 K.

A Physical Properties Measurement System (PPMS Evercool-II), equipped with a vibrating sample magnetometer from Quantum Design, was used to obtain isothermal magnetic hysteresis (M(H)) loops at RT for a maximum field of 50 kOe (low-temperature magnetization experiments in the field-cooling protocol were also done, and the results show no significant changes when compared to those M(H) data reported here).

The textural properties, including surface specific area (SSA) and pore size distribution, were determined by employing a Multi-Brunauer–Emmett–Teller (BET) point plot (BRUNAUER; EMMETT; TELLER, 1938). The BET-specific surface area analysis was performed using Quantachrome Autosorb-1 equipment. Samples were outgassed for 24 h at 598 K before each isotherm measurement.

The surface morphology of the adsorbents was analyzed with scanning electron microscopy (SEM, HITACHI TM3030) coupled with energy-dispersive spectroscopy (EDS) operating with a voltage of 15 kV.

The point of zero charge (pH_{PZC}) was measured by preparing P-rich solutions with pH adjusted between 3 to 10, and the procedure was done as reported in the literature (PINOTTI et al., 2022). Concentrations of 5 $g.L^{-1}$ of S-MgFeO (or 0.6 $g.L^{-1}$ of C-MgFeO) were placed in 40 mL of 50 $mg.L^{-1}$ P solutions and stirred for 24 h, long enough to have stable pH.

3.1.3 Phosphorus adsorption experiments

The influence of adsorbent dosage and calcination temperature on the phosphate removal efficacy was investigated using 50 ppm phosphorus synthetic solution. Experiments were performed in a batch system with a magnetic stirrer for 24 h. The adsorber was removed by filtration and phosphorus concentration was found using the vanadomolybdate colorimetric method based on APHA 4500-P procedure (BAIRD B.; EATON D.; RICE W., 2017). Phosphorus solution (50 $mg.L^{-1}$) was prepared dissolving 0.1098 g KH_2PO_4 anhydrous to 500 mL of distilled water.

Adsorption kinetic experiments were performed for 5 $g.L^{-1}$ of each adsorbent in 200 mL of 50 $mg.L^{-1}$ phosphorus solution at natural pH ~5.4. The suspension was stirred and 20 mL aliquot was taken (using a polyethylene syringe) for phosphorus analysis at different contact times.

Adsorption isotherms were performed by applying 5 $g.L^{-1}$ of adsorption in a 50 $mg.L^{-1}$ of a phosphorus solution. The adsorption system was kept stirring for 24 h to ensure that the equilibrium was reached.

The influence of pH on the adsorption efficiency was evaluated on the pH range of 3 to 10. The initial pH of 50 mg.L^{-1} phosphorus solution was adjusted by 0.1 N NaOH and 0.1 N HCl. For C-MgFeO material, 0.6 g.L^{-1} was added to 40 mL of phosphorus solution, while 5 g.L^{-1} of S-MgFeO material were applied in 40 mL phosphorus solution.

The multicycle reuse of adsorbents was performed with the optimized adsorbent dosage to remove at least 90 % of phosphate. The initial concentration was 50 mg.L^{-1} and contact time of 24 h. Treated effluent was filtrated and the collected remaining adsorbent was dried at 373 K in an oven for 1 h. Then, the dried adsorbent was reused with no chemical treatment to investigate its regeneration.

3.1.4 P quantification by vanadomolybdophosphoric acid (APHA 4500-P)

The colorimetric reagent is prepared from 2 solutions (A and B). Solution A consists of 25 g of ammonium molybdate dissolved in 300 mL of deionized water. For solution B, 1.25 g of ammonium metavanadate is dissolved in 300 mL of deionized water until vaporization begins. Solution B is cooled, and 330 mL of concentrated HCl is added. Finally, solutions A and B are mixed and diluted for 1 L, which forms the colorimetric reagent.

For P quantification, 5 mL of sample were mixed with 1 mL of distilled water in a glass tube. Then 1.5 mL of colorimetric reagent were added to the tube and shook for 30 s. 10 min must be waited for UV-Vis analysis at 470 nm.

3.2 RESULTS

3.2.1 Characterization of synthetized adsorbent materials

Figure 11(a) shows the X-ray patterns for the adsorbent materials synthetized by the Sol-gel method with three different calcination temperatures and two different Mg-Fe mass ratios. During the preliminary tests, we investigated the best annealing temperature to produce stoichiometric (S-MgFeO) and non-stoichiometric (C-MgFeO) adsorbents. It was observed some undesirable phases (Mg(OH)Cl and $MgCl_2.6H_2O$) for an annealing temperature of 400 °C. Also, materials absorbed a lot of moisture over time. S-MgFeO calcinated at 550 °C had the lowest adsorption efficiency (~25 %) and high amount of $\alpha - Fe_2O_3$. It can be noticed that the best temperature to obtain the high amount of $MgFe_2O_4$ and MgO phases was 700 °C. Therefore, relatively high pure $MgFe_2O_4$ (~89 %) and $MgO/MgFe_2O_4$ composite (100 %) were obtained when the S-MgFeO and C-MgFeO precursors were calcinated at 700 °C, respectively (**Table 3**), indicating that an excess of MgO in the C-MgFeO sample reduced the undesired antiferromagnetic $\alpha - Fe_2O_3$ phase. For this reason, most of the adsorption tests will be done using the samples calcinated at 700 °C.

Table 3 – Phase contents and crystallite sizes from the Rietveld refinements of the DRX diffractograms for samples calcinated at 700 °C.

Sample	Phase (%)			Crystallite size (nm)
	$MgFe_2O_4$	MgO	α -Fe_2O_3	
S-MgFeO_700	89	-	11	250
C-MgFeO_700	34	66	-	244

The N_2 adsorption isotherms curves for the adsorbent materials calcinated at 700 °C are represented in **Figure 11(b)**. According to IUPAC (THOMMES et al., 2015), pores can be classified as: micropores for size < 2 nm, mesopores for size < 50 nm, and macropores for size > 50 nm.

Type-II isotherm is related to non-porous or microporous adsorbents, leading to a multilayer adsorption (**Figure 11(b)**). On the other hand, the type-IV isotherm possess a hysteresis loop related to the connection of a various sized pores (e.g., adsorbent develops considerable micropore and mesopore, except non-macropore), favoring a hysteresis associated with a capillary condensation.

Figure 11 – (a) XRD patterns and (b) BET isotherm of the S-MgFeO and C-MgFeO samples for different calcination temperatures (400, 550 and 700 °C).

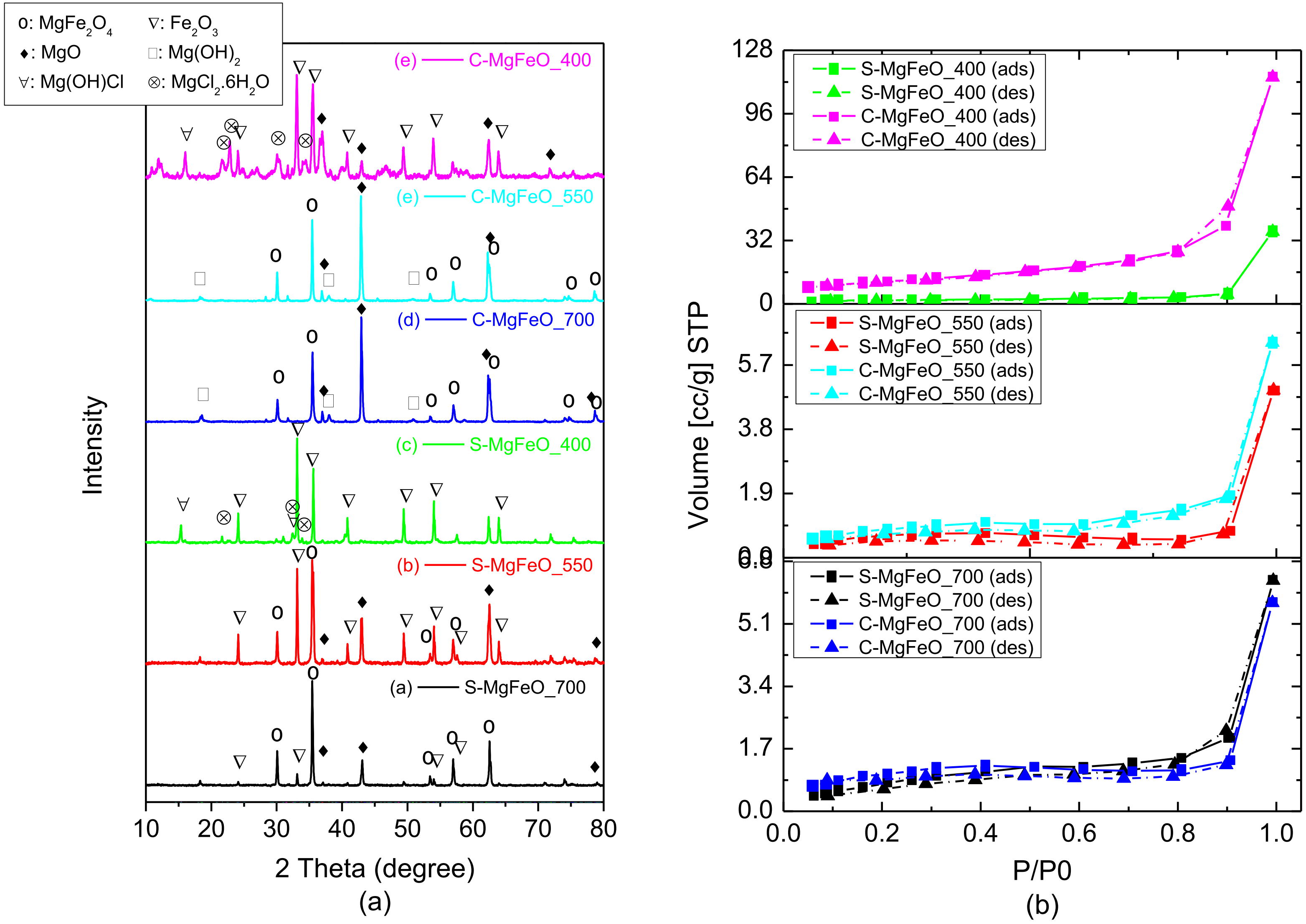

(a)

(b)

Increasing Mg content improved the BET surface area for all calcination temperatures. It can be noticed that the BET surface area for the C-MgFeO and S-MgFeO materials decreases in the following order of calcination temperature: 400 > 700 > 550 °C.

However, after P adsorption, S-MgFeO_700 and C-MgFeO_700 have shown higher specific surface area (SSA) and pore size. Therefore, BET and BJH data (**Figure 12** and **Table 4**) suggest that phosphates intensify "chemical erosion" since (i) the increment of SSA is more remarkable for C-MgFeO_700, which has higher P adsorption efficiency than for S-MgFeO_700, and (ii) there is an enlargement of pores after P adsorption.

Since S-MgFeO_700 and C-MgFeO_700 have pores at the micropore and mesopore regions (based on the BJH curve at the supplementary materials), the isotherms for these adsorbents are classified as type-IV. Magnesium ferrite synthetized by Ivanets and coworkers (2021) was also characterized with a type-IV isotherm.

Table 4 – Results acquired from BET adsorption isotherms before and after P removal for samples calcinated at 700 °C.

Sample	Before P adsorption			After P adsorption		
	BET Surface Area $m^2.g^{-1}$	Pore Volume $cm^3.g^{-1}$	Average Pore Size nm	BET Surface Area $m^2.g^{-1}$	Pore Volume $cm^3.g^{-1}$	Average Pore Size nm
C-MgFeO_700	4	0.0088	9	23.8	0.077	13
C-MgFeO_550	3.1	0.0099	13	-	-	-
C-MgFeO_400	39.9	0.1774	18	-	-	-
S-MgFeO_700	3.3	0.0097	12	3.5	0.018	20
S-MgFeO_550	2.5	0.0077	12	-	-	-
S-MgFeO_400	6.5	0.0566	35	-	-	-

Figure 12 – BET and BJH data for C-MgFeO_700 and S-MgFeO_700 (a) before and (b) after P adsorption.

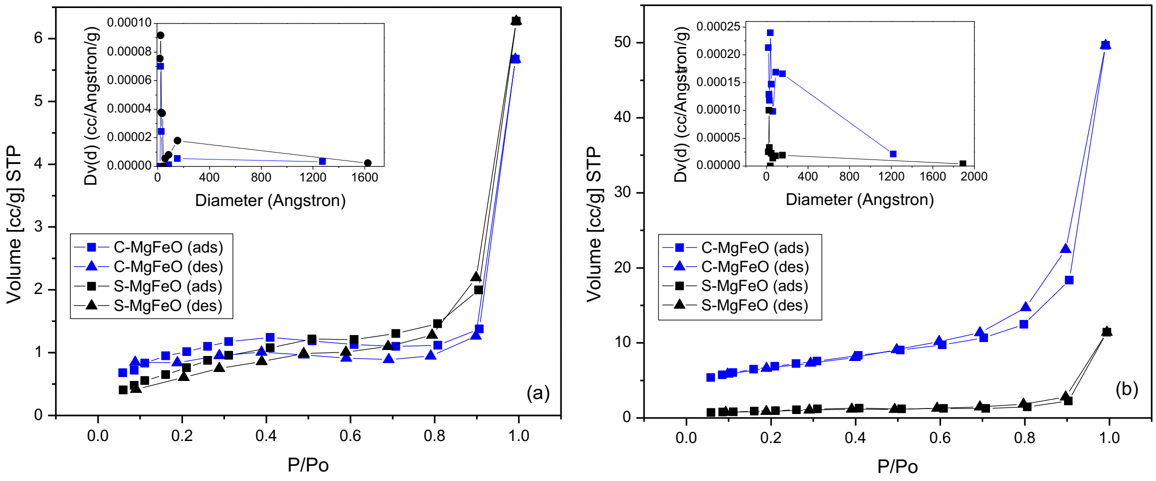

Evidence for an Mg-rich matrix was confirmed by EDS experiments shown in **Fig. 13** (right-hand side). From this figure, it is noticed dendrite-type forms of some grains in SEM micrographs (**Figure 13** (left-hand side)). Since, Mg species ($MgFe_2O_4$ and MgO) have great chemical affinity, they interact with each other (ISIDORO RIBEIRO et al., 2023; IVANETS, Andrei et al., 2021).

Figure 13 – MEV-EDS of (a, c) C-MgFeO_700 and (b, d) S-MgFeO_700.

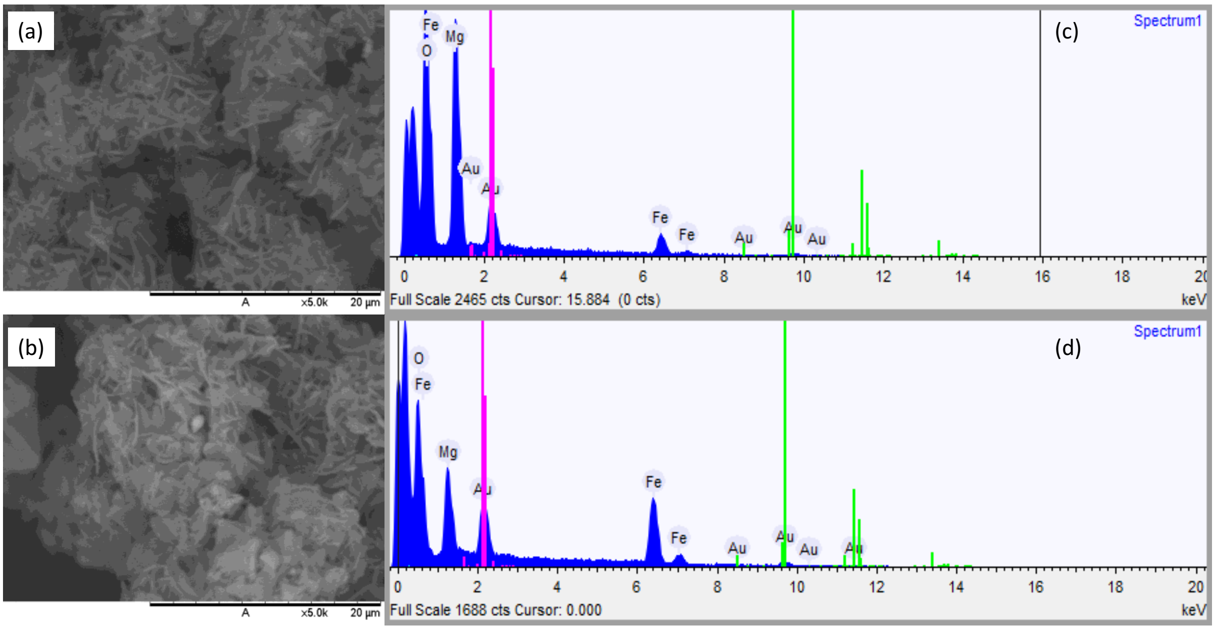

Figure 14 shows ^{57}Fe Mössbauer spectroscopy taken at 300 K (left-hand side) and at 15 K (right-hand side) before (top) and after (bottom) P adsorption for the i) S-MgFeO_700 and ii) C-MgFeO_700 samples. Six absorption lines compose the spectra as a result of nuclear Zeeman interactions between nuclear magnetic moment of ^{57}Fe and their hyperfine magnetic fields (B_{hf}). It is observed asymmetries in spectra due to Fe ions in different sites. The spectra were fitted considering up to five components, which are:

- Two sextets for Fe^{3+} ions in cubic spinel structure [A (red) and B (blue)];
- One sextet (orange) due to the Fe^{3+} ions in the hematite (α -Fe_2O_3) structure (only for S-MgFeO);
- One broad sextet (magenta) with Fe^{3+} features that can be attributed to Fe spin relaxation phenomenon or to chemical disorders found in Mg-ferrite crystal;
- One broad paramagnetic component (green) due to Fe ions in non-magnetically blocked state (small particles of ferrites in SPM state).

Based on the isomer shifts observed in the fits parameters presented in **Table 5**, Fe^{+3} ions of Mg-ferrite crystals randomly occupy the tetrahedral (A) and octahedral (B) configurations yielding a mixed spinel-like structure. This results in a non-zero net magnetic moment for Mg-ferrite crystals. A strong chemical disorder occurs resulting in Mg-rich regions for both adsorbents (this assumption is based on the features of the 4th-sextet-magenta component).

Figure 14 – 15 and 300 K ^{57}Fe Mössbauer spectra recorded for the i) S-MgFeO_700 and ii) C-MgFeO_700 samples. A (red color) and B (blue color) sextets are due to the Fe^{3+} ions in the spinel cubic structure of the Mg-ferrite, and the magenta sextet is due to Fe^{3+} ions at the particle surface where there is an enhancement of the gradient of Fe-composition. The orange sextet is due to α-Fe_2O_3 for S-MgFeO_700, while the dark-green doublet is due to the small grains of Mg-ferrite in C-MgFeO_700.

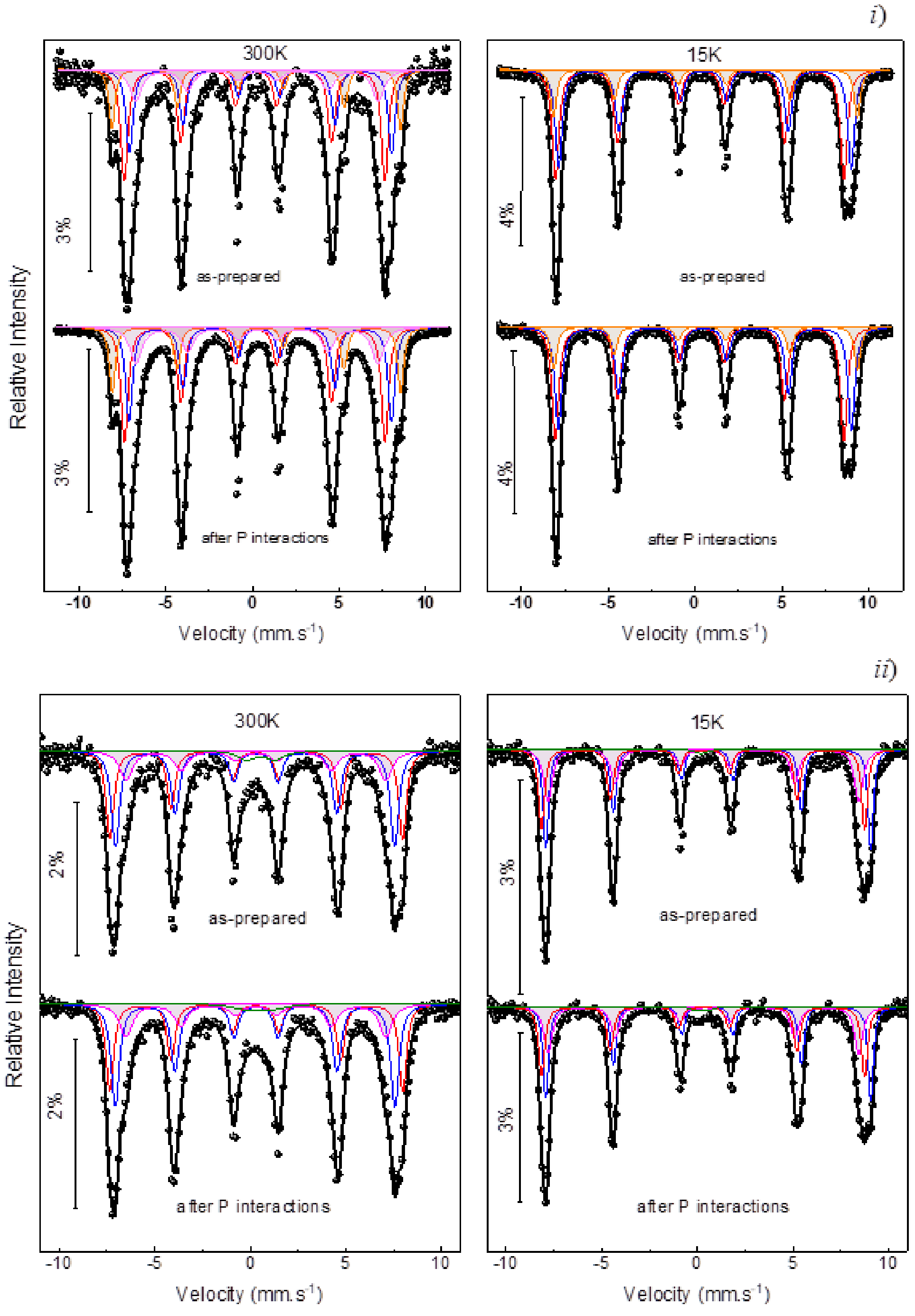

Table 5 – Hyperfine parameters obtained from the fits of 15 and 300 K ^{57}Fe Mössbauer spectra of the C-MgFeO sample before (as-prepared) and after its interaction with the effluent rich in P. δ is the isomer shift given relative to a-Fe at 300 K, $\Delta\varepsilon$ is the quadrupolar shifting, B_{hf} is the magnetic hyperfine field, and the fraction of each component is represented by the area in percentage.

C-MgFeO sample before (as-prepared) and after phosphorus interactions							
Sample	Mössbauer Parameters	Measurement Temperature (K)					
		15			300		
		$MgFe_2O_4$		broad-sextet (disordered)	$MgFe_2O_4$		broad-sextet (disordered)
		Site A	Site B		Site A	Site B	
As-prepared C-MgFeO	δ (mm.s^{-1})	0.46	0.27	0.23	0.21	0.18	0.21
	$\Delta\varepsilon$ (mm.s^{-1})	0.05	-0.08	-0.04	0.02	-0.05	-0.01
	B_{hf} (± 0.5 T)	52.7	50.4	52.4	47.4	45.0	43.0
	Area (%)	29	40	29	28	35	27
C-MgFeO+P	δ (mm.s^{-1})	0.38	0.27	0.26	0.21	0.18	0.20
	$\Delta\varepsilon$ (mm.s^{-1})	0.05	-0.07	-0.03	0.02	-0.05	-0.01
	B_{hf} (± 0.5 T)	53.4	50.6	52.4	47.5	45.4	42.1
	Area (%)	29	38	30	27	35	28

To understand the magnetic behavior of adsorbents, magnetic hysteresis (M(H)) loops were recorded, and the inset in **Figure 15** shows nonzero coercivity (H_C) fields, which suggest a soft ferrimagnetic state for both materials.

Figure 15 – M(H) curves recorded ca. RT for the S-MgFeO (black) and C-MgFeO (red) samples. The inset shows amplification of low field region, displaying the nonzero coercive field.

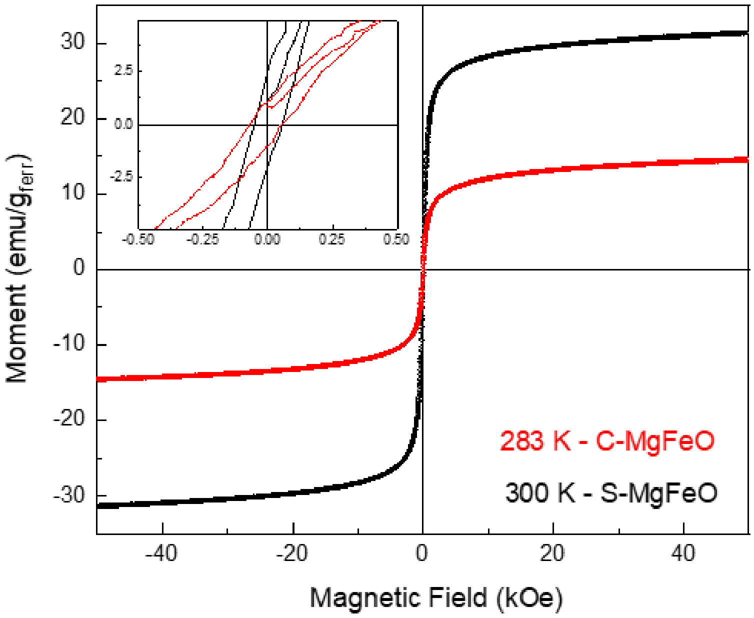

3.2.2 Adsorption experiments

3.2.2.1. Influence of calcination temperature and adsorbent dosage

To investigate the effect of calcination temperature, a series of different Mg-Fe based composites were synthetized at 400, 550 and 700 °C. Their adsorption capacities for phosphate removal were evaluated and the results are shown in **Figure 16(a, b)**.

It can be seen that phosphorus removal efficiency strongly depends on the calcination temperature for S-MgFeO. The phosphorus removal efficiency increased with adsorbent dosage due to higher number of active sites (SHARMA; KAKKAR, 2018). The best performance was observed for the adsorbent calcinated at 400 °C (~87 %), followed by 700 °C (~74 %), then 550 °C (~21 %) at 5 $g.L^{-1}$ S-MgFeO dosage.

The calcination temperature seems to not affect P adsorption efficiency for C-MgFeO. However, all materials produced by calcinating at 400 °C had the disadvantage of being hygroscopic, though, due to the presence of MgOHCl and other spurious phase (KASHANI-NEJAD; NG; HARRIS, 2004). After a month they got wet if kept in untreated air.

It can be noted that higher adsorption capacity was achieved for lower adsorbent dosage due to excessive amount of phosphorus, which leads to adsorbent saturation (YU et al., 2021). When adsorption dosage was 0.6 $g.L^{-1}$, the adsorption capacity of C-MgFeO_700 was 60 $mg.g^{-1}$, which reached the best result.

Comparing results for P removal and specific surface area, it can be denoted that there is no direct correlation between these two parameters. C-MgFeO_400 has a specific surface area 10 times larger than C-MgFeO_700, both obtained similar adsorption efficiency though.

Higher phosphorus removal can be achieved increasing Mg content in the adsorbent, which indicates that adsorption capacity depends mainly of Mg content. For S-MgFeO_700 the Mg/Fe molar ratio was 0.9, while C-MgFeO_700 was 5.7. Several works from the literature have demonstrated that the MgO phase provides active sites for phosphate adsorption. In particular, they revealed an existence of abundant Mg-O bonds on the MgO surface that can interact with phosphates by ligand exchange mechanism. Also, they have shown a high zeta potential of MgO, which means a surface positively charged, that guarantees electrostatic attractions to phosphates (LI, Anyu et al., 2022). Moreover, Luo and coworkers (2021) have found that biochar had low affinity to phosphate (P removal ca. 5 %), but after a treatment with KOH and functionalized with MgO, via stirring modification method, its P removal efficiency reached 84 %. Hence, the structure and content of MgO in the composite have significant affect phosphate adsorption. Also, Liang and coworkers (2023) modified biochar with MgO observing that the increase of Mg content led to higher adsorption capacities, while Wang and coworkers (2023) have modified bentonite by NaOH treatment and performed MgO impregnation to enhance affinity to phosphates. So, our composite with an excess of MgO keeps the higher phosphate adsorption.

3.2.2.2. Adsorption kinetic

Kinetic experiments were performed with an adsorbent dosage of 5 g.L^{-1}, and initial P concentration of 50 mg.L^{-1} (**Figure 16(c)**). Data fitted better to Weber and Morris model (Table *6*), and the process was divided in two steps (**Figure 16(d)**): (i) intraparticle diffusion; and (ii) chemical equilibrium. It can be stated that adsorption equilibrium in both materials is reached after ~12 h, and the adsorption capacities for C-MgFeO_700 and S-MgFeO_700 are 9.27 and 6.77, respectively.

Table 6 - Fit parameters obtained for the adsorption kinetics.

Model	Equation	Parameter	C-FeMgO_700	S-MgFeO_700
		q_e (exp)	9.4	7.9
Pseudo 1nd order	$q_t = q_e(1 - e^{-k_1 t})$	K_1	(0.21± 0.01)	(0.15±0.01)
		q_e	(9.5±0.2)	(7.8±0.3)
		R^2	0.989	0.9785
Pseudo 2nd order	$q_t = \frac{k_2\, q_e^2\, t}{1 + k_2\, q_e\, t}$	$K_2 q_e$	(0.25± 0.04)	(0.16± 0.02)
		$K_2 q_e^2$	(2.8±0.3)	(1.5±0.2)
		q_e	11.20	9.38
		K_2	0.022	0.017
		R^2	0.9741	0.9692
Weber and Morris (Stage I: intra-particle diffusion)	$q_t = k_{s1}\, t^{0.5}$	k_{s1}	(2.65±0.02)	(1.86±0.08)
		R^2	0.9994	0.988
Weber and Morris (Stage 2: intra-particle diffusion)	$q_t = k_{s2}\, t^{0.5} + I$	k_{s2}	(0.04±0.05)	(0.39±0.03)
		I	(9.2±0.3)	(5.4±0.1)
		R^2	-0.25	0.9896

Figure 16 – (a) qt vs adsorbent dosage, (b) phosphate uptake vs adsorbent dosage, (c) adsorption kinetic, (d) intraparticle diffusion model, (f) adsorption isotherm, (e) initial pH influence, and (g) multicycle reuse.

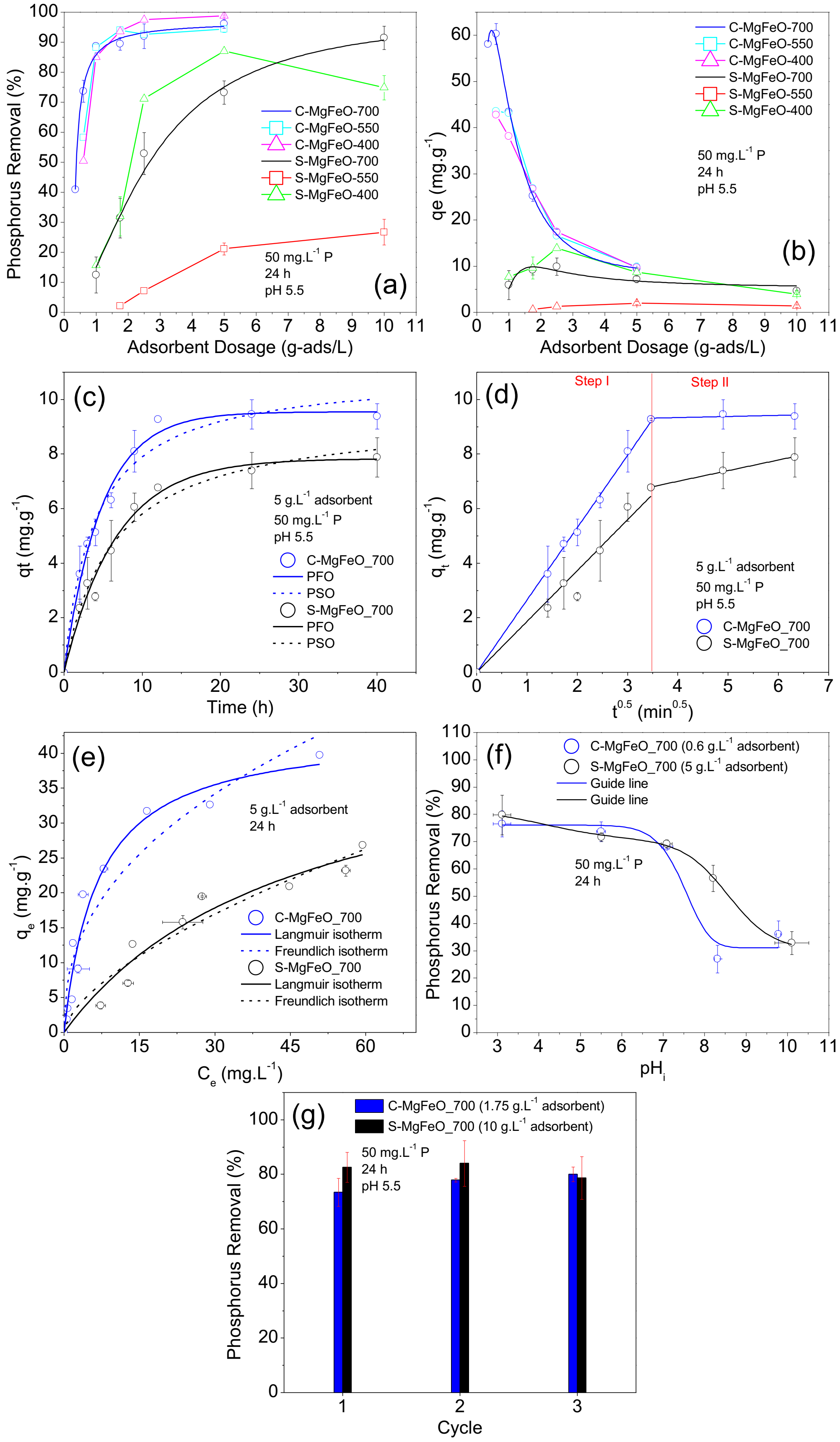

3.2.2.3. Adsorption isotherm

Isotherm studies were carried out for C-MgFeO_700 and S-MgFeO_700. **Figure 16(e)** shows adsorption capacities against phosphate equilibrium concentration. Experimental data for C-MgFeO and S-MgFeO were well fitted ($R^2 > 0.94$) by Langmuir model (**Table** *7*). This suggests that adsorption occurs in a monolayer, and there is no interaction between side active sites. The theoretical q_{max} value is (44 ± 3) $mg.g^{-1}$ for C-MgFeo_700 and initial P concentration of 250 $mg.L^{-1}$, while for S-MgFeO_700 obtained a q_{max} experimental lower than the fitted due to non-saturated regime in the initial P concentration range tested. Compared to other Mg-based materials reported in literature, C-MgFeO_700 has demonstrated great competitivity (**Table 8**).

Table 7 - Fit parameters obtained for the adsorption isotherms while using diverse models.

Model	Equation	Parameter	C-MgFeO	S-MgFeO
Langmuir	$q_e = \frac{q_{max}\, b\, C_e}{1 + b\, C_e}$	$q_{máx}$	(44 ± 3)	(45 ± 9)
		B	(0.15±0.03)	(0.022 ±0.008)
		R^2	0.9599	0.9469
Freundlich	$q_e = k_f\, C_e^{\frac{1}{n}}$	k_f	(8 ± 1)	(2 ± 0.1)
		n	(2.4 ± 0.3)	(1.6 ± 0.2)
		R^2	0.9075	0.9302

Table 8 - P adsorption parameters for different materials reported in the literature and results from this work.

Material	Model	Adsorbent dosage $g.L^{-1}$	P Concentration $mg.L^{-1}$	Experimental q_{max} $mg.g^{-1}$	Autor
C-MgFeO_700	-	0.6	50	(60 ± 2)	This study
C-MgFeO_700	Langmuir	5	10-250	(40 ± 2)	This study
$MgFe_2O_4$-BM-La(b)	-	0.6	50	26.8	(WANG, Li et al., 2020)
Mg-loaded biochar (BSB)	Langmuir	5	20-350	32	(JIANG, Yan-Hong et al., 2019)
MgO-modified biochar (MROBC)	Langmuir	2	10-600	28	(OGINNI et al., 2020)
20%Mg-BC	Langmuir	2	1-800	56.97	(DENG, Yu et al., 2021)
MgO-biochar (5MCB)	Langmuir-Freundlich	3.33	4-200	60	(ZHU, Danchen et al., 2020)
Mg-Al layered double hydroxides	Sips	4	10-400	47	(MAIA et al., 2021)
20%Al-BC	Sips	2	1-800	41.82	(DENG, Yu et al., 2021)

3.2.2.4. Effect of pH

During the experiments pH was performed between 3 and 10. Results revealed that adsorbents work better at low pH with PR % > 70 % (**Figure 16(f)**). It can be assumed that phosphate species are negatively charged. At the same time, pH of zero charge for adsorbents was around 10 (**Figure 17**), so that for all the experiments the adsorbent surface was positively charged ($pH < pH_{PZC}$), which attracted negatively-charged phosphates (LIU et al., 2018; RAZANAJATOVO et al., 2021). The electrostatic attraction can be considered as

Electrostatic attraction $\mathrm{M - OH_2^+ + H_2PO_4^- \rightarrow M - OH_2^+ \cdots H_2PO_4^-}$

Also, the excess of Mg may promote the formation of superficial hydroxyl groups that interact with phosphate species by ligand exchange mechanism. Indeed, it has been reported in the literature that ligand exchange process can be facilitated due to the protonation of surface OH groups at low pH solution, but excess of hydroxyl groups may compete for active sites in high pH (BALIARSINGH; PARIDA; PRADHAN, 2013; RAZANAJATOVO et al., 2021). This explains the loss of efficiency at alkaline environment for both adsorbents.

Ligand exchange: $\mathrm{M - OH + H_2PO_4^- \rightarrow M - H_2PO_4^- + OH^-}$

Besides the fact that pH of solution was higher after P adsorption implies that hydroxyl groups from adsorbent surface were released into solution, corroborating to ion-exchange mechanism (LONG et al., 2011; RAZANAJATOVO et al., 2021; ZHANG et al., 2018). This also helps us to understand the increase of pores and surface areas observed after phosphate-material interactions.

Figure 17 – pH of zero charge

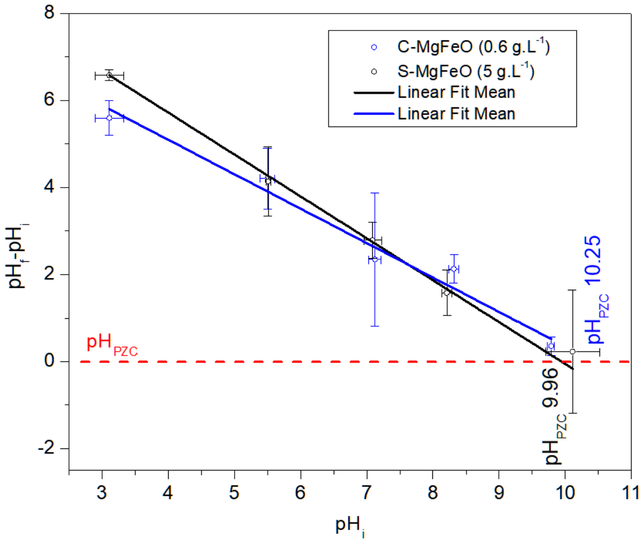

3.2.2.5. Multicycle reuse

Adsorbents were reused for three consecutive cycles with no chemical generation to evaluate its feasibility and obtain their maximum efficiency (**Figure 16(g)**). With the dosage stipulated for C-MgFeO_700 (1.75 $g.L^{-1}$) and S-MgFeO_700 (10 $g.L^{-1}$), it was expected to remove 90 % of P from a solution with 50 $mg.L^{-1}$ of phosphate. However, by increasing reactional volume over three times, adsorbent starts to agglomerate and a reduction of PR% was noticed. This problem could possibly be avoided using continuous flow or agitation at higher speeds in industrial processes. There is no significant loss in removal efficiency through the cycles for both adsorbents.

3.2.2.6. Cost evaluation

The estimated cost for using C-MgFeO_700 and S-MgFeO_700 is shown in **Table 9**. The cost of synthesis comprises energy and reagent cost, but the main expenditure is related to reagents. C-MgFeO_700 is cheaper than S-MgFeO_700, since part of $FeCl_3.6(H_2O)$ is substituted by a lower price salt ($MgCl_2.6(H_2O)$). Considering 1 kg of each adsorbent, C-MgFeO_700 can treat 1715 L of effluent, while S-MgFeO_700 treats 300 L. This fact makes the cost per liter of effluent of the former adsorbent 7 times lower than the later.

3.3 CONCLUSION

Ferrimagnetic magnesium ferrite and $MgO/MgFe_2O_4$ composite synthesized by sol-gel method were employed to remove phosphate from synthetic effluent. Adsorbents were characterized by X-ray diffraction, BET and BJH, ^{57}Fe Mössbauer spectroscopy, and magnetization experiments. Regarding P adsorption, it was investigated adsorption kinetics, isotherm, adsorbent dosage and pH dependence. Multicycle reuse of adsorbent was performed for three consecutive adsorption cycles. Also, the cost of adsorbent synthesis and effluent treatment were estimated. It was found that P adsorption is not related to specific surface area nor calcination temperature of adsorbent. Besides, EDS has shown that C-MgFeO was Mg rich. After P adsorption, it was noticed an enlargement of pores and enhancement of specific surface area. The isotherm followed Langmuir model suggesting monolayer adsorption, and kinetics were controlled by intra-particle diffusion step. Both adsorbents can be used for three cycles with no loss in removal efficiency. But the synthesis cost is lower for C-MgFeO, since it requires less amount of iron salt (which is expensive). Also, the cost for effluent treatment with C-MgFeO is cheaper than S-MgFeO since it requires lower adsorbent dosage to reach the same efficiency. Therefore, a change of Mg-Fe based adsorbent process brought a new competitive material to P removal that maintains its magnetic properties.

Table 9 - Cost evaluation of adsorbent synthesis.

Materials					
Material	Estimated mass to produce 1 kg of		Cost per kg (USD)	Total cost	
	S-MgFeO (kg)	C-MgFeO (kg)	**Cost per kg (USD)**	S-MgFeO ($USD.kg^{-1}$)	C-MgFeO ($USD.kg^{-1}$)
Lemons [1]	14.71	16.92	0.78	11.40	13.12
$FeCl_3 .6(H_2O)$	3.20	1.38	24.97	79.84	34.55
$MgCl_2 .6(H_2O)$	1.20	3.68	9.70	11.66	35.69
Total Material Cost				102.91	83.36
Energy					
	Lemmon peel drying	Precursor drying	Calcination	Drying before reuse (2 x)	Total
Time (h)	24	24	2	2	
Power expenditure (kW) [2]	1.5	1.5	3.72	1.5	
Energy Cost (USD) [3]	4.26	4.26	0.88	0.35	9.75
Total cost of synthesis per kg					
S-MgFeO ($USD.kg^{-1}$)			C-MgFeO ($USD.kg^{-1}$)		
112.65			93.10		
Estimated litters of effluent treated with at least 90 % phosphorous removal by 1 kg of adsorbent (pH 5.5)					
S-MgFeO (L)			C-MgFeO (L)		
300			1714.286		
Cost per litter of effluent treated					
S-MgFeO ($USD.L^{-1}$)			C-MgFeO ($USD.L^{-1}$)		
0.38			0.05		

4 PHOSPHOROUS MINING FROM MUNICIPAL SEWAGE TREATMENT PLANT EFFLUENT BY NOVEL V-DOPED Mg-Fe BASED COMPOSITE SYNTHESIZED VIA CO-PRECIPITATION ROUTE

Considering that (i) the previous $MgO/MgFe_2O_4$ composite revealed great adsorption efficiencies and (ii) rare-earth metals (e.g., Ce and La) have already tested for producing a composite that enhanced P removal, other d-elements should be also tested in the preparation of new magnetic nanoadsorbents for this purpose and also to open new applications to other contaminants. In this context, vanadium (V) could be used to prepare a multifunctional adsorbent since V-type composites are photocatalytic active under visible or natural light to degrade 2-chlorophenol (SALAH et al., 2016), methylene blue (BETTINELLI et al., 2007; RAMEZANPOUR; SHEIKHSHOAIE; KHATAMIAN, 2017), rhodamine B (TOLOMAN et al., 2016), acetaldehyde (YANG et al., 2007), i.e., showing its multifunctional features.

This chapter approaches to the synthesis of V-doped Mg-Fe based composite through the reverse co-precipitation method. Adsorbents were characterized by XRD, Fourier Transforms Infrared (FTIR) spectroscopy, SEM-EDS, TEM, ^{57}Fe Mössbauer spectroscopy, and their specific surface areas and pore size distributions were also determined as previously by BET and BJH data. Adsorption experiments with synthetic effluent are performed to evaluate the influence of: adsorbent dosage, initial phosphate concentration, removal efficiency over time, initial pH, and coexisting ions. Data from material characterization before and after P adsorption combined with adsorption experiments are used to propose an adsorption mechanism. Finally, 3 adsorption cycles with sewage treatment plant effluent followed by P desorption are performed to evaluate the feasibility of adsorptive processes.

The content of this chapter was published in the *Journal of Cleaner Production* in 2024 (https://doi.org/10.1016/j.jclepro.2024.143184).

4.1 MATERIALS AND METHODS

The following chemical compounds of analytical grade were used as obtained from Êxodo Científica: iron (III) chloride hexahydrate ($FeCl_3{\bullet}6H_2O$, P.A.), magnesium (II) chloride hexahydrate ($MgCl_2{\bullet}6H_2O$, P.A.), anhydrous potassium dihydrogen phosphate (KH_2PO_4, PA), and Sodium hydroxide (NaOH, PA). Hydrochloric acid (HCl, purity = 37%) and ammonium metavanadate (NH_4VO_3, PA) were purchased from Dinamica and Moderna, respectively. All reagents were used without further purification.

4.1.1 Synthesis of $MgO/MgFe_2O_4$ composite

Figure 18 is a schematic diagram of the synthesis process for the S and V-composites via reverse co-precipitation method (GUSATTI et al., 2011; MUSHARAF et al., 2021). At this method, the precursor solution is dropwise in a precipitant solution that ensures that the metal cations are in a supersaturated state and, thus, precipitate simultaneously. The advantage is a more homogeneous nano-material compared with the traditional co-precipitation method (HUIXIA et al., 2014; KARIMI; HASSANZADEH-TABRIZI; SAFFAR-TELURI, 2017). 2 M NaOH was prepared by dissolving 16 g of NaOH in 200 mL of deionized water. The metallic ions solution was obtained by dissolving the salts, as shown in Table *10*, in 50 mL of deionized water.

50 mL of 2 M NaOH was heated until it reached 343 K, and this temperature was kept constant. Then, 50 mL of the solution of metallic ions was dropwise added to the NaOH solution, while stirring for 45 minutes. After that, the mixture was cooled down to RT. Next, the mixture was filtered using a vacuum filter system, and the cake retained on the paper filter was denominated as the composite precursor. This powdered material was then calcinated at 973 K for 2 h to obtain the final composites, an optimum calcinated temperature previously determined according to the fraction of ferrite formation and also after P removal tests.

Figure 18 – Schematic image of the sample preparation route via Solochemical method.

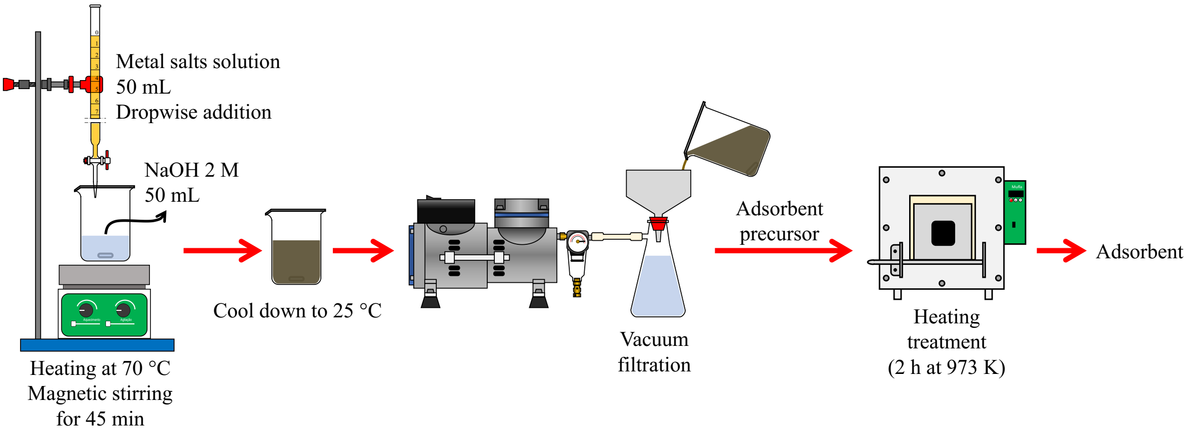

Table 10 – Summary of key synthesis parameters to be evaluated.

Material	NH_4VO_3 (g)	$MgCl_2.6H_2O$ (g)	$FeCl_3.6H_2O$ (g)	Calcination temperature (°C)
MgFeO	-	10.16	3.82	700
V-MgFeO	0.2338	10.16	3.82	700

4.1.2 Samples characterization

X-ray diffraction (XRD) patterns were recorded at RT using a Rigaku Miniflex 600 diffractometer, operating with a Cu-Kα radiation source (1.5418 Å wavelength) for 2θ from 15° to 80° in a step of 0.02°. The XRD patterns were fitted by Rietveld refinement using the MAUD software (L.; S.; H., 1999). The following crystallographic files from Inorganic Crystal Structure Database – ICSD were used: MgO – 064930, $MgFe_2O_4$ – 009939, and NaCl – 028948.

Fourier transforms infrared (FTIR) spectrum of adsorbents (before and after P adsorption) in KBr pellets was recorded using a Cary 660 FTIR spectrometer, ranging 4000 cm^{-1} to 400 cm^{-1}.

Quantachrome Autosorb-1 equipment was used to evaluate the BET-specific surface area and BJH-pore size distribution. Before recording the isotherms, the samples were outgassed for 24 h at 598 K.

The morphology of the nano-adsorbents was first obtained using a Scanning Electron Microscope (TermoFisher Scientific Quattro S) operating at 15 kV and coupled with Energy Dispersive Spectroscopy (EDS), the latter performed using a UltraDry ANAX-60P-B EDS detector from Thermo Scientific with an accelerating voltage of 20 kV. Also, JEOL 2100F Transmission Electron Microscope, operating at 200 kV, was used to get high resolution images. This JEOL microscope is equipped with an CMOS (ONE VIEW) camera and operates in three modes: transmission electron microscopy (TEM), High-Resolution TEM (HRTEM) and Scanning TEM (STEM), the latter allowed to perform the selected area electron diffraction (SAED). It has also an EDS setup that gives the elemental compositions using the STEM mode. EDS mappings were acquired using a probe with a diameter of 0.7 nm.

Transmission ^{57}Fe Mössbauer spectra were collected at RT and 19 K using a conventional spectrometer operating with a sinusoidal velocity sweep and a 25 mCi source of ^{57}Co in Rh matrix. In a Janis He closed-cycle setup, the source is kept at RT, but the sample went down to 19 K (this temperature difference in low temperature experiments yields the second-order Doppler shift contribution). The nylon sample containers were filled with the powder absorber, and its effective thickness was set to be around 0.1 mg ^{57}Fe per cm^2. The Mosswinn 4.0i program was used to fit the Mössbauer spectra.

4.1.3 Adsorption experiments with synthetic effluents

A set of adsorbent dosages (0.35-2 g.L^{-1}) was added to 50 mL of 50 mg.L^{-1} P solution for 24 h to evaluate the minimum adsorbent amount to reach 90 % of phosphorous removal. Therefore, to prepare 50 mg.L^{-1} P solution, 0.2197 g of KH_2PO_4 was solubilized in 1 L of deionized water.

An adsorption kinetic experiment was performed for 2 g.L^{-1} of adsorbent added to 100 mL of 50 mg.L^{-1} P solution, and aliquots were taken at predetermined times. The models described in Section 2.2.1. were used to evaluate the kinetic data.

For adsorption isotherms, P initial concentration varied from 25 mg.L^{-1} to 500 mg.L^{-1}, and the synthetic effluent was treated with 2 g.L^{-1} of adsorbent for 24 h. Data were fitted with the Freundlich and Langmuir isotherm model (Eq. 7).

No pH adjustment was performed for adsorbent dosage, kinetic, and isotherm experiments.

The influence of initial pH (50 mg.L^{-1} of P) was studied for 0.6 g.L^{-1} of adsorbent and a contact time of 24 h. NaOH 0.1 M and HCl 0.1 M were used to adjust pH.

Coexisting species competition was performed for 50 mg.L^{-1} of P solution and 15 mM of $NaNO_3^-$, SO_4^{2-} or CO_3^{2-}. The adsorbent dosage and contact time were 2 g.L^{-1} and 24 h. No pH correction was performed.

The phosphorus concentration was determined using the vanadomolybdophosphoric acid method based on the APHA 4500-P procedure (see Section 3.1.4).

Each adsorption experiment and adsorbent synthesis was repeated, at least, twice (replicated).

4.1.4 Reuse of adsorbents and P recovery from sewage

To test our magnetic adsorbent in a real effluent and to check its commercial feasibility, we have performed reuse and chemical regeneration studies using effluent from the municipal sewage treatment plant (**Figure 19**). The effluent after biological treatment (UASB reactor and submerged aerobic biofilter) was collected daily, and P concentration was determined as soon as the sample came to the laboratory. The adsorbents were reused 3 times with no chemical treatment. Then, P desorption was promoted by NaOH 1 M solution for 3 h. Before P quantification, samples were filtrated and centrifuged. This set of tests is not often found in the literature and it will bring some relevant contribution to this issue for the literature.

Figure 19 – Scheme of (a) batch adsorption with reuse and regeneration.

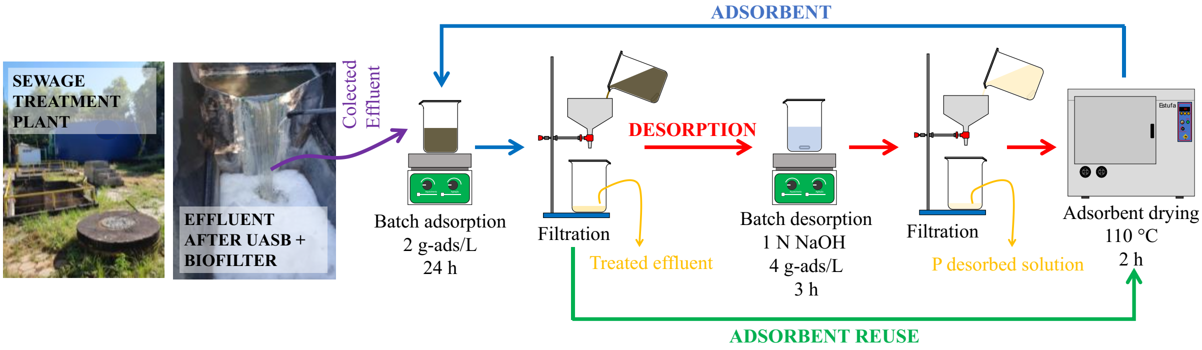

4.2 RESULTS

4.2.1 Characterization

XRD patterns of S- and V-samples before and after P adsorption are shown in **Figure 20(a, b)**. Phase contents were obtained by Rietveld Refinement. **Table 11** displays the results of their grain sizes and fractions obtained from the XRD refinements. As it can be noticed, the grain sizes of the MgO, $MgFe_2O_4$ phases are respectively ca. 50 nm and 30 nm, sizes in nanometric regime, allowing us to label the material as nano. It can be noticed that a high amount of NaCl was formed during NaOH and metal chloride's reaction. MgO and $MgFe_2O_4$ were also formed. After P adsorption, NaCl peaks were vanished at V-MgFeO sample and decreased significantly for the MgFeO sample, suggesting that NaCl leached to the solution. The presence of NaCl did not impact the adsorption properties of the composites, an assumption that is proven in multicycle reuse experiments. Adding a purification or washing step would increase the synthesis costs and waste generation, in other words, the main focus was a feasible process with cleaner production. In addition, for similar S-sample synthetized by SG method (composite with bulk-like phases), no trace of NaCl phase was detected and the P adsorption follow similar features to those that will be shown here, except that in the present case an enhancement of P removal was demonstrated by the experiments performed with the adsorbents synthesized by Sol-Gel. MgO content was higher than $MgFe_2O_4$ before P adsorption for both adsorbents. However, after phosphate adsorption, $MgFe_2O_4$ becomes the main phase from the X-ray point of view. We have observed that in phosphate solution, Mg-based adsorbents can release Mg^{2+}, as often reported in the literature (DENG, Yu et al., 2021; ISIDORO RIBEIRO et al., 2023; LIN et al., 2019; PINOTTI et al., 2023), and might justify a drop in MgO content. The presence of Mg^{2+} in solution could react with phosphate and forms magnesium phosphate, which can be easily adsorbed by metal oxides (LIN et al., 2019; LU et al., 2020; XU, Chenglong et al., 2023). This could explain the high adsorption capacity of the S- and V-samples, as will be discussed below. Consequently, the apparent absence of magnesium phosphate phase (for both samples after P adsorption) and also no evidence of vanadium oxide phase (for V-sample) in XRD diffractograms imply that these phases acquired amorphous-like structure and/or they have a low crystallinity, as reported in the literature (XU, Chenglong et al., 2023).

FTIR spectra of the S- and V-samples before and after P adsorption are respectively displayed in **Figure 20(c)** and **(d)**. A broad absorption band from 400 cm^{-1} to 760 cm^{-1} is a result from contribution of Mg-O, Fe-O, V=O, and P-O bonds that are superposed (no energy resolution in our spectra). On the other hand, the broad band from 765 cm^{-1} to 950 cm^{-1} for the V-MgFeO spectra before adsorption confirms the success of vanadium substitution, since this band is not observed at MgFeO and it is commonly assigned to V=O bond (WU, Yingjie; GAO; WU, 2015). Therefore, the assumption of V-substitution on the spinel cubic structure is supported by two facts (i) absence of V-oxide crystalline phase in the XRD pattern and (ii) substantial changes of Fe environments of the V-sample as seen by ^{57}Fe Mössbauer spectroscopy that will be discussed below. Peaks at 800 cm^{-1} to 1200 cm^{-1}, clearly seen in the samples after chemical interactions with phosphates, refer to P-O bonds validating the mentioned phosphate adsorption by our adsorbents. Deconvolution of FTIR spectra for V-MgFeO is shown in Figure *28*(c), and 2 point groups can be noticed (ELZINGA; SPARKS, 2007):

- C_{3V}: consists of 2 ν_3 bands located at 1078 cm^{-1} and 990 cm^{-1}, and 1 ν_1 band at 850 cm^{-1}, related to nonprotonated monodentate inner-sphere complex formation.
- C_{2V}: composed of 3 ν_3 bands at 1159 cm^{-1}, 1077 cm^{-1}, and 940 cm^{-1}, and 1 ν_1 band at 875 cm^{-1}, which can be assigned to monodentate binuclear or a bidentate mononuclear inner-sphere complex.

Figure 20 – Rietveld refined XRD patterns for the (a) S- and (b) V-samples [Legend - ●: MgO, ■: $MgFe_2O_4$, ▲: NaCl]; FT-IR spectrum of (c) S and (d) V; BET isotherm with inset of BJH pore-size distribution for (e) C and (f) V; M(H) curves recorded at RT for (g) S and (h) V. Both adsorbents were characterized before and after P adsorption. Legend: VA and SA are V- and S-samples after P adsorption; VR and SR are V- and S-samples after adsorbent alkaline regeneration.

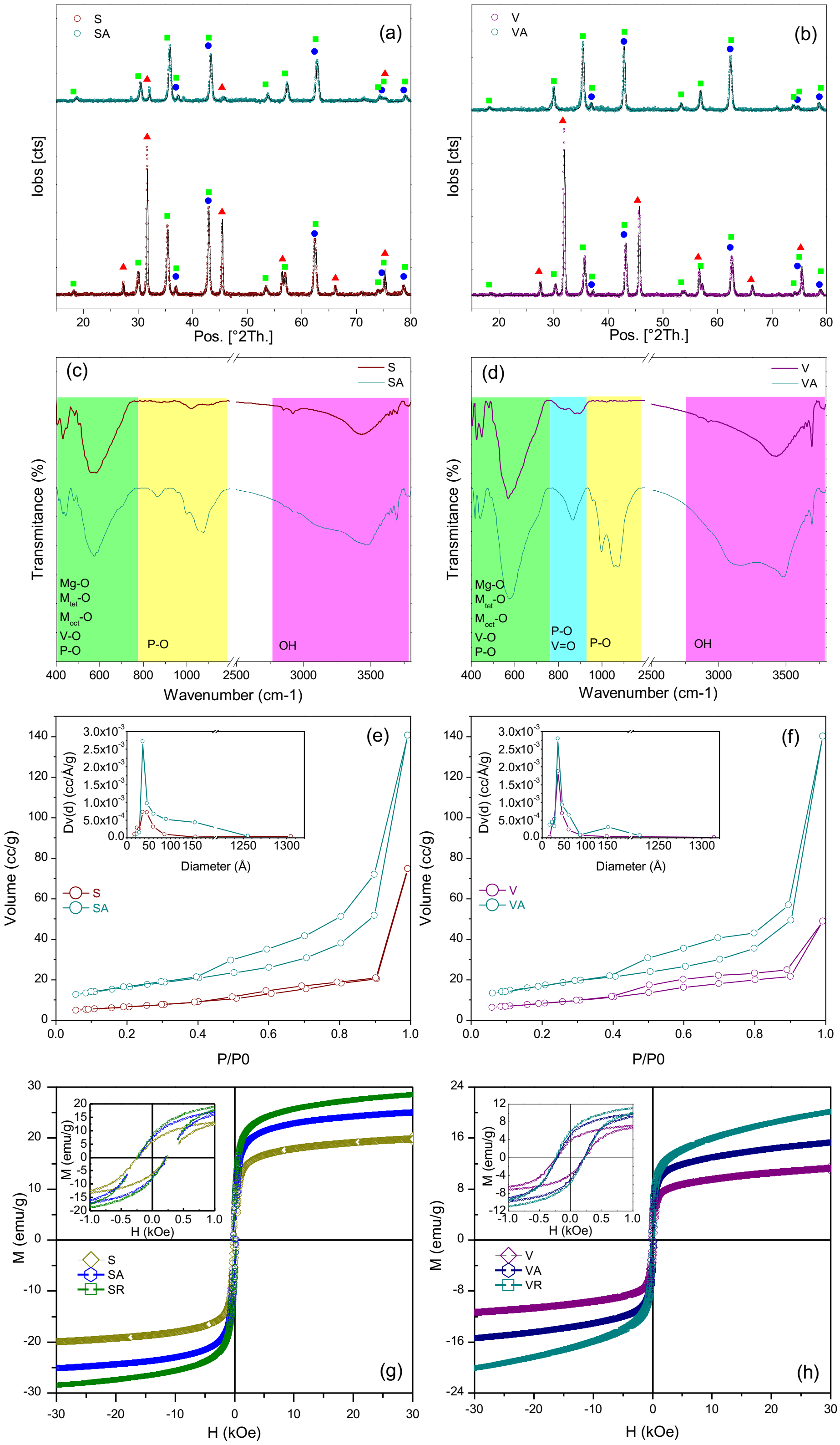

Table 11 – Phase contents and crystallite sizes obtained from the Rietveld refinements of the XRD diffractogram, results acquired from BET adsorption isotherms, molar ratios obtained from EDS, magnetization characteristics from hysteresis loos, and pH of zero charge before and after P removal.

	Sample	DRX					N_2 adsorption (BET and BJH)			Atomic ratios from EDS (%)					Magnetization			pH_{PZC}
		Phases			Crystallite size nm													
		$MgFe_2O_4$	MgO	NaCl	$MgFe_2O_4$ (°2 Theta 35.55)	MgO (°2 Theta 43.07)	BET Surface Area $m^2.g^{-1}$	Pore Volume $cm^3.g^{-1}$	Average Pore Size nm	V	Fe	Mg	O	P	M_S $emu.g^{-1}$	M_R $emu.g^{-1}$	H_C kOe	
Before P adsorption	S	33	38	29	34	51	2.42	0.116	19.2	-	14.5	29.2	56.3	-	20	6	0.24	11.3
	V	23	29	48	30	57	3.06	0.076	9.9	1.5	11.3	30	57.2	-	11	3	0.19	10.7
After P adsorption	S	54	42	4	29	41	5.80	0.218	15.1	-	12.7	27.2	58.3	1.7	25	8	0.22	-
	V	55	45	-	29	59	6.12	0.217	14.2	1.4	11.5	27	56.9	3	15	5	0.2	-

Table 12 – Hyperfine parameters obtained from the fits of 19 and 300 K ^{57}Fe Mössbauer spectra of the V and S-sample before (as-prepared) and after its interaction with the effluent rich in P, and after its alkaline regeneration. δ is the isomer shift given relative to α-Fe at 300 K, Q_{UA} is the quadrupolar shifting, B_{hf} is the magnetic hyperfine field, and the fraction of each component is represented by the area in percentage.

		1^{st}-component (B sites)				**2^{nd}-component (A sites)**				**3^{rd}-component**		
Sample	**T (K)**	**B_{hf} (mm/s)**	**Q_{UA} (mm/s)**	**δ (mm/s)**	**A (%)**	**B_{hf} (mm/s)**	**Q_{UA} (mm/s)**	**δ (mm/s)**	**A (%)**	**Q_{UA} (mm/s)**	**δ (mm/s)**	**A (%)**
S	19	52.9(5)	0.02(8)	0.42(5)	40(1)	50.9(5)	-0.06(8)	0.33(5)	57(1)	---	---	--
S+P		52.3(5)	0.05(2)	0.47(2)	46(1)	51.4(5)	-0.12(2)	0.27(1)	52(1)	---	---	--
Regenerated S		52.8(5)	0.02(1)	0.42(8)	49(1)	50.9(5)	-0.07(2)	0.32(1)	48(1)	0.00(1)	0.22(1)	3(1)
V	19	51.7(5)	0.12(2)	0.47(1)	44(1)	50.8(5)	-0.16(1)	0.28(4)	53(1)	0.60(1)	0.42(1)	3(1)
V+P		51.3(5)	-0.07(2)	0.49(1)	46(1)	50.7(5)	-0.13(1)	0.23(4)	51(1)	0.60(1)	0.42(1)	3(1)
Regenerated V		51.6(2)	0.11(1)	0.49(1)	47(1)	50.8(5)	-0.16(1)	0.25(5)	50(1)	0.70(1)	0.50(2)	4(1)
S	300	37.8(5)	-0.01(3)	0.28(1)	100	---	---	---	---	---	---	---
S+P		37.0(5)	-0.03(1)	0.29(1)	100	---	---	---	---	---	---	---
Regenerated S		39.4(5)	-0.02(1)	0.27(1)	100	---	---	---	---	---	---	---
V	300	30.5(5)	0.04(3)	0.21(1)	75	---				0.72(2)	0.39(2)	25
V+P		31.1(5)	0.03(2)	0.33(1)	75	---				0.63(2)	0.33(2)	25
Regenerated V		27.1(5)	0	0.30(1)	73	---				0.68(3)	0.34(2)	27

The importance of hydroxyl groups on phosphate adsorption efficiency is already well-established in the literature (IVANETS, Andrei et al., 2021). From FTIR spectra, the band in V-sample referred to OH^- stretching (2500-4000 cm^{-1}) is more intense than S-sample, which could reflect in higher adsorption efficiency in the former. The ligand exchange process can be facilitated due to the protonation of surface OH groups at low pH solutions (BALIARSINGH; PARIDA; PRADHAN, 2013; RAZANAJATOVO et al., 2021).

The average pore size for the MgFeO and V-MgFeO samples are in mesopore region (**Table 11**), and BET isotherms show hysteresis loops related to the connection of various sized pores (**Figure 20**). Thus, the isotherms for these adsorbents are classified as type-IV (THOMMES et al., 2015). In particular, the as-prepared S-(V-)sample has increased its surface area from 2.42(3.06) to 5.80(6.12) $m^2.g^{-1}$ after P adsorption. While there is enlargement of pores after P adsorption for the V-sample, the average pore size for the S-sample has diminished, showing the strong effect that the phosphates and V-substitution do on Mg-based phase. Ribeiro and coworkers (2023) have also observed the enlargement of its adsorbent surface area after P adsorption experiments. They have explained that the partial dissolution of adsorbent followed by its reprecipitation may have provoked this effect.

Figure 20(g, h) depicts magnetic hysteresis [M(H)] loops recorded at 300 K for the S- and V-samples before (S and V) and after P adsorption (SA and VA), and after alkaline regeneration (SR and VR) and the main magnetic parameters are also displayed in **Table 11**. Comparing the saturation magnetization (M_S) of the S and V-samples, it can be noticed that M_S value diminished after V addition, suggesting that V atoms are being incorporating in the atomic lattice of the cubic spinel structure, as also supported by ^{57}Fe Mössbauer spectrometry that will be discussed below. The narrow hysteresis loops (i.e., with low H_C field value) suggest a soft ferromagnetic character for the S and V-samples (SALIH; MAHMOOD, 2023). The gradual increasing of M_S values over P adsorption cycles indicates leaching of Mg^{2+} from MgO, in close agreement with the XRD data that indicate an augment on the $MgFe_2O_4$ fraction after P adsorption, consequently yielding an increase of the sample magnetic masses.

For the study of the morphology, size distribution, crystalline structure and atomic composition of the nano-adsorbents, TEM, HRTEM, STEM and EDS were systematically applied. Several TEM and STEM images were taken, at various magnifications, to have an overview of the nano-adsorbents. **Figure 21(a)** and **(c)** displays representative TEM images of the S- and V-samples, respectively. Statistical analyzes of the particle size distribution (PSD) are shown in inset figures. The PSD curves were calculated from the histograms after counting 300 nanoparticles. The distribution curves are asymmetric and well-fitted with log-normal functions. The mean size (<D>) was found to be 23 nm and 27 nm for the S- and V-samples, respectively, values that agree with those obtained from the X-ray for the spinel structure of the $MgFe_2O_4$. The figures inserted at the top show a zoom of the region of the box demarcated with dashed lines. The HRTEM figures clearly display interplanar distance of 0.3 nm, which corresponds to the (220) plane of $MgFe_2O_4$. The SAED patterns are shown in **Figure 21(b)** and **(d)** of the S- and V-samples, respectively. The SAED patterns contain dots where apparently the spots form discontinuous rings. This effect is due to the fact that each nanoparticle exhibits an almost monocrystalline behavior with different zone axes. The integrated angular intensity of the diffraction patterns for both samples shows peaks with similar interplanar. The vertical lines are the positions of X-ray reflections from the $MgFe_2O_4$ (ICSD 009939), and MgO (ICSD 064930) overlaps at 0.15 nm and 0.21 nm.

Figure 21 – (a) and (c) TEM images showing the S- and V-samples, respectively. The inset figures (at the bottom) show the particle size distribution with the corresponding lognormal fit. The inset figures (at the top) display the zoom of the region selected by the box of dashed lines, showing the interplanar distances. (b) and (d) typical electron diffraction patterns for the S- and V- samples, respectively. The inset figures show the integrated angular intensity of the diffraction pattern. The vertical lines are the positions of X-ray reflections from $MgFe_2O_4$ (ICSD 00-9939) and MgO (ICSD 064930).

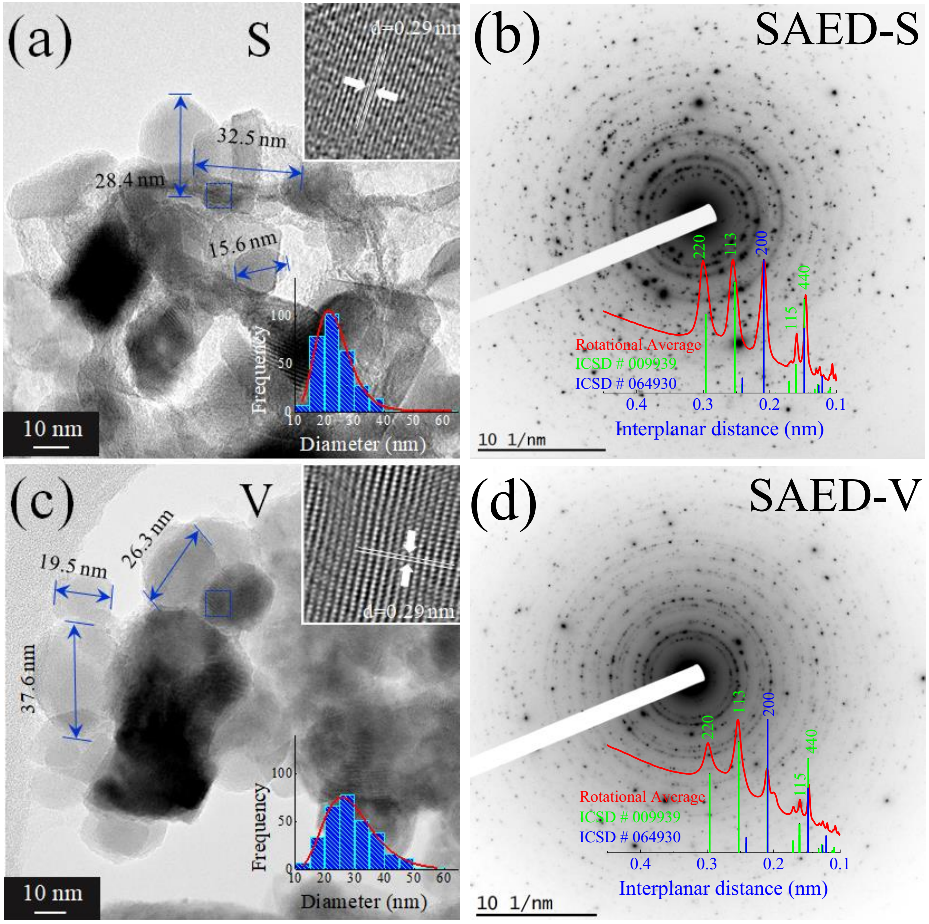

To confirm the elemental distributions of the nano-adsorbents, **Figure 22** shows the atomic-scale EDS-STEM mappings of the V, VA and VR samples, where Mg, Fe, O and V atoms are clearly visible in all samples. For the VA sample, however, irregular structures formed by Mg and P are observed, an effect similar to that found for the struvite crystals formed by P precipitation (KOFINA; KOUTSOUKOS, 2005).

Figure 22 – STEM-EDS mapping analysis of the V-, VA- and VR-samples with their respective elemental maps of Mg (yellow), Fe (blue), O (cyan), V (red) and P (magenta), respectively.

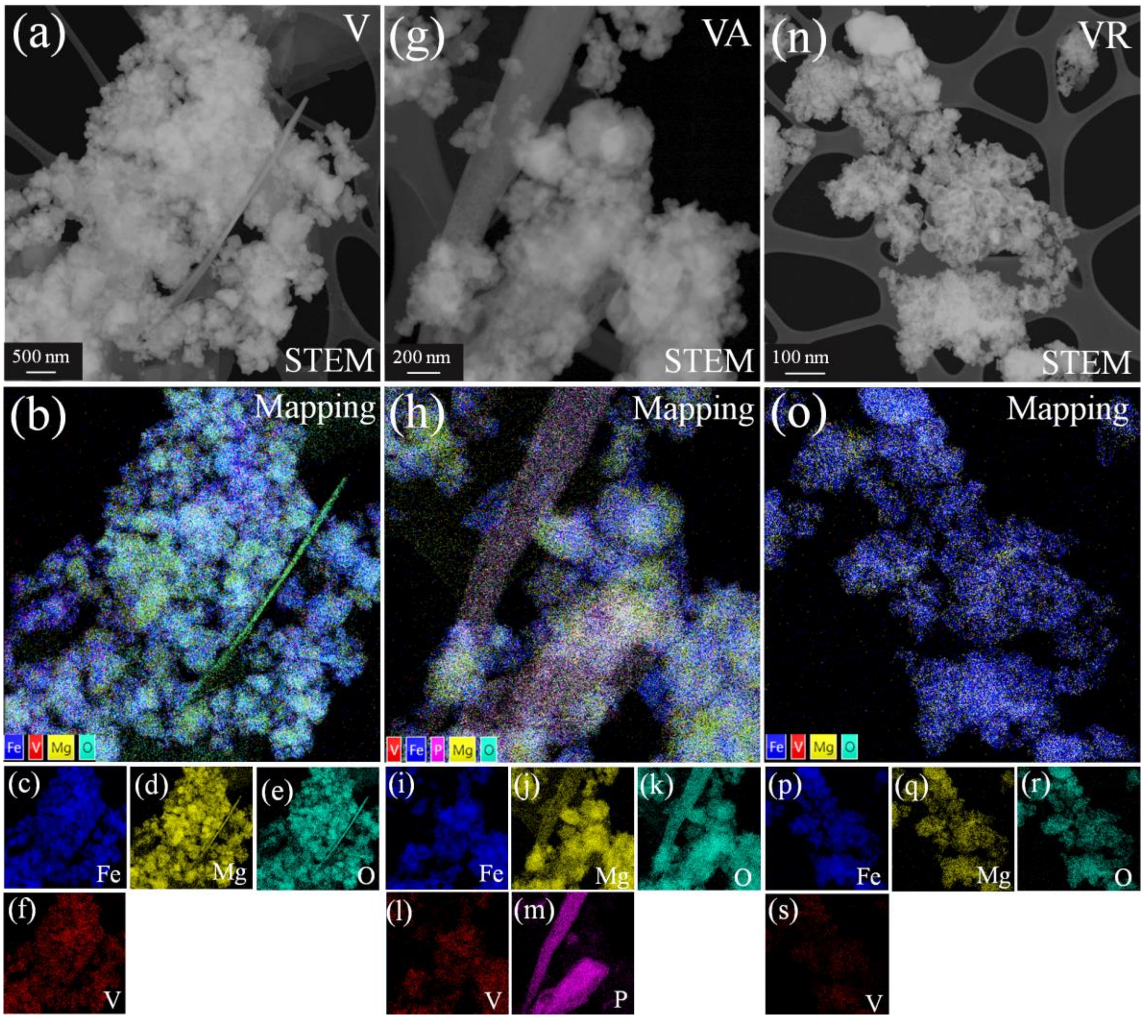

From MEV-EDS of the V-sample (**Figure 25(c)** and **(d)**), the molar ratio Mg/Fe before P adsorption was found to be 2.7 and slightly dropped to 2.3 after P adsorption, while V/Fe molar ratio was maintained at 0.13 after P adsorption (**Table 11**). These observations suggest that (i) there is a Mg^{2+} releases on the effluent probably from the MgO matrix, ions that may react with P and precipitate, and (ii) the V ions are bounded to Fe ions on the $MgFe_2O_4$ ferrite surface, consequently with no significant V leaching after adsorption experiments (this assumption will be supported by ^{57}Fe Mössbauer data).

Figure 23 – SEM images and EDS mapping of the V-MgFeO sample (a, c) before and (b, d) after P adsorption.

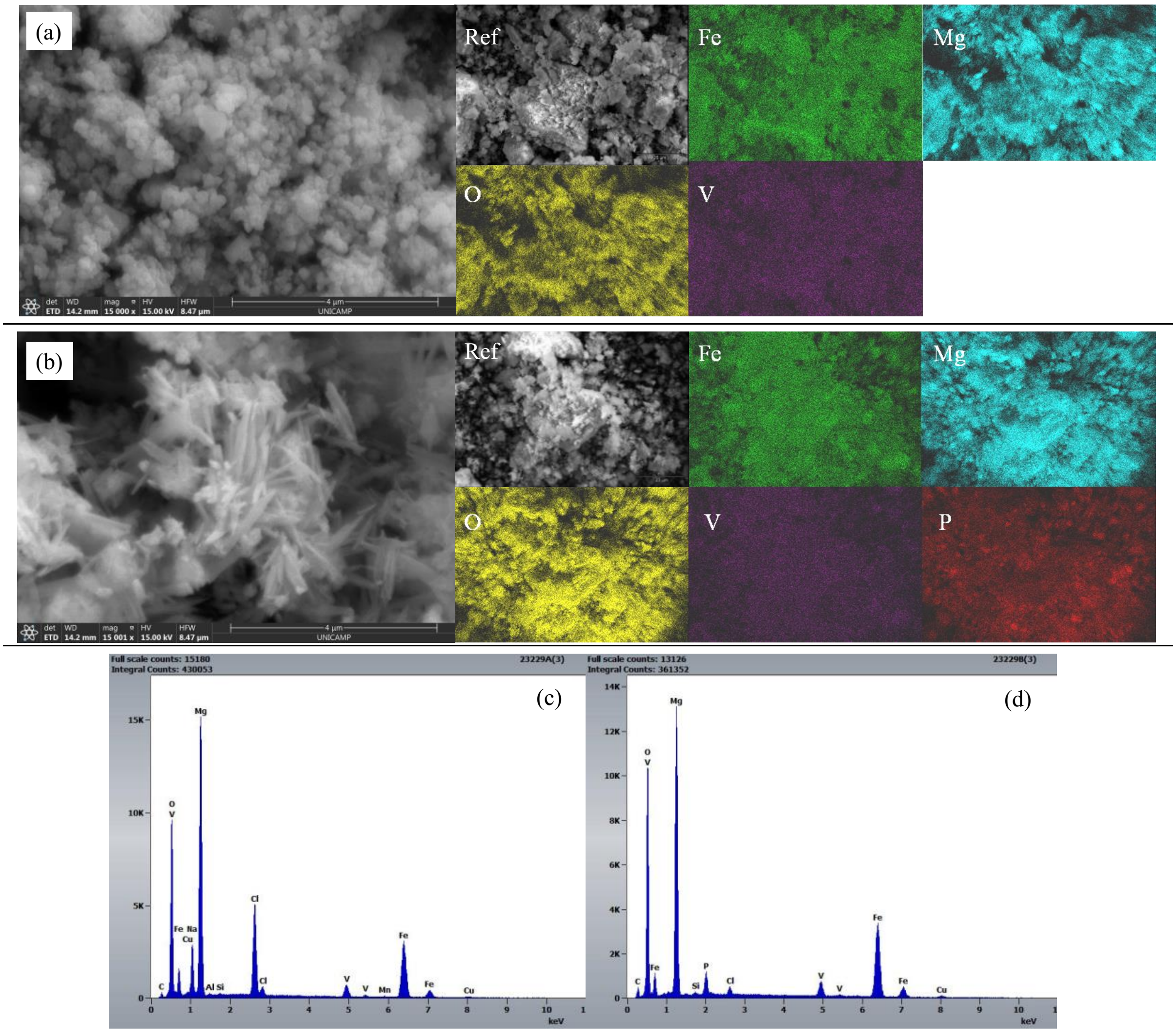

^{57}Fe Mössbauer spectra taken at 300 K (**Figure 24** top panel) and 19 K (bottom panel) before and after P adsorption, and after adsorbent regeneration for the S and V-samples were fitted considering the following components for data taken at 19 K:

- Two sextets for Fe^{3+} ions in cubic spinel structure [tetrahedral - A (green) and octahedral - B (blue)] that results from the Zeeman interaction of ^{57}Fe nuclear magnetic moment with the B_{hf} field (KURIAN; MATHEW, 2018; RAGHASUDHA et al., 2017). At 300 K, the sextets are broader due to thermal effects and the spectra are fitted with a distribution component. However, the spectra of the same samples are at 19 K because of reduction of spin fluctuation. They were then fitted with the two resolved subspectra due to the A and B sites of the spinel structure;

- One doublet (orange) observed in small fraction for V-substituted ferrite at 19 K, but with a large fraction at RT. After regeneration, a very small doublet also appears in the V-non-substituted sample. The presence of doublet suggests in V-substituted sample a paramagnetic phase for part of Fe ions (HUMBE et al., 2020). It can be explained by low ordering temperature due to an Fe-poor phase in Mg-ferrite or can be attributed a size effect of Mg-ferrite crystals caused by V^{3+} substitution that leads a grain reduction that favors a SPM regime (ALMESSIERE et al., 2022; KURIAN; MATHEW, 2018; RAGHASUDHA et al., 2017).

Sextets are assigned to A and B sites according to isomer shift (δ) values, which is a sign of s- electron density. Larger δ is referred to octahedral sites, since metal oxygen bond length is higher and the overlap of orbitals in B site is smaller (ALMESSIERE et al., 2022; HASHIM et al., 2013; JUSTIN JOSEYPHUS et al., 2006; KURIAN; MATHEW, 2018; RAGHASUDHA et al., 2017). It is commonly reported that for δ in the range of 0.1-0.5 $mm.s^{-1}$ Fe ions are in trivalent state (i.e.,Fe^{3+}), while δ for Fe^{2+} lies in the range of 0.6-1.7 $mm.s^{-1}$ (HE et al., 2015; KUMAR, Shalendra et al., 2008). Thus, the values of δ for samples in **Table 12** indicates a trivalent state for Fe ions and they are randomly occupying A and B sites, if one looks to their fractions (for an inverse spinel the fraction of A site occupied by Fe^{3+} should be 50 %) (HUMBE et al., 2020; KAUR UBHI et al., 2022). Therefore, the Mg-ferrite possesses a mixed-spinel structure. In fact, it has been reported that Mg^{2+} have preference for octahedral interstitial sites (REYES-RODRÍGUEZ et al., 2020). However, calcinating temperature plays an important role on Mg-ferrite degree of inversion (ŠEPELÁK et al., 2001).

The rise of 3rd components (assigned to a paramagnetic doublet) in V-substituted MgFeO is correlated to its weaker ferrimagnetism (low magnetization) compared to non-doped adsorbent (SATYANARAYANA et al., 2019). This assumption is also supported by the fact that after V-substitution there is a decrease of magnetic hyperfine field (B_{hf}) assigned to B site, which indicates that V has preference to B site (HASHIM et al., 2013; YADAV et al., 2015).

Figure 24 – ^{57}Fe Mössbauer spectroscopy at i) 300 K and ii) 19 K before (top) and after (middle) P adsorption, and after adsorbent regeneration (bottom) for: MgFeO (left-hand side) and V-MgFeO (right-hand side). Legend: V and SC are V-MgFeO and MgFeO, respectively; VA and SA are V and S after P adsorption; VR and SR are V and S after adsorbent alkaline regeneration.

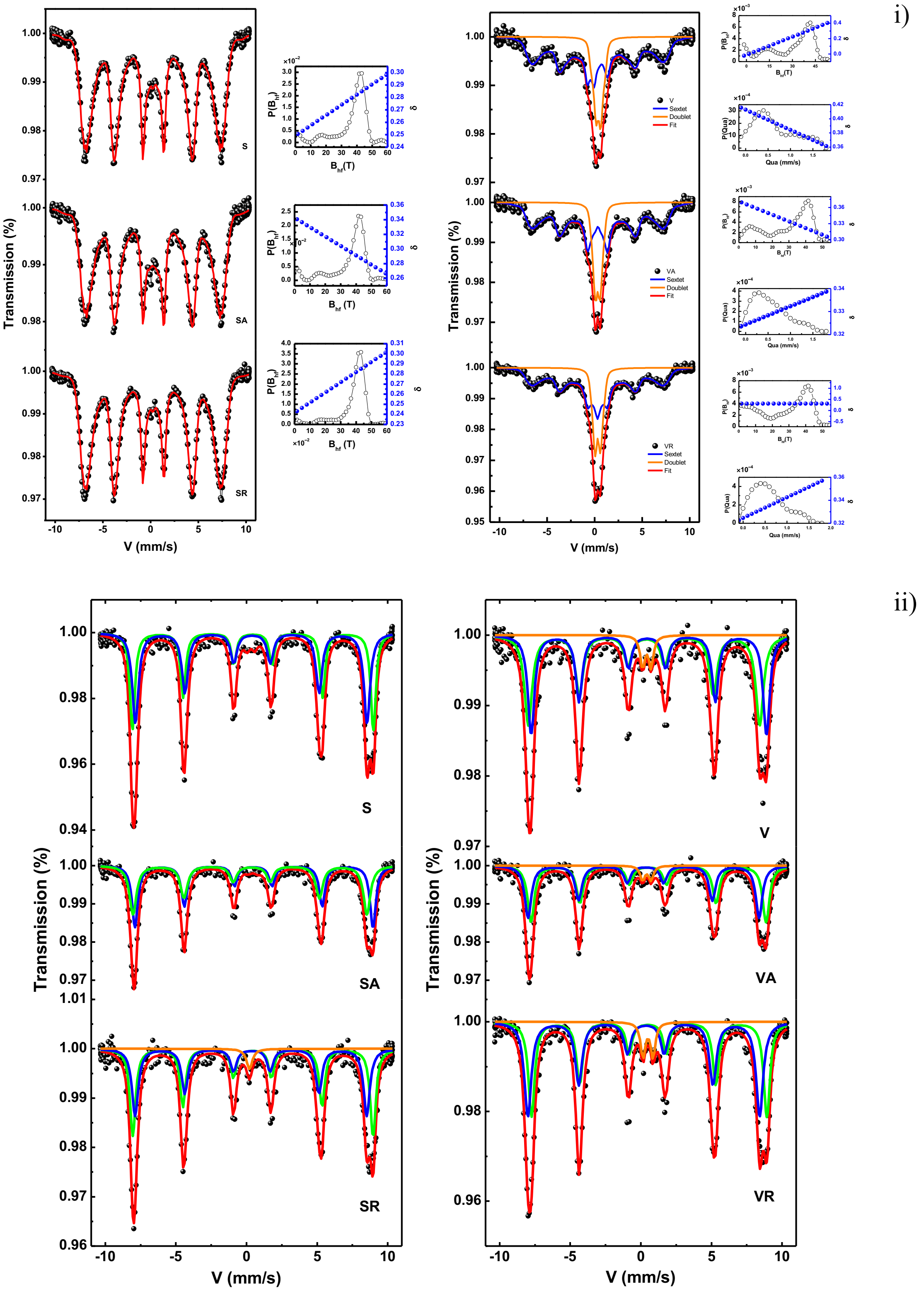

4.2.2 Adsorbent dosage

For adsorbent dosage higher than 1.75 $g.L^{-1}$, both materials remove over 80 % of phosphorous and have similar adsorption capacities (**Figure 25**(a)). Greater specific surface area allied to a higher amount of hydroxyl groups would favor enhanced adsorption capacity for V-MgFeO at low adsorbent dosage in face to MgFeO results. Adsorption capacity tends to reduce with increasing adsorption dosage since it starts to have an excess of active sites. An adsorbent dosage of 2 $g.L^{-1}$ is employed for the next experiments since it is the minimum dosage capable of removing 90 % phosphate.

4.2.3 Adsorption kinetic

Figure 25(b) presents the adsorption kinetic data obtained from batch experiments, modeled by PFO and PSO. After a 24-hour contact time, both materials achieve impressive P removal rates of over 90 %. However, the V-sample exhibits a remarkable 70% removal, accomplishing this in approximately 2.5 h less than the S-sample. The fitting of the adsorption data is notably superior for the PSO model, with an R^2 exceeding 0.995 (**Table 13**).

Thus, the intraparticle diffusion model was used to investigate the adsorption mechanism by plotting q_t vs $t^{0.5}$. The intraparticle diffusion model was tested (**Figure 25(c)**), and two stages were observed, with diffusion rate constants $k_{s1} > k_{s2}$. The first stage is faster and can be assigned to outer-surface phosphate adsorption. In contrast, the second stage can be related to the intraparticle diffusion process plus a lower concentration of phosphate, which reduces the probability of the contaminant hitting an active site (BENHITI et al., 2021).

4.2.4 Adsorption isotherm

The effect of initial phosphate was investigated, and the results are shown in **Figure 25**(d). The Freundlich isotherm model fitted better for both adsorbents, indicating that the adsorption site distribution is heterogeneous and there is a multilayer adsorption process (**Table 14**). Besides that, the adsorption process is favorable since 1/n values are between 0 and 1 (AL-GHOUTI; DA'ANA, 2020).

Figure 25 – Results of P adsorption experiments for the S- and V-samples (a) with different adsorbent dosage; (b) fits with PFO and PSO models for P adsorption kinetic; (c) fits with intraparticle diffusion model for adsorption kinetic; (d) P adsorption isotherm; (e) pH influence (inset of P species speciation); and (f) coexisting species.

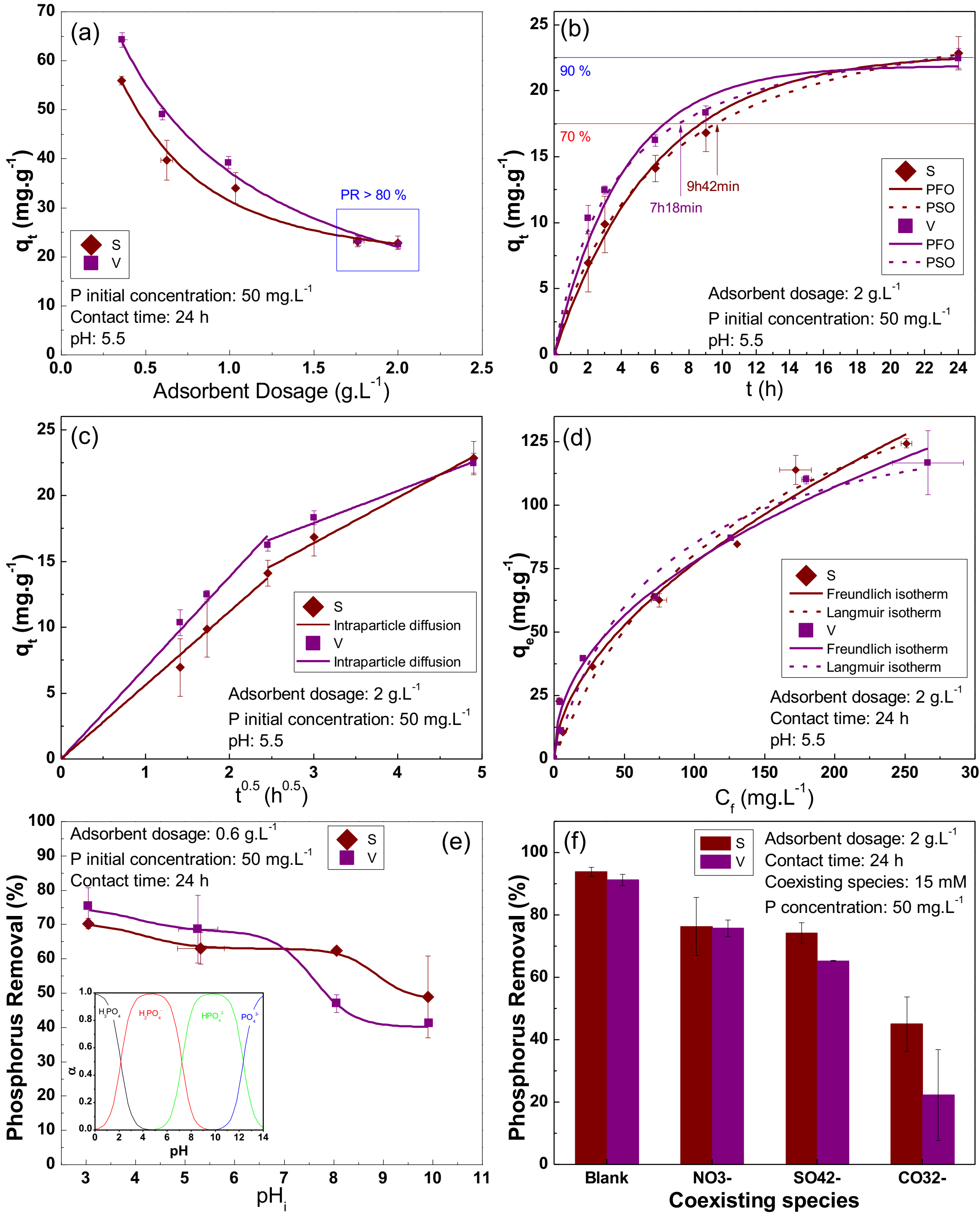

Table 13 – Parameters obtained from fitting the experimental data with different adsorption kinetic models.

Model	Equation	Parameter	MgFeO	V-MgFeO
		q_e (exp)	(22 ± 1)	(22.5 ± 0.8)
Pseudo 1nd order	$q_t = q_e(1 - e^{-K_1 t})$	K_1	(0.17 ± 0.1)	(0.24 ± 0.04)
		q_e	(22.8 ± 0.8)	(21 ± 1)
		R^2	0.9916	0.9731
Pseudo 2nd order	$q_t = \frac{K_2\, q_e^2\, t}{1 + K_2\, q_e\, t}$	$K_2 q_e$	(0.167 ± 0.007)	(0.28 ± 0.02)
		$K_2 q_e^2$	(4.7 ± 0.1)	(7.3 ± 0.4)
		q_e	28.14	26.07
		K_2	0.006	0.011
		R^2	0.999	0.9961
Weber and Morris (Stage I)	$q_t = k_{s1}\, t^{0.5}$	k_{s1}	(5.6 ± 0.2)	(6.9 ± 2)
		R^2	0.9957	0.9973
Weber and Morris (Stage 2)	$q_t = k_{s2}\, t^{0.5} + I$	k_{s2}	(3.5 ± 0.3)	(2.4 ± 0.3)
		I	(6 ± 1)	(11 ± 1)
		R^2	0.9826	0.9718

Table 14 – Parameters obtained from fitting the experimental data with Freundlich adsorption isotherm model.

Model	Equation	Parameter	MgFeO	V-MgFeO
Freundlich	$q_e = k_f\, C_e^{\frac{1}{n}}$	k_f	(6 ± 2)	(9 ± 2)
		n	(1.8 ± 0.2)	(2.2 ± 0.2)
		R^2	0.9779	0.9835
Langmuir	$q_e = \frac{q_{max}\, bC_e}{1 + bC_e}$	b	(0.007 ± 3)	(0.014 ± 5)
		q_{max}	(194 ± 37)	(146 ± 17)
		R^2	0.9619	0.9657

4.2.5 pH influence

During the experiments, pH remained between 3 and 10 (**Figure 25(e)**), meaning phosphate species were negatively charged (see **Figure 25(e) inset**). At the same time, the pH of zero charge for adsorbent was around 10 (**Figure 26**), so for all the experiments, the adsorbent surface was positively charged ($pH<pH_{PZC}$), which attracted negatively-charged phosphates (LIU et al., 2018; RAZANAJATOVO et al., 2021).

It can be noted that V-sample has an advantage on P adsorption at low pH, but at high pH the S-sample surpasses. Even though the high presence of superficial hydroxyl groups at V-sample can facilitate the ligand exchange process at a low pH solution, OH^- can compete with phosphate for active sites at high pH, leading to decrease P adsorption efficiency (BALIARSINGH; PARIDA; PRADHAN, 2013; RAZANAJATOVO et al., 2021).

Also, the fact that the pH of solution was higher after P adsorption implies that hydroxyl groups from the adsorbent surface were released into the solution, corroborating to ion-exchange mechanism (LONG et al., 2011; RAZANAJATOVO et al., 2021; ZHANG et al., 2018).

Figure 26 – pH of zero charge for adsorbents.

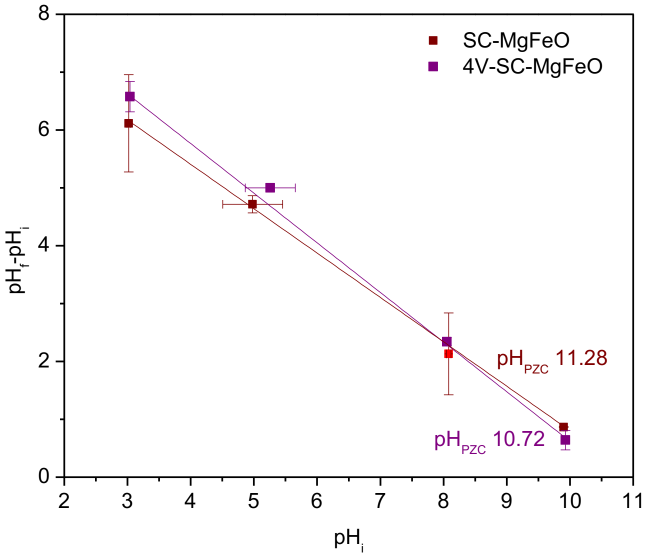

4.2.6 Coexisting ions

Industrial effluents and sewage always contain other anions (Cl^-, NO_3^-, SO_4^{2-} and CO_3^{2-}) that may compete with phosphate for active sites. **Figure 25(f)** shows the interference of coexisting species. Thus, the order of influence on P adsorption was found to be $CO_3^{2-} > SO_4^{2-} > NO_3^-$. This result agrees with Lewis acid-base theory, which posits that the alkalinity of anions follows the order $PO_3^{4-} > CO_2^{3-} > SO_2^{4-} > Cl^- > NO_3^-$. Consequently, coexisting ions will strongly compete with phosphate for active sites if those have a similar capability to donate electrons as phosphate (GUO et al., 2023). Moreover, it can be noted that the S-sample has lower inhibition than the V-sample for SO_4^{2-} and CO_3^{2-}. Indeed, it is expected that the addition of Na_2CO_3 would raise the pH of the solution due to its hydrolysis (GUO et al., 2023) and, as discussed before, the V-sample is associated with impaired ligand exchange at high pH.

4.2.7 Adsorption study with sewage treatment plant effluent

Municipal sewage treated effluent was used for 3 consecutive adsorption cycles, since it was noticed through the preliminary tests that after third adsorption cycle the results are not reproducible anymore, which could indicate adsorbent saturation. Therefore, the desorption experiment was performed after all (**Figure 27**). Based on experiments performed with synthetic wastewater, it is expected that for 2 $g.L^{-1}$ of adsorbent and 50 $mg.L^{-1}$ of phosphate the removal efficiency for both materials would reach 90 %. However, a phosphate uptake for the first cycle with real effluent was around 60 %. At least, the two main possible reasons for these results are: (i) P concentration in effluent was around (11 ± 1) $mg.L^{-1}$, which reduces the probability of P species hit an active site and (ii) the presence of other species in the effluent that compete for active sites. Moreover, the subsequent two cycles, after the first one, indicate a gradual increase of the P removal efficient (no treatment was done in the samples in the multicycle adsorption tests).

It is also noticed that the V-sample has a slightly advantaged on P adsorption compared to the S-sample. However, a very high P desorption was observed for the V-sample (97 %) against S-sample after the alkaline treatment of the P-adsorbed samples. This suggests that with stabilization of residual NaOH in adsorbent surface and pores plus further regeneration with $MgCl_2$ solution it could recover the ability of adsorbents to remove phosphate and can also change the V-sample efficacy for P removal in real contaminated water. The full regeneration of Mg-ferrite, using 0.001-0.1 M $MgCl_2$ regenerative solutions, was consistently proved by Ivanets and coworkers (IVANETS, A. I. et al., 2019; IVANETS, A.I. et al., 2018; IVANETS, Andrei et al., 2021). It must be emphasized that our nanoadsorbents were able to maintain their efficiencies for three cycles even with no chemical regeneration, a good result and rarely found in the literature.

4.2.8 Adsorption mechanism

Based on the information obtained up to now, it can be proposed the following P adsorption mechanism (**Figure 28**).

I) XRD and magnetization data indicated a reduction of MgO phase due to Mg^{2+} ions release, while SEM-EDS and TEM mapping have shown a lower Mg/Fe molar ratio after P adsorption and the formation of irregular flake-like structures composed by Mg and P, similar to struvite crystallization and precipitation. However, the Mössbauer and SEM-EDS revealed that V is stable in octahedral sites of Mg-ferrite;

Figure 27 – Batch reuse and regeneration of adsorbent with real effluent.

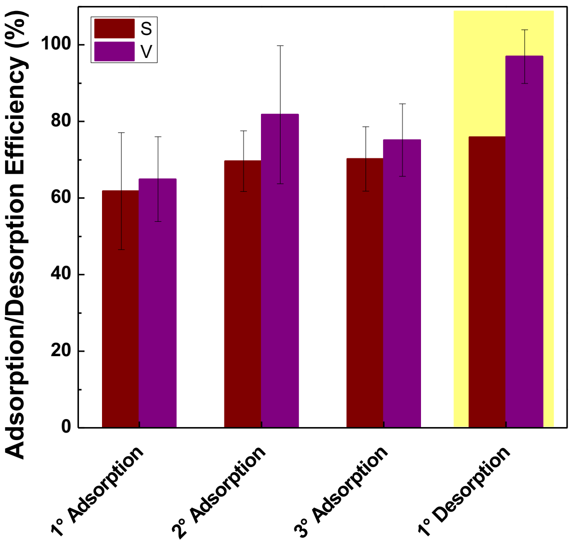

Figure 28 – Scheme of the P adsorption mechanism for the S- and V-nanocomposites.

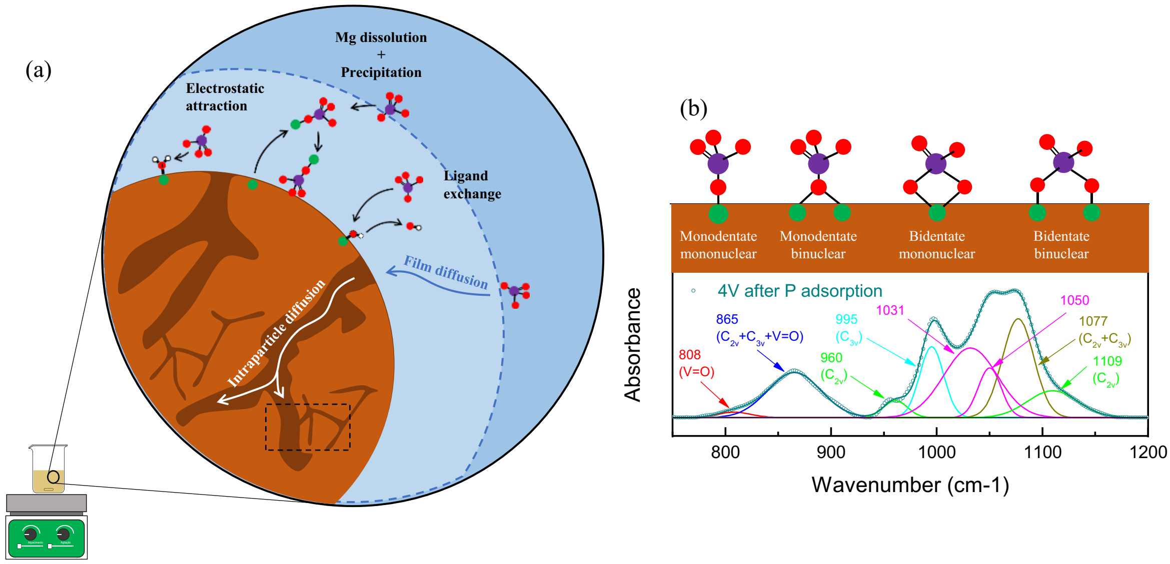

II) At low pH (7 > pH > 3), there is a high P removal efficiency due to phosphate-adsorbent electrostatic attraction on the MgO surface. Also, ligand exchange plays an important role since there is a significant loss of adsorption efficiency at pH > 7 due to hydroxyl groups competing with phosphate for active sites;

III) At the beginning of P adsorption, there is fast adsorption on the external surface of the adsorbent. Phosphate uptake reduces when the outer surface saturates, and the intraparticle diffusion process overcomes. Also, a lower phosphate concentration minimizes the probability of phosphate reaching an active site;

IV) As suggested by Freundlich model, the P adsorption is heterogeneous and a multilayer character dominates the adsorption;

V) Deconvolution of FTIR spectra after P adsorption suggests phosphate binding to adsorbent as a monodentate or bidentate ligand.

4.2.9 Cost evaluation

The estimated costs for adsorbents synthesis, effluent treatment, P adsorption and desorption are shown in **Table 15**. Considering the synthesis process, chemical reagents correspond to the main portion of cost. Both materials have the same energy cost, but the use of NH_4VO_3 for the substitution effect in the S-sample compound has increased the preparation cost from 76.99 USD kg^{-1} to 88.68 USD kg^{-1}. The cost for effluent treatment is estimated for a real effluent with an average P concentration of (11 ± 1) mg L^{-1} treated at adsorbent dosage of 2 g L^{-1} and contact time of 24 h. The adsorbents were used for 3 consecutive cycles without regeneration. For 1 kg of each adsorbent, 1500 L of effluent can be treated. However, the V-sample has shown greater adsorption capacity, which led to a cost reduction on P adsorption of 11 % compared to the S-sample. As discussed before, the addition of V on the adsorbent enhanced its desorption capability in 30%, and the cost for P desorption reduced from 10.27 USD g-P^{-1} to 6.2 USD g-P^{-1}. Therefore, although the addition of V to the adsorbent has increased its synthesis cost, greater adsorption and desorption efficiencies were reached leading to lower costs of effluent treatment.

Table 15 – Cost evaluation of adsorbents synthesis and P recovery.

<table>
<tr><th colspan="4">Reagents</th></tr>
<tr><td>Material</td><td>Relative cost (USD.kg^{-1})</td><td>Real cost to produce 1 kg of S-sample (USD)</td><td>Real cost to produce 1 kg of V-sample (USD)</td></tr>
<tr><td>$FeCl_3.6H_2O$</td><td>27.06</td><td>32.82</td><td>31.81</td></tr>
<tr><td>$MgCl_2.6H_2O$</td><td>10.51</td><td>33.91</td><td>32.86</td></tr>
<tr><td>NH_4VO_3</td><td>194.88</td><td>0.00</td><td>14.02</td></tr>
<tr><td>NaOH</td><td>6.98</td><td>8.87</td><td>8.59</td></tr>
<tr><th colspan="4">Energy</th></tr>
<tr><td></td><td>Heating/Mixing</td><td>Vaccum filtration</td><td>Calcination (precursor)</td></tr>
<tr><td>Time (h)</td><td>1</td><td>2</td><td>2</td></tr>
<tr><td>Power expenditure (kW)</td><td>1.5</td><td>2.92</td><td>7.44</td></tr>
<tr><td>Energy Cost (USD)</td><td>0.18</td><td>0.35</td><td>0.88</td></tr>
<tr><th colspan="4">Total cost of synthesis per kg</th></tr>
<tr><td colspan="2">S-sample (USD.kg^{-1})</td><td colspan="2">V-sample (USD.kg^{-1})</td></tr>
<tr><td colspan="2">76.99</td><td colspan="2">88.68</td></tr>
<tr><th colspan="4">Cost of P recovery</th></tr>
<tr><td colspan="2"></td><td>S-sample</td><td>V-sample</td></tr>
<tr><td colspan="2">Adsorption capacity (g of P/kg of adsorbent)</td><td>8.99</td><td>11.65</td></tr>
<tr><td colspan="2">Cost per g of P adsorbed (USD.g^{-1})</td><td>8.56</td><td>7.61</td></tr>
<tr><td colspan="2">Volume of effluent treated (L)</td><td>1500</td><td>1500</td></tr>
<tr><td colspan="2">Cost per liter of effluent treated (USD.L^{-1})</td><td>0.051</td><td>0.059</td></tr>
<tr><td colspan="2">Desorption capacity (g of P/kg of adsorbent)</td><td>6.83</td><td>11.31</td></tr>
<tr><td colspan="2">Cost per g of P desorbed (USD.g^{-1})[1]</td><td>10.27</td><td>6.20</td></tr>
</table>

[1] For 1 kg of adsorbent it is necessary 250 L of 1 N NaOH (or 10 kg of NaOH) and 2 h for adsorbent drying, which costs USD 70.16.

[2] At a value of 0.118 USD.kW^{-1} as given by the local energy company.

4.3 CONCLUSION

A novel Vanadium-modified Mg-Fe based composite was synthesized via co-precipitation method. Samples were characterized by XRD, FTIR, BET and BJH, and SEM-EDS. To understand P species interactions with adsorbents, adsorption kinetics, isotherm, adsorbent dosage, pH and coexisting ions dependence, and adsorption/desorption cycles were systematically performed. Both materials fitted better to the Freundlich isotherm model, indicating that the adsorption site distribution is heterogeneous and a multilayer adsorption mechanism is favored. Adsorption kinetics has shown two controlling steps: (i) outer-surface phosphate adsorption; and (ii) intra-particle diffusion. However, V-functionalized adsorbent obtained higher adsorption rates in the first step, which could be related to its higher specific surface area. At alkaline environment, both materials performed worse, possibly due to hydroxyl competition to active sites. The presence of competing ions has impacted P adsorption efficiency. Mg-Fe composites were also used for real effluent from sewage treatment plant and even though V-modified adsorbent has higher synthesis cost, its better adsorption and desorption efficiency have diminished treatment and P recovery cost. In short, the use of co-precipitation method has simplified Mg-Fe method and reduced synthesis cost. Also, modifying adsorbent with V has improved its adsorption and desorption capacity with real effluent. These characteristics make this novel composite more competitive for P adsorption processes.

5 OVERALL CONCLUSIONS

This project evaluated the synthesis of Mg-Fe composites synthesized via Sol-gel and co-precipitation method, and then tested their feasibility for P adsorption. First, it was checked the effect of calcination temperature and Mg content in composite matrix using sol-gel method. The material with the highest Mg/Fe ratio and calcinated at 700 °C achieved an adsorption capacity of 60 $mg.g^{-1}$. Second, it was used co-precipitation method to simplify and reduce costs of adsorbent synthesis and produce Mg-Fe composite functionalized with Vanadium. It was also noticed that the materials synthesized by Sol-gel method followed the Langmuir isotherm model, while the data obtained from samples prepared with co-precipitation method adjusted to the Freundlich model. pH and coexisting groups strongly affect adsorption efficiency, since hydroxyl groups (in alkaline environment) and other groups compete to active sites. Higher adsorption and desorption efficiency led to diminishing treatment cost by V-modified adsorbent, which makes this material the most efficient in this work. Even though SG seems a reliable method, several reasons could be pointed out to use co-precipitation instead: (i) the co-precipitation method is less expensive than SG and with higher reproduction in sample properties, (ii) the sample preparation by co-precipitation leads to nanocrystalline materials, where Mg-ferrite and MgO phases range in nanometric scale (samples synthesized by SG process show crystalline grains reaching the micrometric regime), (iii) the co-precipitated samples show different structure, hyperfine, magnetic and adsorption properties when compared with the SG ones and, (iv) the co-precipitation synthesis demands less time than that by SG. **Table 16** illustrates that the final results obtained meet the specific objectives proposed at the beginning of the project.

Table 16 – Specific objectives proposed at the beginning of the project and the final results obtained.

Specific Objectives	Results
Investigate the influence of synthesis parameters (such as Mg/Fe molar ratio, calcination temperature and V-doping) on physical-chemical and textural characteristics of adsorbents and on the P adsorption efficiency;	Precursor calcinated at 973 K had better chemical stability and great adsorption efficiency. Increasing Mg/Fe molar ratio led to higher adsorption capability, which indicates that Mg has more affinity to P than Fe.
Study the effect of adsorbent dosage, initial P concentration, initial pH, and coexisting ions on the adsorption process;	Adsorption isotherms for adsorbents synthesized through sol-gel and reverse coprecipitation followed Langmuir and Freundlich isotherm, respectively. Higher pH tends to impact the adsorption efficiency, since hydroxyl groups compete with P for active sites. Other species (NO_3^-, SO_4^{2-} and CO_3^{2-}) also have significant effect on adsorption efficiency. Adsorbents can be reused over 3 cycles without chemical regeneration.
Understand the P adsorption mechanism;	Negatively charged phosphate reacts with the positively charged adsorbent surface by electrostatic interaction. Ligand exchange is an important path of P removal. Mg leaches from adsorbent surface, reacts with P, and forms crystals.
Evaluate the economic viability of using adsorbents in P recovery.	Using reverse coprecipitation method reduced the cost of adsorbents synthesis and time expenditure compared to sol-gel. Adding V to the adsorbent matrix improved adsorption and desorption efficiency of P.

6 PROSPECTS FOR FUTURE WORKS

Great improvements were obtained through this project aiming the synthesis of an efficient and low cost Mg/Fe-based composite for the removal of phosphate from wastewater. This thesis still leaves open doors for more research, as follows:

- Increase Mg/Fe molar ratio to balance treatment cost and magnetic properties;
- V-modified materials possesses photocatalytic properties under visible light, therefore these photocatalysts could be employed for orgaphosphorous compounds degradation;
- Support V-modified composite on biochar;
- Perform pilot-scale adsorption column experiments.

REFERENCES

ABCON. Impactos econômicos da universalização do saneamento básico no Brasil. p. 24, 2022.

ABID, Namra et al. Synthesis of nanomaterials using various top-down and bottom-up approaches, influencing factors, advantages, and disadvantages: A review. **Advances in Colloid and Interface Science**, v. 300, p. 102597, fev. 2022. Disponível em: <https://linkinghub.elsevier.com/retrieve/pii/S0001868621002384>.

AL-GHOUTI, Mohammad A.; DA'ANA, Dana A. Guidelines for the use and interpretation of adsorption isotherm models: A review. **Journal of Hazardous Materials**, v. 393, p. 122383, jul. 2020. Disponível em: <https://linkinghub.elsevier.com/retrieve/pii/S030438942030371X>.

ALMANASSRA, Ismail W. et al. A state of the art review on phosphate removal from water by biochars. **Chemical Engineering Journal**, v. 409, p. 128211, abr. 2021. Disponível em: <https://linkinghub.elsevier.com/retrieve/pii/S1385894720343278>.

ALMESSIERE, Munirah A. et al. Bi3+ and V3+ co-substituted Ni-Co spinel ferrites: Synthesis, optical, magnetic characterization and hyperfine interaction. **Materials Science and Engineering: B**, v. 284, p. 115905, out. 2022. Disponível em: <https://linkinghub.elsevier.com/retrieve/pii/S092151072200294X>.

BAIRD B., Rogers; EATON D., Andrew; RICE W., Eugene. **Standard methods for the examination of water and wastewater**. 23rd editi ed. [S.l: s.n.], 2017. v. 49.

BALIARSINGH, N.; PARIDA, K. M.; PRADHAN, G. C. Influence of the nature and concentration of precursor metal ions in the brucite layer of LDHs for phosphate adsorption – a review. **RSC Advances**, v. 3, n. 46, p. 23865, 2013. Disponível em: <http://xlink.rsc.org/?DOI=c3ra42857e>.

BECKER, Anna; KIRCHBERG, Kristin; MARSCHALL, Roland. Magnesium Ferrite (MgFe 2 O 4) Nanoparticles for Photocatalytic Antibiotics Degradation. **Zeitschrift für Physikalische Chemie**, v. 234, n. 4, p. 645–654, 28 abr. 2020. Disponível em: <https://www.degruyter.com/document/doi/10.1515/zpch-2019-1430/html>.

BENHITI, Ridouan et al. RETRACTED ARTICLE: Kinetic, isotherm, thermodynamic and mechanism investigations of dihydrogen phosphate removal by MgAl-LDH. **Nanotechnology for Environmental Engineering**, v. 6, n. 1, p. 16, 17 maio 2021. Disponível em: <https://link.springer.com/10.1007/s41204-021-00110-7>.

BETTINELLI, M. et al. Photocatalytic activity of TiO2 doped with boron and vanadium. **Journal of Hazardous Materials**, v. 146, n. 3, p. 529–534, jul. 2007. Disponível em: <https://linkinghub.elsevier.com/retrieve/pii/S0304389407005389>.

BRASIL. Lei n° 14.026, de 15 de julho de 2020 Novo Marco Legal do Saneamento Básico. 2020.

BROCKMAN, F. G. Structure and properties of ferrites. **Electrical Engineering**, v. 70, n. 6, p. 489–494, jun. 1951. Disponível em: <http://ieeexplore.ieee.org/document/6436635/>.

BRUNAUER, Stephen; EMMETT, P. H.; TELLER, Edward. Adsorption of Gases in Multimolecular Layers. **Journal of the American Chemical Society**, v. 60, n. 2, p. 309–319, 1 fev. 1938. Disponível em: <https://pubs.acs.org/doi/abs/10.1021/ja01269a023>.

BUKHTIYAROVA, M.V. A review on effect of synthesis conditions on the formation of layered double hydroxides. **Journal of Solid State Chemistry**, v. 269, p. 494–506, jan. 2019. Disponível em: <https://linkinghub.elsevier.com/retrieve/pii/S0022459618304511>.

CHEN, Run-Feng et al. Effect of Organic Substances on Nutrients Recovery by Struvite Electrochemical Precipitation from Synthetic Anaerobically Treated Swine Wastewater. **Membranes**, v. 11, n. 8, p. 594, 4 ago. 2021. Disponível em: <https://www.mdpi.com/2077-0375/11/8/594>.

CHENG, Fulong et al. Efficient and stable removal of phosphate from aqueous solutions by hollow microspheres of MgO/ZrO2 composite oxide. **Colloids and Surfaces A: Physicochemical and Engineering Aspects**, v. 635, p. 128095, fev. 2022. Disponível em: <https://linkinghub.elsevier.com/retrieve/pii/S0927775721019646>.

CHRISPIM, Mariana Cardoso; SCHOLZ, Miklas; NOLASCO, Marcelo Antunes. Phosphorus recovery from municipal wastewater treatment: Critical review of challenges and opportunities for developing countries. **Journal of Environmental Management**, v. 248, p. 109268, out. 2019. Disponível em: <https://linkinghub.elsevier.com/retrieve/pii/S0301479719309703>.

CORDELL, Dana; DRANGERT, Jan-Olof; WHITE, Stuart. The story of phosphorus: Global food security and food for thought. **Global Environmental Change**, v. 19, n. 2, p. 292–305, maio 2009. Disponível em: <https://linkinghub.elsevier.com/retrieve/pii/S095937800800099X>.

CULLITY, B. D.; GRAHAM, C. D. **Introduction to magnetic materials**. [S.l: s.n.], 2009. v. 12. Disponível em: <http://linkinghub.elsevier.com/retrieve/pii/S1369702109700914>.

CUSHING, Brian L.; KOLESNICHENKO, Vladimir L.; O'CONNOR, Charles J. Recent Advances in the Liquid-Phase Syntheses of Inorganic Nanoparticles. **Chemical Reviews**, v. 104, n. 9, p. 3893–3946, 1 set. 2004. Disponível em: <https://pubs.acs.org/doi/10.1021/cr030027b>.

DENG, Linyu; DHAR, Bipro Ranjan. Phosphorus recovery from wastewater via calcium phosphate precipitation: A critical review of methods, progress, and insights. **Chemosphere**,

v. 330, p. 138685, jul. 2023. Disponível em: <https://linkinghub.elsevier.com/retrieve/pii/S0045653523009529>.

DENG, Yu et al. Comparative study on characteristics and mechanism of phosphate adsorption on Mg/Al modified biochar. **Journal of Environmental Chemical Engineering**, v. 9, n. 2, p. 105079, abr. 2021. Disponível em: <https://linkinghub.elsevier.com/retrieve/pii/S2213343721000579>.

EL-KHAWAGA, Ahmed M.; ZIDAN, Alaa; EL-MAGEED, Ahmed I. A. Abd. Preparation methods of different nanomaterials for various potential applications: A review. **Journal of Molecular Structure**, v. 1281, p. 135148, jun. 2023. Disponível em: <https://linkinghub.elsevier.com/retrieve/pii/S002228602300248X>.

ELZINGA, Evert J.; SPARKS, Donald L. Phosphate adsorption onto hematite: An in situ ATR-FTIR investigation of the effects of pH and loading level on the mode of phosphate surface complexation. **Journal of Colloid and Interface Science**, v. 308, n. 1, p. 53–70, abr. 2007. Disponível em: <https://linkinghub.elsevier.com/retrieve/pii/S0021979706012124>.

FOO, K.Y.; HAMEED, B.H. Insights into the modeling of adsorption isotherm systems. **Chemical Engineering Journal**, v. 156, n. 1, p. 2–10, 1 jan. 2010. Disponível em: <https://linkinghub.elsevier.com/retrieve/pii/S1385894709006147>.

GRAŽULIS, Saulius et al. Crystallography Open Database (COD): an open-access collection of crystal structures and platform for world-wide collaboration. **Nucleic Acids Research**, v. 40, n. D1, p. D420–D427, jan. 2012. Disponível em: <https://academic.oup.com/nar/article-lookup/doi/10.1093/nar/gkr900>.

GU, Wei et al. Enhanced adsorption of phosphate onto zinc ferrite by incorporating cerium. **Chemical Engineering Research and Design**, v. 117, p. 706–714, jan. 2017. Disponível em: <https://linkinghub.elsevier.com/retrieve/pii/S0263876216304580>.

______. Phosphate removal using zinc ferrite synthesized through a facile solvothermal technique. **Powder Technology**, v. 301, p. 723–729, nov. 2016. Disponível em: <https://linkinghub.elsevier.com/retrieve/pii/S0032591016304077>.

______. Removal of phosphate from water by amine-functionalized copper ferrite chelated with La(III). **Science of The Total Environment**, v. 619–620, p. 42–48, abr. 2018. Disponível em: <https://linkinghub.elsevier.com/retrieve/pii/S004896971733156X>.

GUO, Changbin et al. B-site metal modulation of phosphate adsorption properties and mechanism of LaBO3 (B = Fe, Al and Mn) perovskites. **Environmental Science and Pollution Research**, v. 30, n. 25, p. 66638–66650, 26 abr. 2023. Disponível em: <https://link.springer.com/10.1007/s11356-023-27284-8>.

GUSATTI, Marivone et al. The Rapid Preparation of ZnO Nanorods via Low-Temperatures Solochemical Method. **Journal of Nanoscience and Nanotechnology**, v. 11, n. 6, p. 5187–5192, 1 jun. 2011. Disponível em: <http://www.ingentaconnect.com/content/10.1166/jnn.2011.4183>.

HASHIM, Mohd. et al. Structural, Dielectric and Magnetic Properties of Nano-Crystalline Ni-Mg Ferrites Prepared by Citrate-Gel Auto Combustion Method. [S.l: s.n.], 2013. p. 215–224. Disponível em: <https://link.springer.com/10.1007/978-3-642-34216-5_22>.

HE, Yun et al. Mössbauer Spectroscopy, Structural and Magnetic Studies of Zn 2+ Substituted Magnesium Ferrite Nanomaterials Prepared by Sol-Gel Method. **Journal of Nanomaterials**, v. 2015, p. 1–8, 2015. Disponível em: <http://www.hindawi.com/journals/jnm/2015/854840/>.

HU, Qili; PANG, Shuyue; WANG, Dan. In-depth Insights into Mathematical Characteristics, Selection Criteria and Common Mistakes of Adsorption Kinetic Models: A Critical Review. **Separation & Purification Reviews**, v. 51, n. 3, p. 281–299, 3 jul. 2022. Disponível em: <https://www.tandfonline.com/doi/full/10.1080/15422119.2021.1922444>.

HUIXIA, Feng et al. Preparation and characterization of the cobalt ferrite nano-particles by reverse coprecipitation. **Journal of Magnetism and Magnetic Materials**, v. 356, p. 68–72, abr. 2014. Disponível em: <https://linkinghub.elsevier.com/retrieve/pii/S0304885313009268>.

HUMBE, Ashok V. et al. Cation distribution, magnetic and hyperfine interaction studies of Ni–Zn spinel ferrites: role of Jahn Teller ion (Cu 2+) substitution. **Materials Advances**, v. 1, n. 4, p. 880–890, 2020. Disponível em: <http://xlink.rsc.org/?DOI=D0MA00251H>.

HUYNH, Nguyen Chi et al. Production of MgFe2O4/activated carbons derived from a harmful grass Cynodon dactylon and their utilization for ciprofloxacin removal. **Chemosphere**, v. 343, p. 139891, dez. 2023. Disponível em: <https://linkinghub.elsevier.com/retrieve/pii/S0045653523021604>.

ILINOVA, Alina; DMITRIEVA, Diana; KRASLAWSKI, Andrzej. Influence of COVID-19 pandemic on fertilizer companies: The role of competitive advantages. **Resources Policy**, v. 71, p. 102019, jun. 2021. Disponível em: <https://linkinghub.elsevier.com/retrieve/pii/S0301420721000362>.

ISIDORO RIBEIRO, Nathália et al. Efficient phosphate adsorption by a composite composed of Mg6Al2(CO3)(OH)16·4H2O LDH and Chitosan: kinetic, thermodynamic, desorption, and characterization studies. **Separation and Purification Technology**, v. 307, p. 122717, fev. 2023. Disponível em: <https://linkinghub.elsevier.com/retrieve/pii/S1383586622022742>.

IVANETS, A. I. et al. Unusual behavior of MgFe2O4 during regeneration: desorption versus specific adsorption. **Water Science and Technology**, v. 80, n. 4, p. 654–658, 15 ago. 2019.

Disponível em: <https://iwaponline.com/wst/article/80/4/654/69708/Unusual-behavior-of-MgFe2O4-during-regeneration>.

IVANETS, A.I. et al. Magnesium ferrite nanoparticles as a magnetic sorbent for the removal of Mn2+, Co2+, Ni2+ and Cu2+ from aqueous solution. **Ceramics International**, v. 44, n. 8, p. 9097–9104, jun. 2018. Disponível em: <https://linkinghub.elsevier.com/retrieve/pii/S0272884218304140>.

IVANETS, Andrei et al. A comparative study on the synthesis of magnesium ferrite for the adsorption of metal ions: Insights into the essential role of crystallite size and surface hydroxyl groups. **Chemical Engineering Journal**, v. 411, p. 128523, maio 2021. Disponível em: <https://linkinghub.elsevier.com/retrieve/pii/S1385894721001212>.

JIANG, Shoupei et al. Phosphate recovery from aqueous solution through adsorption by magnesium modified multi-walled carbon nanotubes. **Science of The Total Environment**, v. 796, p. 148907, nov. 2021. Disponível em: <https://linkinghub.elsevier.com/retrieve/pii/S0048969721039796>.

JIANG, Yan-Hong et al. Characteristics of nitrogen and phosphorus adsorption by Mg-loaded biochar from different feedstocks. **Bioresource Technology**, v. 276, p. 183–189, mar. 2019. Disponível em: <https://linkinghub.elsevier.com/retrieve/pii/S0960852418317504>.

JUNG, Kyung-Won; LEE, Soonjae; LEE, Young Jae. Synthesis of novel magnesium ferrite (MgFe2O4)/biochar magnetic composites and its adsorption behavior for phosphate in aqueous solutions. **Bioresource Technology**, v. 245, p. 751–759, dez. 2017. Disponível em: <https://linkinghub.elsevier.com/retrieve/pii/S0960852417315845>.

JUSTIN JOSEYPHUS, R. et al. Synthesis and magnetic properties of the size-controlled Mn–Zn ferrite nanoparticles by oxidation method. **Journal of Physics and Chemistry of Solids**, v. 67, n. 7, p. 1510–1517, jul. 2006. Disponível em: <https://linkinghub.elsevier.com/retrieve/pii/S0022369706001752>.

KARIMI, M.; HASSANZADEH-TABRIZI, S. A.; SAFFAR-TELURI, A. In situ reverse co-precipitation synthesis and magnetic properties of CuO/CuFe2O4 nanocomposite. **Journal of Sol-Gel Science and Technology**, v. 83, n. 1, p. 124–131, 17 jul. 2017. Disponível em: <http://link.springer.com/10.1007/s10971-017-4386-z>.

KASHANI-NEJAD, S.; NG, K. W.; HARRIS, R. Properties of MgOHCl. **Metallurgical and Materials Transactions B**, v. 35, n. 2, p. 406–408, abr. 2004. Disponível em: <http://link.springer.com/10.1007/s11663-004-0043-3>.

KAUR UBHI, Manpreet et al. Hierarchical Nanoflowers of MgFe2O4, Bentonite and B-,P- Co-Doped Graphene Oxide as Adsorbent and Photocatalyst: Optimization of Parameters by Box–

Behnken Methodology. **International Journal of Molecular Sciences**, v. 23, n. 17, p. 9678, 26 ago. 2022. Disponível em: <https://www.mdpi.com/1422-0067/23/17/9678>.

KIM, Yoonho; ZHAO, Xuanhe. Magnetic Soft Materials and Robots. **Chemical Reviews**, v. 122, n. 5, p. 5317–5364, 9 mar. 2022. Disponível em: <https://pubs.acs.org/doi/10.1021/acs.chemrev.1c00481>.

KOFINA, A. N.; KOUTSOUKOS, P. G. Spontaneous Precipitation of Struvite from Synthetic Wastewater Solutions. **Crystal Growth & Design**, v. 5, n. 2, p. 489–496, 1 mar. 2005. Disponível em: <https://pubs.acs.org/doi/10.1021/cg049803e>.

KUANG, Xiaotong et al. Ca–Mg modified attapulgite for phosphate removal and its potential as phosphate-based fertilizer. **Journal of Environmental Management**, v. 357, p. 120727, abr. 2024. Disponível em: <https://linkinghub.elsevier.com/retrieve/pii/S0301479724007138>.

KUMAR, Prashanth Suresh et al. Adsorption as a technology to achieve ultra-low concentrations of phosphate: Research gaps and economic analysis. **Water Research X**, v. 4, p. 100029, ago. 2019. Disponível em: <https://linkinghub.elsevier.com/retrieve/pii/S2589914719300660>.

KUMAR, Shalendra et al. Mössbauer studies of Co0.5CdxFe2.5−xO4 (0.0⩽x⩽0.5) ferrite. **Physica B: Condensed Matter**, v. 403, n. 19–20, p. 3604–3607, out. 2008. Disponível em: <https://linkinghub.elsevier.com/retrieve/pii/S0921452608002573>.

KURIAN, Jessyamma; MATHEW, M. Jacob. Structural, optical and magnetic studies of CuFe2O4, MgFe2O4 and ZnFe2O4 nanoparticles prepared by hydrothermal/solvothermal method. **Journal of Magnetism and Magnetic Materials**, v. 451, p. 121–130, abr. 2018. Disponível em: <https://linkinghub.elsevier.com/retrieve/pii/S0304885317321364>.

L., Lutterotti; S., Matthies; H., Wenk. **MAUD (Material Analysis Using Diffraction): a user friendly Java program for Rietveld Texture Analysis and more**. . [S.l: s.n.]. Disponível em: <https://iris.unitn.it/handle/11572/57067#.YTwEgp1KiXQ>. , 1999

LI, Anyu et al. Preparation, adsorption performance and mechanism of MgO-loaded biochar in wastewater treatment: A review. **Environmental Research**, v. 212, p. 113341, set. 2022. Disponível em: <https://linkinghub.elsevier.com/retrieve/pii/S0013935122006685>.

LI, Shuangli et al. MgO coated magnetic Fe3O4@SiO2 nanoparticles with fast and efficient phosphorus removal performance and excellent pH stability. **Chemosphere**, v. 307, p. 135972, nov. 2022. Disponível em: <https://linkinghub.elsevier.com/retrieve/pii/S0045653522024651>.

LIANG, Hai et al. Porous MgO-modified biochar adsorbents fabricated by the activation of Mg(NO3)2 for phosphate removal: Synergistic enhancement of porosity and active sites.

Chemosphere, v. 324, p. 138320, maio 2023. Disponível em: <https://linkinghub.elsevier.com/retrieve/pii/S0045653523005878>.

LIN, Jianwei et al. Removal of phosphate from aqueous solution by a novel Mg(OH)2/ZrO2 composite: Adsorption behavior and mechanism. **Colloids and Surfaces A: Physicochemical and Engineering Aspects**, v. 561, p. 301–314, jan. 2019. Disponível em: <https://linkinghub.elsevier.com/retrieve/pii/S0927775718307672>.

LIU, Ruiting et al. Review of metal (hydr)oxide and other adsorptive materials for phosphate removal from water. **Journal of Environmental Chemical Engineering**, v. 6, n. 4, p. 5269–5286, ago. 2018. Disponível em: <https://linkinghub.elsevier.com/retrieve/pii/S2213343718304408>.

LOGANATHAN, Paripurnanda et al. Removal and Recovery of Phosphate From Water Using Sorption. **Critical Reviews in Environmental Science and Technology**, v. 44, n. 8, p. 847–907, 18 abr. 2014. Disponível em: <http://www.tandfonline.com/doi/abs/10.1080/10643389.2012.741311>.

LONG, Fei et al. Removal of phosphate from aqueous solution by magnetic Fe–Zr binary oxide. **Chemical Engineering Journal**, v. 171, n. 2, p. 448–455, jul. 2011. Disponível em: <https://linkinghub.elsevier.com/retrieve/pii/S1385894711004311>.

LU, Changyong et al. Stability of magnetic LDH composites used for phosphate recovery. **Journal of Colloid and Interface Science**, v. 580, p. 660–668, nov. 2020. Disponível em: <https://linkinghub.elsevier.com/retrieve/pii/S0021979720308985>.

LUO, Haoyu et al. Key roles of the crystal structures of MgO-biochar nanocomposites for enhancing phosphate adsorption. **Science of The Total Environment**, v. 766, p. 142618, abr. 2021. Disponível em: <https://linkinghub.elsevier.com/retrieve/pii/S0048969720361477>.

MAIA, Marina Avena et al. Phosphate removal from industrial wastewaters using layered double hydroxides. **Environmental Technology**, v. 42, n. 20, p. 3095–3105, 6 set. 2021. Disponível em: <https://www.tandfonline.com/doi/full/10.1080/09593330.2020.1722257>.

MARQUES, Willbrynner Pereira et al. Pore size increase in sol–gel prepared non-stochiometric magnesium ferrite composite during phosphorous removal from water. **Journal of Materials Science**, v. 58, n. 28, p. 11610–11630, 13 jul. 2023. Disponível em: <https://link.springer.com/10.1007/s10853-023-08734-7>.

MATHEW, Daliya S.; JUANG, Ruey-Shin. An overview of the structure and magnetism of spinel ferrite nanoparticles and their synthesis in microemulsions. **Chemical Engineering Journal**, v. 129, n. 1–3, p. 51–65, maio 2007. Disponível em: <http://linkinghub.elsevier.com/retrieve/pii/S1385894706004931>.

MAYER, Brooke K. et al. Total Value of Phosphorus Recovery. **Environmental Science & Technology**, v. 50, n. 13, p. 6606–6620, 5 jul. 2016. Disponível em: <https://pubs.acs.org/doi/10.1021/acs.est.6b01239>.

MDR. Diagnóstico Temático - Serviços de Água e Esgoto. 2021.

MEHTA, Dhruv; MAZUMDAR, Siddharth; SINGH, S.K. Magnetic adsorbents for the treatment of water/wastewater—A review. **Journal of Water Process Engineering**, v. 7, p. 244–265, set. 2015. Disponível em: <https://linkinghub.elsevier.com/retrieve/pii/S221471441530026X>.

MOHAMMED, Leena et al. Magnetic nanoparticles for environmental and biomedical applications: A review. **Particuology**, v. 30, p. 1–14, fev. 2017. Disponível em: <https://linkinghub.elsevier.com/retrieve/pii/S1674200116300852>.

MORRISH, Allan H. **The physical principles of magnetism**. [S.l: s.n.], 2001.

MUNIZ, Eduardo P. et al. On cobalt ferrite production by sol-gel from orange fruit residue by three related procedures and its application in oil removal. **Journal of Cleaner Production**, v. 265, p. 121712, ago. 2020. Disponível em: <https://linkinghub.elsevier.com/retrieve/pii/S0959652620317595>.

MUSHARAF, Muhammad et al. Solubility Enhancement of Fe in ZnO Nanoparticles Prepared by Co-Precipitation Method. **Journal of Superconductivity and Novel Magnetism**, v. 34, n. 10, p. 2633–2642, 2021.

OGINNI, Oluwatosin et al. Phosphorus adsorption behaviors of MgO modified biochars derived from waste woody biomass resources. **Journal of Environmental Chemical Engineering**, v. 8, n. 2, p. 103723, abr. 2020. Disponível em: <https://linkinghub.elsevier.com/retrieve/pii/S2213343720300713>.

OWODUNNI, Amina A. et al. A review on revolutionary technique for phosphate removal in wastewater using green coagulant. **Journal of Water Process Engineering**, v. 52, p. 103573, abr. 2023. Disponível em: <https://linkinghub.elsevier.com/retrieve/pii/S2214714423000909>.

ÖZGÜR, Ümit; ALIVOV, Yahya; MORKOÇ, Hadis. Microwave ferrites, part 1: fundamental properties. **Journal of Materials Science: Materials in Electronics**, v. 20, n. 9, p. 789–834, 25 set. 2009. Disponível em: <http://link.springer.com/10.1007/s10854-009-9923-2>.

PARASHAR, Mritunjaya; SHUKLA, Vivek Kumar; SINGH, Ranbir. Metal oxides nanoparticles via sol–gel method: a review on synthesis, characterization and applications. **Journal of Materials Science: Materials in Electronics**, v. 31, n. 5, p. 3729–3749, 13 mar. 2020. Disponível em: <http://link.springer.com/10.1007/s10854-020-02994-8>.

PATRA, Jayanta Kumar; BAEK, Kwang-Hyun. Green Nanobiotechnology: Factors Affecting

Synthesis and Characterization Techniques. **Journal of Nanomaterials**, v. 2014, p. 1–12, 2014. Disponível em: <http://www.hindawi.com/journals/jnm/2014/417305/>.

PATTAPPAN, Dhanaprabhu et al. Layered Double Hydroxides for Regulating Phosphate in Water to Achieve Long-Term Nutritional Management. **ACS Omega**, v. 8, n. 28, p. 24727–24749, 18 jul. 2023. Disponível em: <https://pubs.acs.org/doi/10.1021/acsomega.3c02576>.

PINOTTI, Camila N. et al. A new magnetic composite with potential application in boron adsorption: Development, characterization, and removal tests. **Materials Chemistry and Physics**, v. 277, p. 125368, fev. 2022. Disponível em: <https://linkinghub.elsevier.com/retrieve/pii/S0254058421011512>.

______. Fractal-like kinetics for enhanced boron adsorption on heterogeneous magnetic composite surfaces. **Materials Chemistry and Physics**, v. 308, p. 128313, out. 2023. Disponível em: <https://linkinghub.elsevier.com/retrieve/pii/S0254058423010210>.

QIU, Hui et al. Critical review in adsorption kinetic models. **Journal of Zhejiang University-SCIENCE A**, v. 10, n. 5, p. 716–724, 1 maio 2009. Disponível em: <http://link.springer.com/10.1631/jzus.A0820524>.

QUYEN, Vu Thi et al. Enhanced recovery of phosphate as a value-added product from wastewater by using lanthanum modified carbon-fiber. **Chemosphere**, v. 281, p. 130737, out. 2021. Disponível em: <https://linkinghub.elsevier.com/retrieve/pii/S004565352101208X>.

RAGHASUDHA, M. et al. Electrical resistivity and Mössbauer studies of Cr substituted Co nano ferrites. **Journal of Alloys and Compounds**, v. 694, p. 366–374, fev. 2017. Disponível em: <https://linkinghub.elsevier.com/retrieve/pii/S0925838816331358>.

RAMEZANPOUR, Samaneh; SHEIKHSHOAIE, Iran; KHATAMIAN, Massumeh. Synthesis, characterization and photocatalytic properties of V-doped Mn 3 O 4 nanoparticles as a visible light-activated photocatalyst. **Journal of Molecular Liquids**, v. 231, p. 64–71, abr. 2017. Disponível em: <https://linkinghub.elsevier.com/retrieve/pii/S0167732216335358>.

RAMOS-GUIVAR, Juan A. et al. Synergetic effect between zeolite 5 A and maghemite nanoparticles for fast lead uptake from the Peruvian river Cumbaza: Study of surface adsorption mechanism using X-ray photoelectron spectroscopy. **Applied Surface Science Advances**, v. 18, p. 100489, dez. 2023. Disponível em: <https://linkinghub.elsevier.com/retrieve/pii/S266652392300123X>.

RAZANAJATOVO, Mamitiana Roger et al. Selective adsorption of phosphate in water using lanthanum-based nanomaterials: A critical review. **Chinese Chemical Letters**, v. 32, n. 9, p. 2637–2647, set. 2021. Disponível em: <https://linkinghub.elsevier.com/retrieve/pii/S1001841721000486>.

REDDY, D. Harikishore Kumar; YUN, Yeoung-Sang. Spinel ferrite magnetic adsorbents: Alternative future materials for water purification? **Coordination Chemistry Reviews**, v. 315, p. 90–111, maio 2016. Disponível em: <https://linkinghub.elsevier.com/retrieve/pii/S0010854515300539>.

REYES-RODRÍGUEZ, P.Y. et al. Synthesis and characterization of magnetic nanoparticles Zn1-xMgxFe2O4 with partial substitution of Mg2+ (x= 0.0, 0.25, 0.5, 0.75 and 1.0) for adsorption of uremic toxins. **Ceramics International**, v. 46, n. 18, p. 27913–27921, dez. 2020. Disponível em: <https://linkinghub.elsevier.com/retrieve/pii/S0272884220323841>.

SALAH, Numan et al. Photocatalytic activity of V doped ZnO nanoparticles thin films for the removal of 2- chlorophenol from the aquatic environment under natural sunlight exposure. **Journal of Environmental Management**, v. 177, p. 53–64, jul. 2016. Disponível em: <https://linkinghub.elsevier.com/retrieve/pii/S0301479716301645>.

SALIH, Shameran Jamal; MAHMOOD, Wali M. Review on magnetic spinel ferrite (MFe2O4) nanoparticles: From synthesis to application. **Heliyon**, v. 9, n. 6, p. e16601, jun. 2023. Disponível em: <https://linkinghub.elsevier.com/retrieve/pii/S2405844023038082>.

SATYANARAYANA, Savitha et al. Magnetic characterization of nano-sized terbium doped bismuth ferrite synthesized by sol-gel method. **Journal of Magnetism and Magnetic Materials**, v. 491, p. 165571, dez. 2019. Disponível em: <https://linkinghub.elsevier.com/retrieve/pii/S030488531833899X>.

SCHOLZ, Fritz; KAHLERT, Heike. The calculation of the solubility of metal hydroxides, oxide-hydroxides, and oxides, and their visualisation in logarithmic diagrams. **ChemTexts**, v. 1, n. 1, p. 7, 24 mar. 2015. Disponível em: <https://link.springer.com/10.1007/s40828-015-0006-0>.

ŠEPELÁK, V et al. Mechanically induced cation redistribution in magnesium ferrite and its thermal stability. **Solid State Ionics**, v. 141–142, p. 677–682, maio 2001. Disponível em: <https://linkinghub.elsevier.com/retrieve/pii/S0167273801007779>.

SHARMA, Lekha; KAKKAR, Rita. Magnetically retrievable one-pot fabrication of mesoporous magnesium ferrite (MgFe2O4) for the remediation of chlorpyrifos and real pesticide wastewater. **Journal of Environmental Chemical Engineering**, v. 6, n. 6, p. 6891–6903, dez. 2018. Disponível em: <https://linkinghub.elsevier.com/retrieve/pii/S2213343718306675>.

SHIRAZINEZHAD, Maryam et al. Phosphate removal from municipal effluent by a porous MgO-expanded graphite composite as a novel adsorbent: Evaluation of seawater as a natural source of magnesium ions. **Journal of Water Process Engineering**, v. 43, p. 102232, out.

2021. Disponível em: <https://linkinghub.elsevier.com/retrieve/pii/S2214714421003196>.

SILVA, Manoj; BALTRUSAITIS, Jonas. A review of phosphate adsorption on Mg-containing materials: kinetics, equilibrium, and mechanistic insights. **Environmental Science: Water Research & Technology**, v. 6, n. 12, p. 3178–3194, 2020. Disponível em: <http://xlink.rsc.org/?DOI=D0EW00679C>.

SPERLING, Marcos von. **Wastewater characteristics, treatment and disposal**. [S.l.]: IWA publishing, 2007.

THOMMES, Matthias et al. Physisorption of gases, with special reference to the evaluation of surface area and pore size distribution (IUPAC Technical Report). **Pure and Applied Chemistry**, v. 87, n. 9–10, p. 1051–1069, 1 out. 2015. Disponível em: <https://www.degruyter.com/document/doi/10.1515/pac-2014-1117/html>.

TOLOMAN, D. et al. V-doped ZnO particles: synthesis, structural, optical and photocatalytic properties. **Journal of Materials Science: Materials in Electronics**, v. 27, n. 6, p. 5691–5698, 9 jun. 2016. Disponível em: <http://link.springer.com/10.1007/s10854-016-4480-y>.

TONG, Qiuwen et al. Hierarchical flower-like MgAl layered double hydroxide microparticles as phosphate porter for its recovery from phosphate-contaminated water. **Separation and Purification Technology**, v. 330, p. 125384, fev. 2024. Disponível em: <https://linkinghub.elsevier.com/retrieve/pii/S138358662302292X>.

TRAN, Hai Nguyen et al. Mistakes and inconsistencies regarding adsorption of contaminants from aqueous solutions: A critical review. **Water Research**, v. 120, p. 88–116, set. 2017. Disponível em: <https://linkinghub.elsevier.com/retrieve/pii/S0043135417302695>.

TU, Panfeng et al. Enhanced phosphate adsorption and desorption characteristics of MgO-modified biochars prepared via direct co-pyrolysis of MgO and raw materials. **Bioresources and Bioprocessing**, v. 10, n. 1, p. 49, 10 ago. 2023. Disponível em: <https://bioresourcesbioprocessing.springeropen.com/articles/10.1186/s40643-023-00670-3>.

UDDIN, Md. Jamal; JEONG, Yeon-Koo. Adsorptive removal of pollutants from water using magnesium ferrite nanoadsorbent: a promising future material for water purification. **Environmental Science and Pollution Research**, v. 29, n. 7, p. 9422–9447, 1 fev. 2022a. Disponível em: <https://link.springer.com/10.1007/s11356-021-17287-8>.

______. Application of magnesium ferrite nanomaterials for adsorptive removal of arsenic from water: Effects of Mg and Fe ratio. **Chemosphere**, v. 307, p. 135817, nov. 2022b. Disponível em: <https://linkinghub.elsevier.com/retrieve/pii/S0045653522023104>.

WANG, Chu-Ya et al. Efficiency and mechanism of phosphate adsorption and desorption of a novel Mg-loaded biochar material. **Environmental Science and Pollution Research**, v. 31, n.

3, p. 4425–4438, 16 dez. 2023. Disponível em: <https://link.springer.com/10.1007/s11356-023-31400-z>.

WANG, Jianlong; GUO, Xuan. Adsorption isotherm models: Classification, physical meaning, application and solving method. **Chemosphere**, v. 258, p. 127279, nov. 2020a. Disponível em: <https://linkinghub.elsevier.com/retrieve/pii/S0045653520314727>.

______. Adsorption kinetic models: Physical meanings, applications, and solving methods. **Journal of Hazardous Materials**, v. 390, p. 122156, maio 2020b. Disponível em: <https://linkinghub.elsevier.com/retrieve/pii/S0304389420301448>.

WANG, Jingxuan et al. Comparative assessment of formation pathways and adsorption behavior reveals the role of NaOH of MgO-modified diatomite on phosphate recovery. **Science of The Total Environment**, v. 876, p. 162785, jun. 2023. Disponível em: <https://linkinghub.elsevier.com/retrieve/pii/S0048969723014018>.

WANG, Li et al. MgFe2O4-biochar based lanthanum alginate beads for advanced phosphate removal. **Chemical Engineering Journal**, v. 387, p. 123305, maio 2020. Disponível em: <https://linkinghub.elsevier.com/retrieve/pii/S1385894719327172>.

WEBER, Walter J. Evolution of a Technology. **Journal of Environmental Engineering**, v. 110, n. 5, p. 899–917, out. 1984. Disponível em: <https://ascelibrary.org/doi/10.1061/%28ASCE%290733-9372%281984%29110%3A5%28899%29>.

WU, Baile et al. Selective Phosphate Removal from Water and Wastewater using Sorption: Process Fundamentals and Removal Mechanisms. **Environmental Science & Technology**, v. 54, n. 1, p. 50–66, 7 jan. 2020. Disponível em: <https://pubs.acs.org/doi/10.1021/acs.est.9b05569>.

WU, Feng-Chin; TSENG, Ru-Ling; JUANG, Ruey-Shin. Initial behavior of intraparticle diffusion model used in the description of adsorption kinetics. **Chemical Engineering Journal**, v. 153, n. 1–3, p. 1–8, nov. 2009. Disponível em: <https://linkinghub.elsevier.com/retrieve/pii/S138589470900312X>.

WU, Yingjie; GAO, Guohua; WU, Guangming. Self-assembled three-dimensional hierarchical porous V 2 O 5 /graphene hybrid aerogels for supercapacitors with high energy density and long cycle life. **Journal of Materials Chemistry A**, v. 3, n. 5, p. 1828–1832, 2015. Disponível em: <http://xlink.rsc.org/?DOI=C4TA05537C>.

XIA, Shumei et al. Preparation, characterization, and phosphate removal and recovery of magnetic MnFe 2 O 4 nano-particles as adsorbents. **Environmental Technology**, v. 37, n. 7, p. 795–804, 2 abr. 2016. Disponível em:

<http://www.tandfonline.com/doi/full/10.1080/09593330.2015.1085099>.

XU, Chenglong et al. Adsorption and immobilization of phosphorus from eutrophic seawater and sediment using attapulgite - Behavior and mechanism. **Chemosphere**, v. 313, p. 137390, fev. 2023. Disponível em: <https://linkinghub.elsevier.com/retrieve/pii/S0045653522038838>.

XU, Yanming et al. Efficient phosphate removal by Mg-La binary layered double hydroxides: synthesis optimization, adsorption performance, and inner mechanism. **Environmental Science and Pollution Research**, v. 31, n. 20, p. 29132–29147, 3 abr. 2024. Disponível em: <https://link.springer.com/10.1007/s11356-024-32838-5>.

YADAV, S.P. et al. Distribution of cations in Co1−xMnxFe2O4 using XRD, magnetization and Mössbauer spectroscopy. **Journal of Alloys and Compounds**, v. 646, p. 550–556, out. 2015. Disponível em: <https://linkinghub.elsevier.com/retrieve/pii/S0925838815300451>.

YANG, X et al. Highly visible-light active C- and V-doped TiO2 for degradation of acetaldehyde. **Journal of Catalysis**, v. 252, n. 2, p. 296–302, 10 dez. 2007. Disponível em: <https://linkinghub.elsevier.com/retrieve/pii/S0021951707003545>.

YU, Peng et al. Insights into the glyphosate removal efficiency by using magnetic powder activated carbon composite. **Separation and Purification Technology**, v. 254, jan. 2021.

ZHANG, Boaiqi et al. Adsorption for phosphate by crosslinked/non-crosslinked-chitosan-Fe(III) complex sorbents: Characteristic and mechanism. **Chemical Engineering Journal**, v. 353, p. 361–372, dez. 2018. Disponível em: <https://linkinghub.elsevier.com/retrieve/pii/S1385894718313342>.

ZHENG, Xiongliu et al. Inhibitory factors affecting the process of enhanced biological phosphorus removal (EBPR) – A mini-review. **Process Biochemistry**, v. 49, n. 12, p. 2207–2213, dez. 2014. Disponível em: <https://linkinghub.elsevier.com/retrieve/pii/S1359511314005042>.

ZHU, Danchen et al. Synthesis and characterization of magnesium oxide nanoparticle-containing biochar composites for efficient phosphorus removal from aqueous solution. **Chemosphere**, v. 247, p. 125847, maio 2020. Disponível em: <https://linkinghub.elsevier.com/retrieve/pii/S0045653520300382>.

ZHU, Qingyu; MOGGRIDGE, Geoff D.; D'AGOSTINO, Carmine. Adsorption of pyridine from aqueous solutions by polymeric adsorbents MN 200 and MN 500. Part 2: Kinetics and diffusion analysis. **Chemical Engineering Journal**, v. 306, p. 1223–1233, dez. 2016. Disponível em: <https://linkinghub.elsevier.com/retrieve/pii/S1385894716310336>.